A THREE-DIMENSIONAL PHOTOELASTIC STUDY OF WELDED TUBULAR T-CONNECTIONS

A Dissertation

Presented to

The Faculty of the Department of Civil Engineering

University of Houston

In Partial Fulfillment

of the Requirements for the Degree

Doctor of Philosophy

---

by

George Hayes Holliday

August 1970

ACKNOWLEDGMENTS

The author wishes to thank and acknowledge the many people and organizations who so graciously gave of their time and equipment so that this study could be initiated and brought to fruition.

Firstly, appreciation is due to Dr. W. M. Murray, M.I.T., who introduced me to photoelasticity. Also, credit is due to Mr. M. M. Leven, Westinghouse Electric Corporation, who so willingly offered helpful suggestions for surmounting technical obstacles.

Thanks are expressed to Dr. W. J. Graff, who served as chairman of the advisory committee and to Professor L. J. Castellanos, Dr. J. M. Nash, Dr. S. T. Poage, and Dr. A. White for acting as members of the committee.

Particular thanks are due to Shell Development Company management who encouraged me to undertake the project and who graciously permitted me the use of the company shop and laboratory facilities during evenings and weekends. In this regard, gratitude is expressed to Mr. B. N. Outwin who took his personal time to teach me the operation of the various machine tools so that I could make the plastic models which were tested.

Sincere appreciation is expressed to Miss Mary Manning who carefully read and edited the manuscript. Her suggestions considerably improved the presentation of the results.

The largest share of thanks must be reserved for my wife, Doris, who was a constant source of encouragement.

Lastly, thanks are due to Miss Sandra Rackley who carefully typed the thesis.

A THREE-DIMENSIONAL PHOTOELASTIC STUDY OF

WELDED TUBULAR T-CONNECTIONS

An Abstract

Presented to

The Faculty of the Department of Civil Engineering

University of Houston

In Partial Fulfillment

of the Requirements for the Degree

Doctor of Philosophy

---

by

George Hayes Holliday

August 1970

UNIVERSITY OF HOUSTON

ABSTRACT

A THREE-DIMENSIONAL PHOTOELASTIC STUDY OF WELDED TUBULAR T-CONNECTIONS

by

George Hayes Holliday

Offshore oil drilling and production activities have occasioned rapid advances in the design of fixed structures fabricated from tubular members. An integral part of these so-called offshore platforms is the welded tubular connection, the structural joint between intersecting tubes. Theoretical analysis of tubular connections is very difficult because of localized bending of the chord (continuous member) and brace (discontinuous member). Thus, stress distributions in tubular connections have been determined by strain gage analysis obtained from steel models.

This thesis is the first reported investigation of stress distributions of tubular connections performed by three-dimensional photoelasticity. The first portion of the thesis is devoted to (1) developing a suitable amine cured epoxy resin from which the connection components were cast, (2) machining the model components to finished dimensions, (3) assembling the models, and (4) stress-freezing the completed models. Each of these activities is discussed in detail and recommended practices set forth.

The second portion of the thesis describes the experimental results relevant to the stress distributions in T-connections, particularly near the intersection weld where, because of localized bending, stresses are high. Stress distributions in the form of stress concentration factors are compared for three T-connections having brace-to-chord thickness ratios varying from 0.354 to 0.610. The brace diameter-to-chord diameter ratio was maintained at 0.5. Loading was restricted to axial tension applied to the brace. The chord was supported at the ends by means of rigid diaphragms which were free to rotate and translate on greased spheres.

The analysis demonstrates the ability of photoelasticity to provide detailed stress distributions even in areas of high stress concentration where strain gage techniques experience difficulty. The stress distributions verify the results of previous investigators; namely, (1) stresses increase rapidly near the intersection weld, and (2) maximum stress, so-called hot-spot, occurs in the chord at the intersection weld in the transverse plane containing the brace axis. More importantly, the analysis shows that the maximum stress along the chord generator through the brace axis is not at the intersection weld, but slightly outboard of the weld because of chord wall bending. Further, the localized bending of the chord results in the brace becoming oval shaped, with the minor axis parallel to the longitudinal axis of the chord.

Stress variations across the chord and brace walls are easily observed in the slices cut from the photoelastic models. The variation is particularly severe in the chord adjacent to the intersection weld. Thus, care must be exercised in applying shell theory solutions to tubular connection problems so as to adequately consider bending effects.

KEY WORDS: Welded tubular connection, three-dimensional model, photoelastic model, T-connection, epoxy resin, stress analysis, photoelasticity, stress distribution, stress concentration, axial loading, deformation, geometric model, stress freezing, model slicing.

TABLE OF CONTENTS

Page

LIST OF TABLES

LIST OF FIGURES

Figure | Page

NOMENCLATURE

b	Brace radius to middle surface
c	Chord radius to middle surface
D_b	Outside diameter of brace
D_{bL}	Outside diameter of brace parallel to chord axis (Figure B-1)
D_{bT}	Outside diameter of brace transverse to chord axis (Figure B-1)
D_c	Outside diameter of chord
D_{cT}	Outside diameter of chord transverse to brace axis
D_{cV}	Outside diameter of chord parallel to brace axis
e	Change in gauge length of calibration bar
E_{eff}	Effective elastic modulus
F	Dimension force
f_σ	Material stress fringe value
G	Shear modulus, $E/2(1 + \nu)$
h	Thickness of calibration bar
h_b	Wall thickness of brace
h_c	Wall thickness of chord
h_1, h_2, h_3	Model slice thickness after first, second, and third machinings
ℓ	Dimension length
L	Gauge length of calibration bar
L_b	Length of brace from origin
L_{bL}	Brace length from chord at left side of model (Figure B-1)

L_{bR}	Brace length from chord at right side of model (Figure B-1)
L_b'	Average length of brace from outside of chord
L_c	Length of chord from origin
L_{cB}	Chord length from end plate to end plate at bottom of T-connection (Figure B-1)
L_{cT}	Chord length from end plate to end plate at top of T-connection (Figure B-1)
L_f	Gauge length of calibration bar
N	Isochromatic fringe order
N_i	Fringe moved during tardy compensation
P	Axial load
Q	Figure of merit, E/f_σ
R_b	Outside radius of brace
R_c	Outside radius of chord
S	Circumferential distance measured along outside surface of chord normal to chord axis
T_{cr}	Critical temperature of plastic
u_b	Axial displacement of brace
u_c	Axial displacement of chord
w	Width of calibration bar
w_b	Radial displacement of brace
w_c	Radial displacement of chord
x	Distance measured along longitudinal axis of chord
α	L_c/R_c
$\bar{\alpha}$	L_c/C
α^*	x/R_c
β	R_b/R_c
$\bar{\beta}$	b/C

ϵ	Normal strain
γ	R_c/h_c
$\bar{\gamma}$	c/h_c
φ	S/C
δ_{LB}	Angular displacement of left end of chord at bottom (Figure B-1)
δ_{LT}	Angular displacement of left end of chord at top (Figure B-1)
δ_F	Angular displacement of far side of brace
δ_N	Angular displacement of near side of brace
δ_{RB}	Angular displacement of right end of chord at bottom (Figure B-1)
δ_{RT}	Angular displacement of right end of chord at top (Figure B-1)
σ_1, σ_2	Maximum and minimum principal stress, respectively
σ_0	Orthogonal stress on surface of model, Figure 24
σ_t	Tangential stress on surface of model, Figure 24
ρ	Analyzer rotation to produce extension during tardy compensation
$\tau = \bar{\tau}$	h_b/h_c
$\ddot{\gamma}$	Angular distance around circumference of brace measured from positive x axis in counterclockwise direction

Coordinate System

x, y, z	Cartesian coordinate system (Figure 1)

Abbreviations

phr	Parts per hundred resin
DEP	Diethylaminopropylamine

Chapter 1

INTRODUCTION

The structural joint formed by welding together two or more intersecting hollow circular cylindrical tubes (pipes) is called a welded tubular connection. The primary use of this construction is in offshore structures (platforms) installed along continental shelves of the world by the petroleum industry for drilling and producing operations. Tubes are favored over more conventional structural shapes, that is, I-beams and boxbeams, because of the low and equal drag from all directions. Many tubular connections occur in such platforms, that is, joining tubular cross members to tubular legs or other tubular cross members.

Platforms are subjected to loads of varying intensity and direction. The wind, wave, and current actions cause shear, normal and bending stresses singularly or, more commonly, in combination.

Stresses adjacent to the intersection weld(s) of the connection are known to be high and to have steep gradients. Few experimental stress analyses have been made to determine the distribution of stresses. Moreover, experimental analyses have concentrated on verifying particular designs. Thus, limited elastic stress distribution data are available for discrete and simple loading conditions, e.g., tension, compression, or bending.

This dissertation is an attempt to provide a thorough experimental stress investigation of T-connections, which it is hoped will act as a starting point for a fundamental continuing study of elastic stress distributions in welded tubular connections. T-connections were selected for analysis because they provide a simple configuration on which to develop experimental techniques and at the same time generate usable data. Furthermore, it is hoped that having available an experimental stress analysis will encourage development of an analytical solution. Such analyses (experimental and analytical) should provide civil engineers fundamental knowledge of stress distribution and stress concentration factors associated with welded tubular connections.

The distribution of elastic stresses is of interest to design engineers because it provides insight into comparative static and fatigue strengths. Traditionally, scale steel models, equipped with resistance strain gages, are used to investigate elastic stress distributions in tubular connections. Such models are expensive, heavy, and difficult to load without specialized equipment. In addition, measurement of strains is limited to outside surfaces because of the difficulty of installing gages inside of model components. Further, stress distribution through the wall of the model must be inferred, since only surface stresses are detectable.

Conversely, study of tubular connections may be performed with small scale plastic models which can be loaded by dead weight of small magnitude. In addition, an investigation is not necessarily limited to surface stresses since slicing and subslicing of the model permit evaluation of stresses anywhere within the model. Furthermore, a continuous display of stresses permits rapid selection of areas of the model requiring careful analysis, thereby avoiding detailed analysis of areas of low interest. This study deals with the photoelastic determination of stresses in discretely loaded three-dimensional scale models of tubular T-connections having geometries similar to those used in current designs, Figure 1.

PURPOSE

The purpose of this photoelastic study is to determine for tubular T-connections:

1) surface principal stresses along planes of symmetry,

2) effect of change in chord (continuous member) wall thickness on the principal stresses, and

3) stress distributions in the direction of the brace (discontinuous member) axis around the intersection curve.

The study also provides experimentally determined stress distributions in the form of stress concentration factors for comparison with theory.

SCOPE

The study is based on an investigation of three-dimensional photoelastic scale T-connection models having a fixed chord-to-brace diameter ratio. Models were cast from an amine cured epoxy resin. Locked-in deformations were produced in the models by the stress freezing technique. Three models having three chord wall thicknesses were analyzed.

Loading was limited to axial tension applied to the brace. In addition, connections were simply supported at the chord ends to

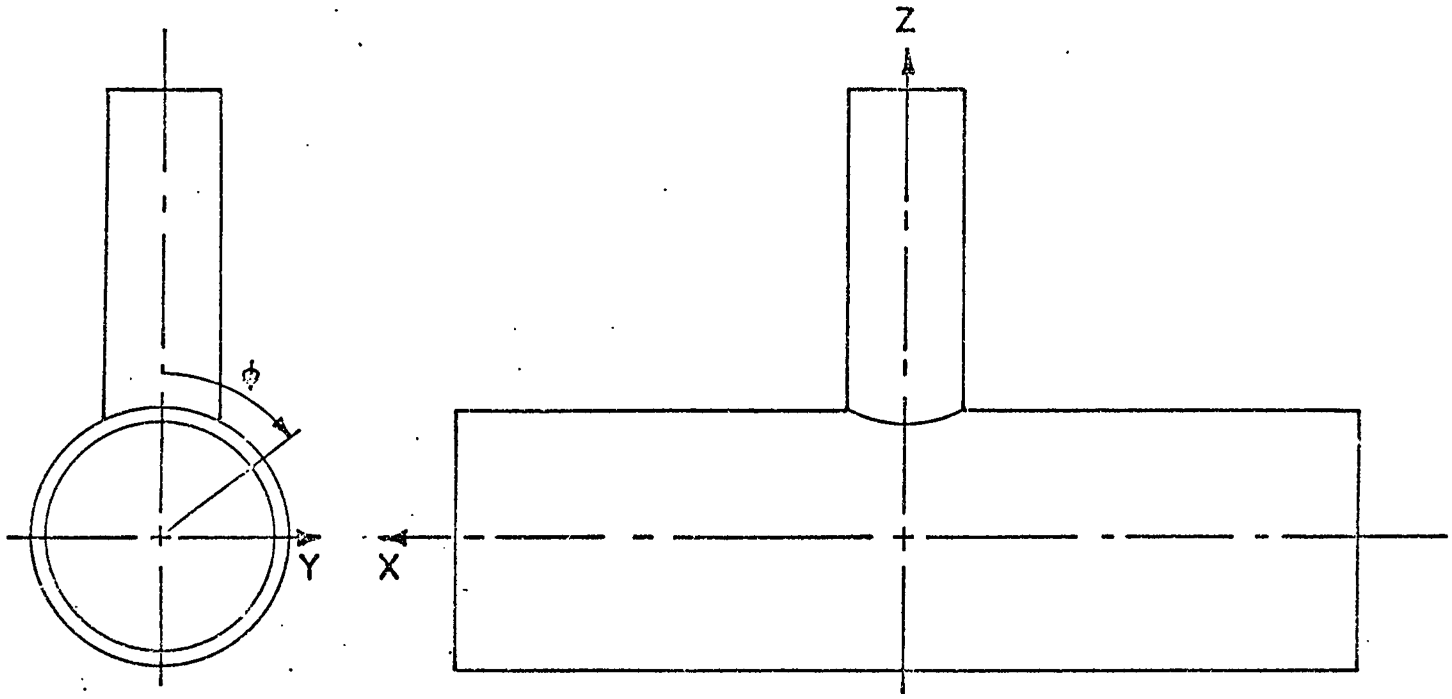

Fig. 1 - Welded Tubular T-Connection

exclude external bending moments from all models. The study was limited to surface stresses, since they are highest and of greater concern in design.

SUMMARY OF RESULTS

Three-dimensional photoelasticity is shown to be an effective and practical experimental stress analysis technique for tubular connections. The maximum stress concentrations (based on the P/A stress in the brace) at the intersection welds were found to be 5.76, 9.62, and 13.28, respectively, for T-connections having the following ratios:

Model	α^a	β^b	γ^c	τ^d
1	4.91	0.50	13.62	0.354
2	4.91	0.50	18.38	0.486
3	4.91	0.50	24.40	0.610

a) ratio of chord length to chord diameter,

b) ratio of brace diameter-to-chord diameter,

c) ratio of chord radius to chord wall thickness, and

d) ratio of brace thickness to chord thickness.

The highest stress concentration was associated with the thinnest chord, Model 3.

Photoelastic analysis showed that the peak stresses occur at or very close to the intersection weld between the brace and chord. In addition, the peak stresses result from local bending of the chord wall. The bending also produces large variations in stress across the brace and chord walls precluding accurate determination of stress by means of direct application of shell theory.

As anticipated, the chord cross section elongated under load; the major axis being parallel to the direction of tensile load. The brace also became ovalled under load. Maximum brace ovalling occurred at about 1 1/2 times the diameter above the intersection weld. Unexpectedly, the minor axis of the cross section was parallel to the longitudinal axis of the chord. Local bending of the chord wall at and near the intersection weld caused this unanticipated configuration. In addition, local bending caused the brace to increase in diameter for a small distance immediately above the intersection weld, parallel to the chord axis. This phenomenon caused the maximum stress in the apex generator (chord generator passing through the brace axis) to be attained slightly outboard of the toe of the intersection weld. The maximum chord stress in the transverse plane was at the toe of the intersection weld as reported by other investigators (Graff 1970).

The brace axial stress variation along the intersection weld was shown to be monotonically increasing from the apex generator to the transverse plane.

Chapter 2

WELDED TUBULAR CONNECTIONS

The inherent high strength-to-weight ratio of structures fabricated from tubular members makes such construction economically attractive (Hettich 1960). Tubular members also have an inherent advantage of low wind and wave loads which remain constant regardless of direction of attack. Thus, the petroleum industry has found tubular structures highly attractive for fixed platforms from which to explore and drill for oil reserves along the continental shelves of the world.

TERMINOLOGY

The term "welded tubular connection" refers to that portion of a structure where circular cylindrical tubes are joined by fusion welding of the cross section of one tube (brace) to the undisturbed exterior surface of the other tube (chord). It is important to note that the brace does not penetrate the wall of the chord. This is done to retain an unbroken and thus stronger chord as well as to prevent uncontrolled fluid communication between structural members during placement of the structure in the water.

Many tubular connection configurations are possible. Some common in-plane connections are shown in Figure 2. In addition, Figure 2 pictures the component elements of a tubular connection as

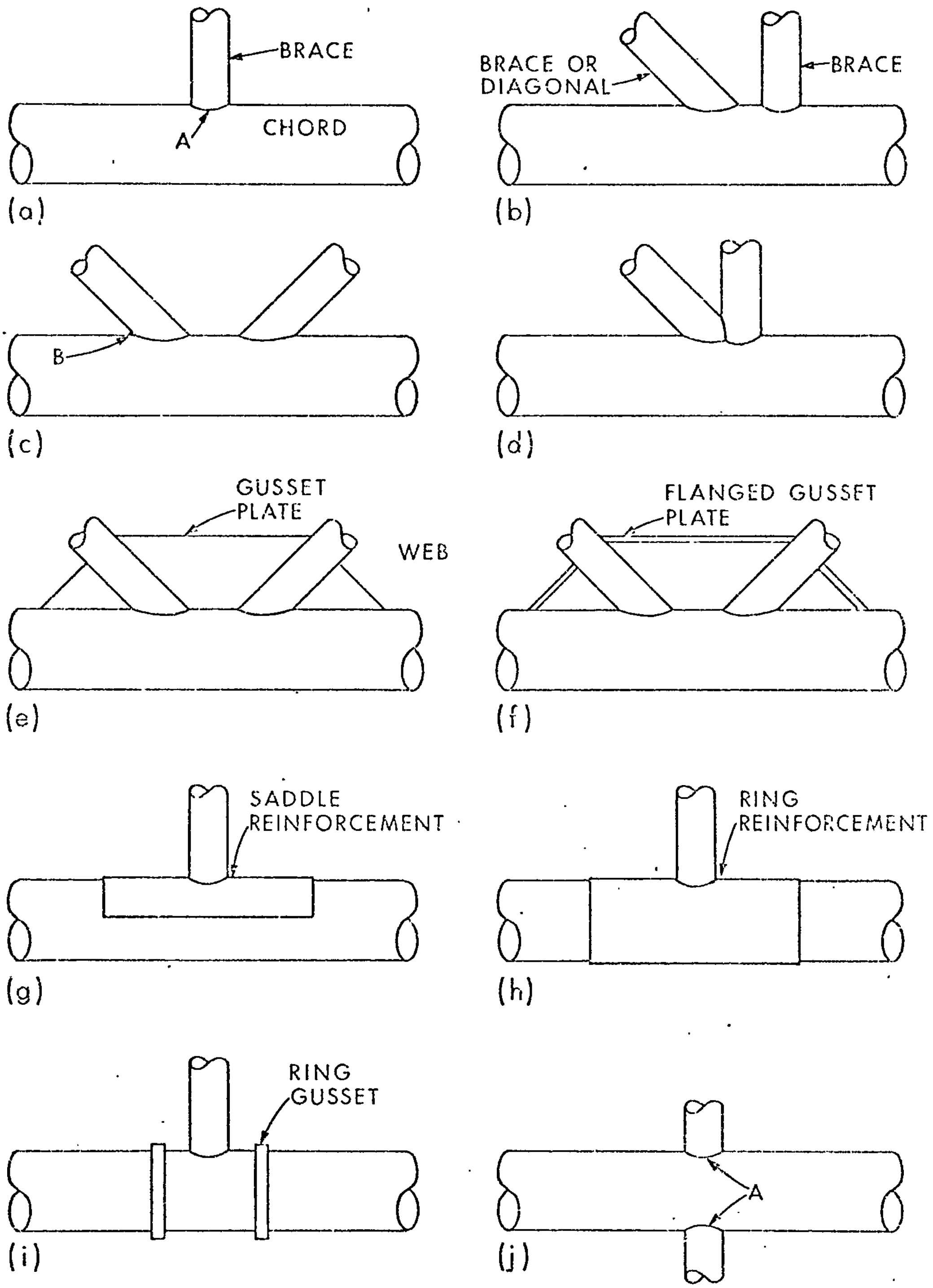

Fig. 2 - Typical in-plane tubular connection types

defined by the petroleum industry. These include:

1) chord - continuous member, normally the platform leg,

2) brace - discontinuous member, and

3) gusset - reinforcing element at or near the intersection.

Tubular connections are designated by shape; namely, T-connection (Figures 2a, g, h, and i), Y-connection, K-connection (Figures 2b-f), and Double T-connection (Figure 2j). Further, tubular connections are classified into three categories by fabrication detail. First, non-overlapping (Carter 1969), Figures 2a, b, c, and j; second, overlapping, Figure 2d; and third, reinforced (Carter 1969, Bouwkamp 1965a), Figures 2e-i. In addition, for in-plane connections where longitudinal axes of two or more braces intersect at a common point, the perpendicular distance from the point of common intersection to the chord axis is defined as the eccentricity, Figure 3. Eccentricity is normally measured in accordance with the convention established by Bouwkamp (1965a); that is, eccentricity is considered (1) negative, if measured on the side of the chord axis toward the braces, Figure 3, or (2) positive, if measured on the side of the chord away from the brace. Eccentricity is zero when chord and brace axes intersect at a common point.

Negatively eccentric connections normally result in overlapping designs, Figure 2d. The use of negative eccentricity was promoted by Bouwkamp as the result of static load tests to failure (Bouwkamp 1965a). The industry trend now is to non-reinforced non-overlapping zero eccentric connections (Carter 1969, Lee 1968). A recent study by

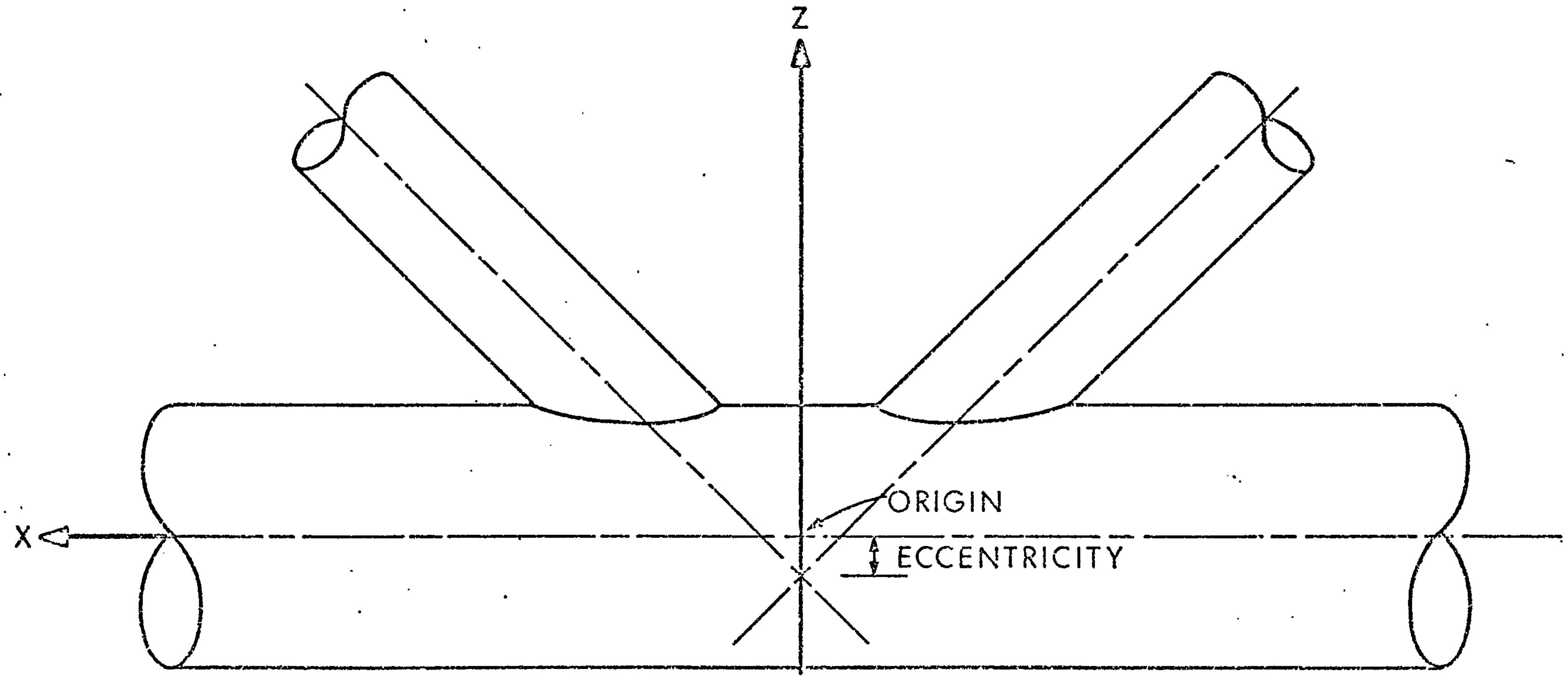

Fig. 3 - Sketch of K-connection showing positive eccentricity

by Bouwkamp (1967) indicates a marked decrease in the fatigue life of overlapping connections and reinforced connections.

A dimensional analysis of tubular connections results in development of four geometric dimensionless groups which describe tubular connections. They are:

$$\begin{aligned} \alpha &= L_c/R_c = \text{half chord length/chord radius} \\ \beta &= R_b/R_c = \text{brace radius/chord radius} \\ \gamma &= R_c/h_c = \text{chord radius/chord thickness} \\ \tau &= h_b/h_c = \text{brace thickness/chord thickness} \end{aligned} \qquad (2\text{-}1)$$

Equations (2-1) represent the groups as normally defined for design purposes. In keeping with shell theory analysis, the groups can also be defined as

$$\begin{aligned} \bar{\alpha} &= L_c/C = \text{half chord length/chord middle surface radius} \\ \bar{\beta} &= b/C = \text{brace middle surface radius/chord middle surface radius} \\ \bar{\gamma} &= C/h_c = \text{chord middle surface radius/chord thickness} \\ \bar{\tau} &= \tau = h_b/h_c = \text{brace thickness/chord thickness} \end{aligned} \qquad (2\text{-}2)$$

The design definitions, equations (2-1), will be used in this thesis because of their wide acceptance by engineers. However, the reader should be aware the dimensionless groups are defined by both equations (2-1) and (2-2) in the literature.

TUBULAR CONNECTIONS IN STRUCTURES

The first major tubular structures were built during the nineteenth century to carry railroads over bodies of water (Stewart 1959). Details of five tubular member bridges built in Britain during the nineteenth century are discussed by Timoshenko (1953) and Godfrey (1958). Tubes for these bridges were fabricated from riveted curved plates. The tubular connections were formed from riveted transition pieces which were complex and costly (Godfrey 1959).

The first major tubular member bridge built in the United States was completed in 1874 across the Mississippi River at Saint Louis, Missouri (Woodward 1881). This bridge was fabricated by riveting, but the tubular connections were special pin couplings, radically different from those used in previous bridges.

Buildings, towers, bridges, and offshore structures have been fabricated from tubular members in recent years; however, the petroleum industry has utilized tubular constructions to a larger extent than any other industry with the advent of the offshore structure (platform) in the late 1940's. Lee (1968) estimated by 1968 that 2000 fixed platforms had been installed in the Gulf of Mexico by the oil industry. The initial offshore structures were fabricated from post-tensioned concrete piles and prefabricated reinforced concrete deck sections. These structures were located in shallow water, 30 feet maximum to the mudline. With the discovery of petroleum reserves in deeper water, the steel tubular structure emerged as the standard design, but with it has emerged the difficult problem of design of adequate welded tubular connections.

REVIEW OF WELDED TUBULAR CONNECTION LITERATURE

Previous investigations of welded tubular connections can be divided into two categories: (1) theoretical analysis, and (2) experimental analysis. Since these techniques have added much to the knowledge of welded tubular connection design, it is of value to review briefly the work of previous investigators.

Theoretical Analysis

Theoretical analysis may be subdivided into three topics: (1) static failure load determination, (2) static elastic stress distribution, and (3) fatigue life prediction. The first two topics are reviewed below. Fatigue life prediction is not discussed because (1) it is beyond the scope of this thesis, and (2) few studies of engineering applicability are reported. Readers interested in fatigue, particularly low cycle fatigue, may refer to papers by Pickett (1967) and Carter (1969).

Failure load determination. The first method developed for determining load carrying capacity of welded tubular connections was the Shear Area Method (Johnston 1963), wherein it was assumed that axial load imposed by the brace was carried in direct shear by the chord wall. Toprac (1966a) indicates that the method is simple to use, but "the simplifications are so very gross that their inability to account for all the geometric parameters is obvious". To avoid this hazard, Marshall (Carter 1969) plotted experimental failure shear stress as a function of chord-radius-to-chord-thickness (γ) ratio to provide an empirical design graph.

Another method developed early in the application of tubular structures to oil exploration was the Column Analogy. Bryant (1962) compared the analogy with several experimental results with relatively good success.

The method consists of selecting and removing a representative hypothetical length of chord extending symmetrically on each side of the brace(s). The representative ring is analyzed as a curved beam. Again, because of the over-simplification of the problem, Toprac (1966a) questions the validity of the results. History appears to substantiate his opinion since the method is virtually no longer used.

Thin elastic shell theory. Thin shell theory is discussed by many authors (Timoshenko 1959, Flügge 1962). The equations developed from linear elastic small deflection theory were used by three recent investigators, Bijlaard, Dundrova, and Scordelis.

Bijlaard (1954, 1955a, 1955b, 1959) developed an approximate solution for pressure vessels by considering a radial load per unit surface (Yuan 1946). The resulting equations (Bijlaard 1955a) were solved numerically by expanding the displacements into double Fourier series. Several loading conditions were represented. The most interesting loading condition for tubular connection design is the radial load uniformly distributed over a rectangular area. This is used to approximate loading imposed by a brace on a chord. The equations for this and several other loadings were programmed (Johnston 1963). However, little use was made of Bijlaard's solution for offshore structures because of the unrealistic representation of a variable ring load parallel to the brace axis by a radial load uniformly distributed over a rectangular area.

Dundrova (1965) was the first investigator to apply shell theory equations to tubular connections. Her solution considered the chord in terms of general shell theory and the brace in terms of membrane theory. Along the intersection curve the three equations of equilibrium are satisfied but only one equation of compatibility, that is, compatibility of displacement in both chord and brace in the direction of the brace axis. Unfortunately, insufficient proof of convergence of the double Fourier series representation of stress was undertaken. Thus, there is a strong indication that insufficient terms are available in the solution to provide accurate results. Nevertheless, the solution represents a unique addition to modern shell theory.

The most recent analytical study of tubular connections was reported in 1968 by Scordelis and Bouwkamp. The investigation was based on Donnell's equation (Donnell 1933) for cylindrical shells. A general method was developed by which a cylindrical shell was analyzed for input loading or displacement. Four computer programs based on the analysis were reported. One deals with the determination of load distribution along the intersection curve. The results of the analysis compared favorably with experimental stress values reported by Noel and Toprac (1965).

Finite element analysis. The most promising analytical tool for analyzing tubular connections appears to be the Finite Element. Greste and Clough (1967) used the method to study elastic stresses in T, Y, and K-connections. The shells were represented by an assemblage of triangular elements which were connected at the corners along the middle surface. Each triangular element corner was provided with five degrees of freedom. The rotation about the axis normal to the shell middle surface was assumed to be zero. Some interesting conclusions were reached. (1) The length of the brace, if greater than two times the diameter, has no direct effect on the stresses and displacements in the chord. This was used as the basis for establishing the brace length for the photoelastic models used in this investigation. (2) The finite element fine mesh idealization of a T-connection produced stress values equivalent to (a) line displacement input and (b) force input cases reported by Scordelis (1968) using shell theory.

The finite element solution also was compared with experimental elastic stress analysis reported by Noel and Toprac (1965). The agreement was relatively satisfactory particularly away from the brace-to-chord intersection (intersection curve). Since the triangular element solution was not conserving of computer storage, Johnson (1967) developed a finite element solution utilizing a quadralateral element having five degrees of freedom.

Experimental Analysis

Experimental investigations may be divided into two broad categories: (1) failure-load determination and (2) static elastic stress distribution determination. Failure load determination has dominated the experimental investigations of tubular connections. However, recently considerable interest has been generated in the determination of elastic stress distributions. Two reasons appear responsible for the change in emphasis. First, it became increasingly evident that failure-load testing of specific designs was time consuming and unusable in establishing failure criteria for designs other than the one being tested. Second, the development of recent analytical solutions provided a means of determining stress distributions, thus reducing the number of test specimens required. For these reasons, the following review of literature dealing with failure load determination is limited.

Failure load determination. A complete survey of experimental analyses was provided by Toprac (1968, 1969) under the auspices of the Welding Research Council. The first survey presents studies completed in Japan, while the second reviews research pursued in the U.S.A. Virtually all of the Japanese and a large share of the American literature deals with failure loads.

Elastic stress distribution. The first experimental stress analysis of tubular connections was reported by Andrain (1958), Southern Methodist University. However, only one of the 11 specimens tested was provided with strain gages. Thus, heavy emphasis was placed on failure load determination.

Pease (1960) prepared the most complete of early experimental stress analyses. Strains were measured on the surface of the chord along four strain gage lines emanating from the brace of the simply supported T-connection. Localized plastic strain occurred near the intersection weld. Disregarding the plastic deformation, the experimental stresses were compared with the elastic solution developed by Bijlaard (1959). The correlation was only moderately satisfactory.

Bryant (1962) undertook an ambitious test program which included three full size specimens. One specimen, provided with six in-line braces having zero eccentricity (two-dimensional K- and

T-connections), was cement filled and equipped with 250 three-gage rosettes. The other specimens were double T-connections provided with a (1) ring gusset which was continuous through the braces, and (2) ring reinforcement which was in the form of two bands equally spaced from the center line of the braces. Unfortunately, the report treats the stress analysis rather lightly and gives limited stress data.

Bouwkamp and Toprac have added greatly to experimental study of welded tubular connections. Their contributions are too extensive to be discussed in full in this thesis; however, readers interested in static stress and alternating stress studies of T, Y, and K-connections are referred to the following publications: Bouwkamp (1965a, 1965b, 1966a, 1967, 1968) and Toprac (Noel 1965, 1966a, b, c, Beale 1967). Toprac's recent investigation (Beale 1967) is interesting because it provides graphs of surface chord stresses as a function of location on the chord.

Lastly, it is of interest to note that two studies were reported in Australia in 1961. The Stewarts and Lloyds (1961) study of Double T-connections is directly applicable to offshore platforms. This experimental study located the point of maximum stress, that is, points A, Figure 2j for Double T-connections. In addition, the longitudinal strain gage measurements on brace surfaces adjacent to the intersection weld were reported to be higher than anticipated. This same stress concentration phenomenon, due to the geometry of the connection, was reported by Toprac (1966b) for T-connections.

The second Australian study (Anderson 1961) covered an experimental investigation of tubular trusses. The so-called Type F was a K-connection in which one brace was in tension while the other was in compression. The results of this study indicated yielding first occurred in the chord at the acute angle between the compression brace and chord, point B, Figure 2c.

SUMMARY

The review of experimental stress analyses of full size and model tubular connections indicates valuable data were collected. However, all of the investigations were disconnected and aimed at solutions to individual designs. Moreover, the investigations were used to confirm specific designs rather than to provide an organized attack of the problem.

Chapter 3

PREVIOUS PHOTOELASTIC ANALYSES OF WELDED TUBULAR CONNECTIONS AND RELATED STRUCTURES

Photoelasticity is recognized as a valuable experimental tool. Readers interested in the theory of photoelasticity are referred to the two volumes by Frocht (1941, 1948). Three-dimensional photoelasticity is reported in detail by Drucker (1950).

A literature review indicates no three-dimensional photoelastic analysis of tubular connections has been reported, although two-dimensional photoelasticity has been used. However, three-dimensional photoelasticity was applied to pressure vessels, which are in many respects similar to tubular connections.

TWO-DIMENSIONAL PHOTOELASTIC ANALYSIS OF TUBULAR CONNECTIONS

Bouwkamp (1966b) reported a two-dimensional photoelastic analysis of a through-the-wall (chord and brace walls) gusset plate installed in a K-connection. The purpose of the investigation was to evaluate the influence of the gusset plate shape on the stress transfer in a tubular connection. The impetus for the study came from the need to improve the fatigue life of connections equipped with gusset plates (Bouwkamp 1967). Difficulty in making a three-dimensional investigation limited the study to gusset plates. In addition, only the shear stress distribution in the gusset was considered. Thus, the analysis precluded evaluation of any of the individual stress components. The results of the investigation dramatically demonstrated the advantage of contouring the gusset plates to provide a gradual change of section where the gusset plate terminates at the brace walls. This result was known and well documented for pressure vessels and piping (Thielsck 1965).

Two experimental studies of K-connections utilized photoelastic coating applied to the surfaces of steel models. Bouwkamp (1966a) made limited use of coatings to observe the critical stress areas in gusset plates. Hebert and Vafai (1969) analyzed the normal stresses in a self-reacting symmetric K-connection, braces of which were loaded with opposing external shears. The photoelastic results did not correlate well with strain gage data. Furthermore, the photoelastic coating was so insensitive that yielding of the brace material occurred before sufficient fringes were developed.

THREE-DIMENSIONAL PHOTOELASTIC ANALYSIS OF PRESSURE VESSELS

Analysis of stresses in pressure vessels at nozzles is closely related to analysis of stresses in tubular connections. Leven (1966) and Taylor (1966) photoelastically analyzed nearly 100 pressure vessel models of various configurations. Leven tested spherical and cylindrical vessels, while Taylor tested cylindrical vessels. The fixation or stress freezing method was employed (Drucker 1950). Both mechanical and pressure loadings were used. The purpose of the investigation was to establish (1) magnitude of stress on the inside and outside of the vessel walls, and (2) effect of nozzle reinforcement on the stress. The results are not germain to this thesis, but the conclusions relative to the accuracy of stress determination are of importance. Leven and Taylor indicated a maximum error of about ± 5 percent in the determination of circumferential stresses if they were evaluated from model transverse slices (Leven 1966, Taylor 1966), that is, a slice of the model cut through the full thickness normal to the longitudinal axis of the vessel. However, the error in determination of axial stresses was estimated to be in the range from 0 to -15 percent since axial stress evaluation depended on use of (1) circumferential stresses previously obtained, and (2) stress fringe values from sub-slices (Leven 1966, Taylor 1966), that is, thin slices taken along the inner or outer surfaces of transverse slices.

In addition, Mershon (1966) showed stresses evaluated by photoelasticity are subject to errors, but generally they are representative of actual stresses. One of the problems analyzed by Mershon was the effect of Poisson's ratio, 0.5 for plastic versus 0.3 for steel. He concluded that stresses evaluated from plastic models are higher than those determined from steel models. The effect is most pronounced when bending stresses are present, such as occurs when small nozzles penetrate the vessel shell.

Takahashi and Mark (1968a) performed a detailed photoelastic analysis of intersecting spherical and cylindrical shells exposed to external pressure. The analysis, which was compared with a finite element solution (Takahashi 1968b), indicated good correlation with the theoretical solution based on thick wall shells of revolution.

As an aside, it is interesting to note Welter and Dubuc (1962) made three separate strain measurements at the same location on steel models, using duplicate strain gages, but obtained a scatter from -7.5 percent to +6.1 percent. This tends to illustrate the inherent variability in experimental data.

Chapter 4

TUBULAR CONNECTION MODELS

Accurate photoelastic analysis depends on carefully fabricated models which faithfully represent the prototype structure. Model geometry and fabrication techniques must be carefully considered. Engineers have little difficulty in selecting proper geometry for photoelastic models because of their training in similitude. Methods of fabricating three-dimensional photoelastic models, however, are not discussed in detail in the literature. Since this omission presents considerable difficulty to the inexperienced investigator, emphasis is placed on this phase of the study in the following sections. In addition, a full description of materials and equipment is included in Appendix A.

MODEL GEOMETRY

The T-connection scale models investigated during this study have geometries similar to connections currently being fabricated into offshore structures. Constant nominal dimensions were maintained in the models except the chord wall thickness which was purposely varied to provide a range of τ-ratios, Table 1.

The chord and brace lengths were carefully selected to avoid end effects caused by loading or mounting fixtures. A chord length of about 19 inches is sufficient to provide at least 6 inches of central

Table 1

Dimensions of Photoelastic T-Connection Models

Model No.	Chord			Brace			Dimensionless Ratios				Calibration Bar	
	OD D_c inches	Thickness h_c inches	Length $2L_c$[a] inches	OD D_b inches	Thickness h_b inches	Length L_b inches	α $2h_c/D$	β D_b/D_c	γ $D_c/2h_c$	τ h_b/h_c	Thickness h inches	Width w inches
1	4.002	0.147	19.655	2.009	0.052	8.007	4.91	0.50	13.62	0.354	0.196[b]	0.251[b]
											0.201[c]	0.253[c]
2	4.006	0.109	19.682	2.006	0.053	8.196	4.91	0.50	18.38	0.486	0.182	0.251
3	4.001	0.082	19.654	2.002	0.050	8.205	4.91	0.50	24.40	0.610	0.179	0.251

[a] Length from centers of support spheres, Figure 10.

[b] Calibration bar for Model 1 brace.

[c] Calibration bar for Model 1 chord.

chord length representative of undisturbed stress distribution. This assumes that end effects disappear within 1 to 1-1/2 diameters (4 inches to 6 inches) of the chord ends. Brace length was selected on the basis of the study by Greste and Clough (1967) as discussed in Chapter 2.

The β and γ ratios were based on design practice. Current practice tends toward thicker chords, that is, τ-ratio of 1/3; however, many platforms are being designed with $\tau = 1/2$. Moreover, many older platforms have $\tau = 1$. The models shown in Table 1 were fabircated with these ratios in mind. Because of practical limitations of machining and loading, the minimum chord thickness was held at 0.082; that is, $\tau = 0.610$ instead of $\tau = 1$.

Each model was measured before and after stress freezing to establish

1) original model geometry,
2) model distortion resulting from stress freezing, and
3) configuration after stress freezing.

Refer to Appendix B for dimensions of the T-connection models.

MODEL FABRICATION TECHNIQUE

Three steps are required in the fabrication of a photoelastic model (1) casting, (2) machining, and (3) assembling. Each of these is discussed below.

Casting

The model components used in this study were cast from EPON 815® activated with 5 phr DEP (diethylaminopropylamine). Development and characteristics of the plastic are discussed in detail in Appendix C. Since components cast from epoxy have a stressed surface or "rind" which cannot be removed by stress relieving, components cannot be cast to finished size. This requires the mold to be oversize so that the rind can be removed by machining. Generally, the components should be about 1/4 inch oversize to provide sufficient stock, and all component castings for one model should be poured at the same time to assure uniformity.

Three T-connection models were fabricated for this study. Each model was cast in two parts (1) chord and (2) brace. In addition, a sheet casting was made from which calibration bars were cut. The chord, brace, and sheet were cast from the same pour of catalyzed epoxy, but, during the machining of the first model, the original chord was broken. A second chord and sheet casting were made necessitating two sets of calibration bars for determining the photoelastic properties of Model 1.

The chord finished nominal outside diameter is 4 inches, Table 1; thus the casting was made in a 4-1/4 inch tubular mold.

A 3-inch center core was provided to decrease the mass of resin required and provide additional surface for heat dissipation, Figure 4. The brace was cast as a solid cylinder 2-3/8 inches outside diameter since the finished nominal dimension is 2 inches, Table 1 and Figure 4. Sheet castings were made between two pieces of Lucite separated by 3/8-inch spacers.

After the activated EPON 815® was poured, the molds were permitted to gel at room temperature, 75°F for 48 hours. The gelled

Fig. 4 - Chord, brace, and sheet molds

resin was cured fully by heating at 180°F for 1 hour. The resulting castings are shown in Figure 5.

The casting procedure is described in detail in Appendix D.

Machining

The chords and braces were turned to finished dimensions in a geared-head lathe. The intersection curve, semi-circular saddle at the end of each brace, was fly-cut in a vertical spindle milling machine. Calibration bars were milled to profile on a numerically controlled automatic vertical spindle mill after being fly-cut to thickness on a vertical spindle mill. Medium to high rotating speeds and low feed rates were used and only carbide-tipped tools were employed because of the abrasive characteristics of cured plastic.

Each model required approximately 40 hours to machine to finished dimensions, Table 1. The finished components are shown in Figure 6.

Details of the machining operations are presented in Appendix E.

Assembling

The intersection weld of tubular connections represents an area of particular interest since the stress gradient there is high. Normally, epoxy cement is thickened with Cab-o-sil* which makes the glue line opaque. For butt welds, opaque cement is satisfactory. However, for fillet welds, such as are inherent with tubular connections, Figure 7, observation of stress flow through the weld is obliterated by the Cab-o-sil.

*Cab-o-sil, Godfrey L. Cabot, Inc., 77 Franklin St., Boston, Massachusetts.

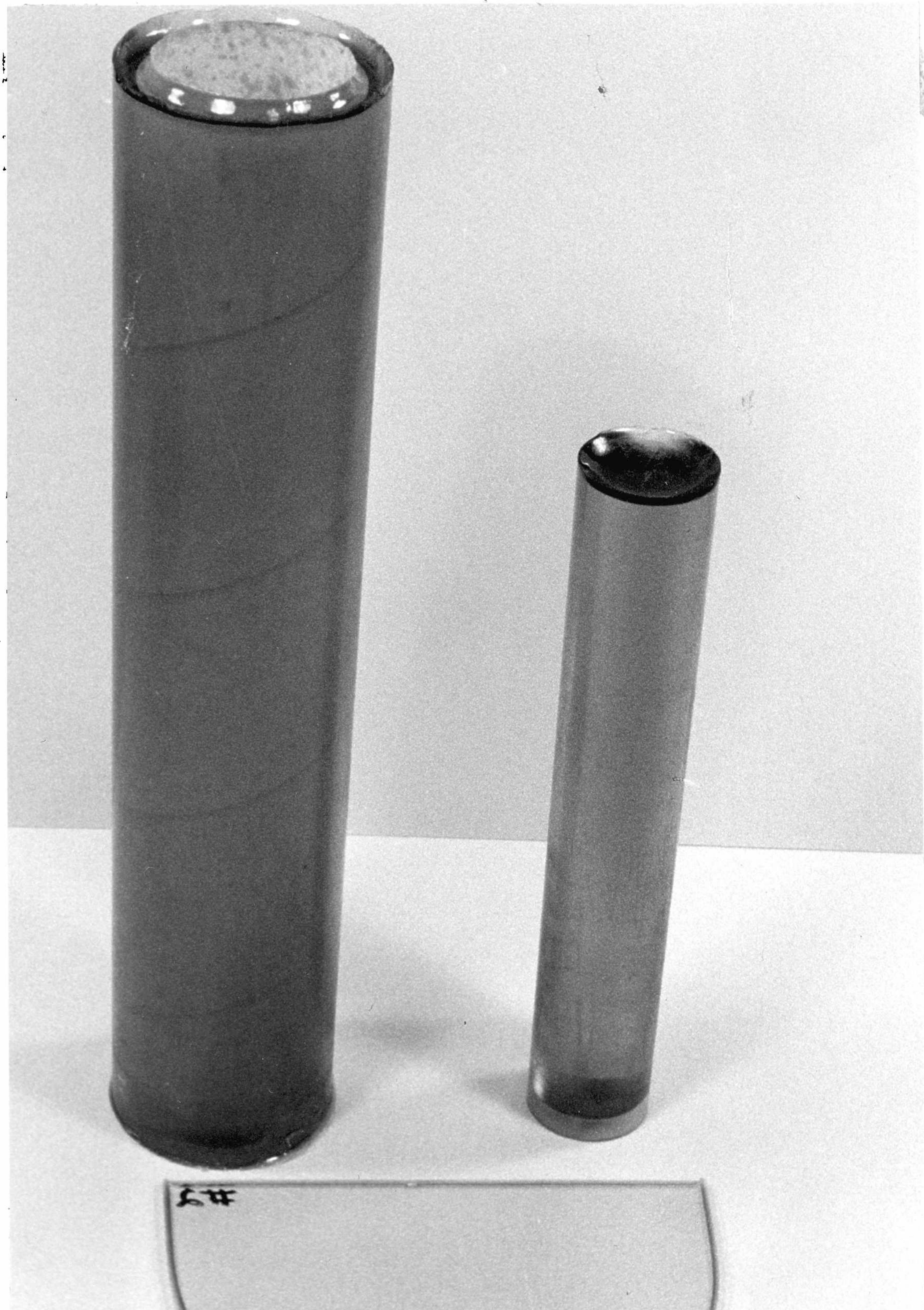

Fig. 5 - Chord, brace, and sheet castings

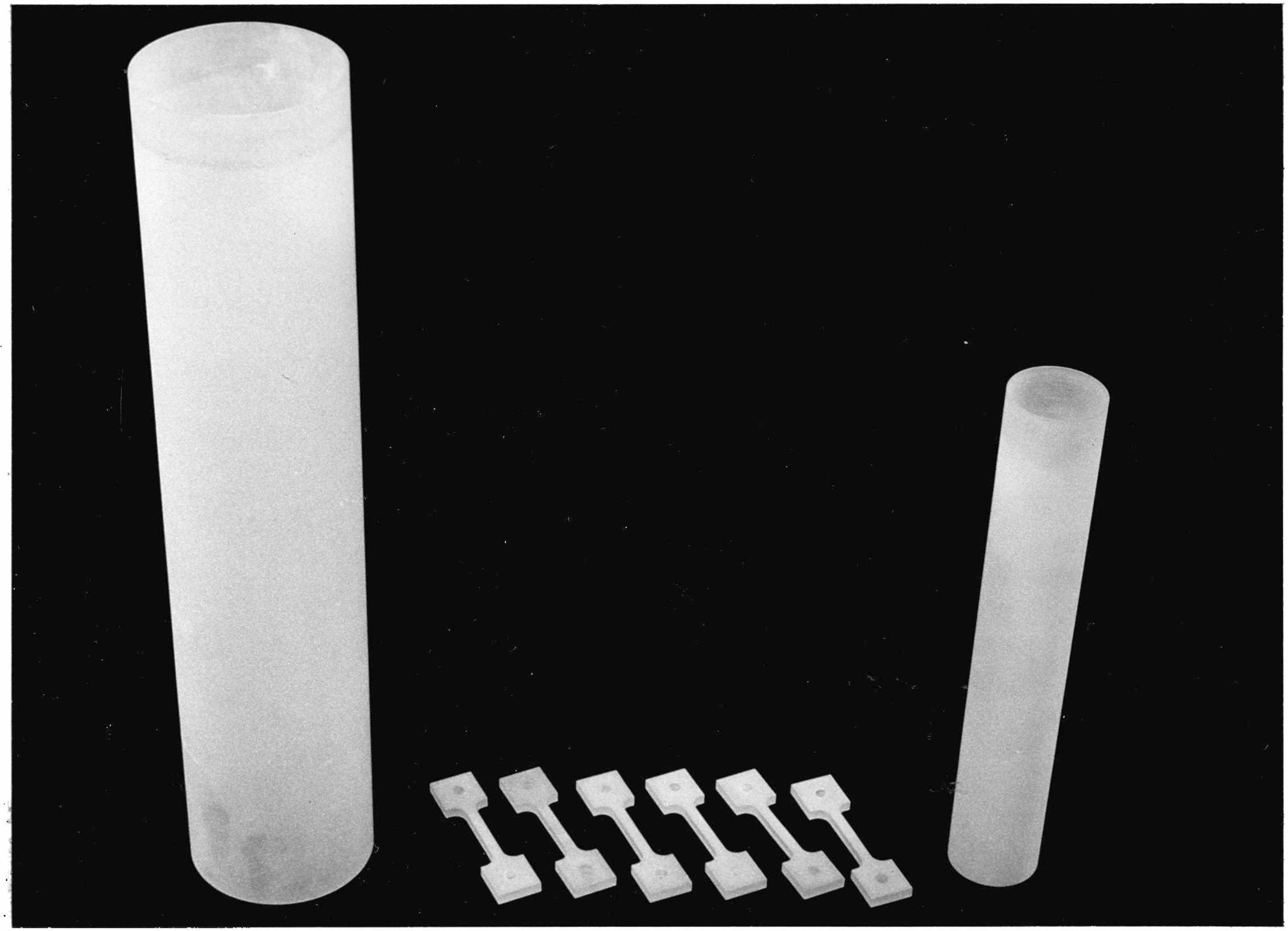

Fig. 6 - Machined chord, brace, and calibration bars

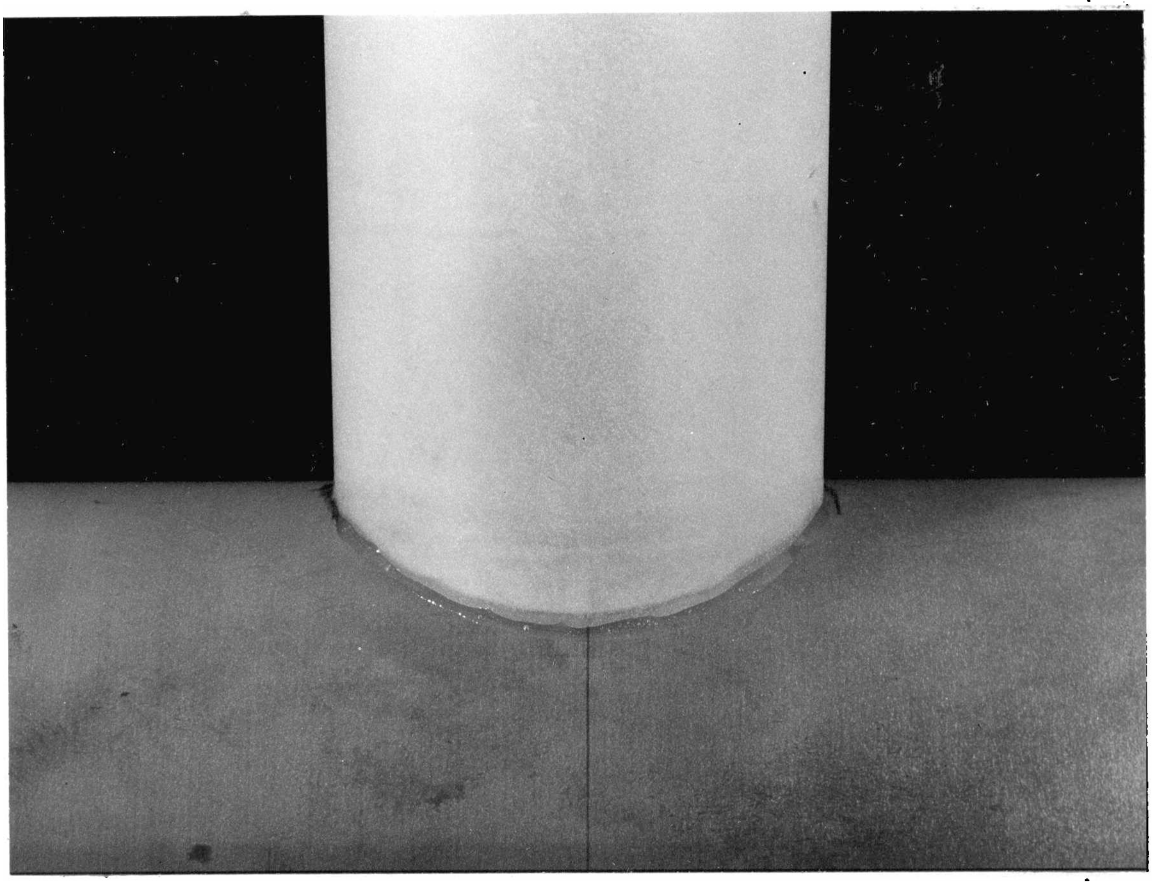

Fig. 7 - T-connection model intersection weld

A technique employing translucent cement was developed. It consists of using the same epoxy base for the intersection weld cement as for the model except that the activated resin was permitted to thicken under vacuum before being applied to the model. As thickening time is a function of the mass of resin, it is important to use the proper weight of resin and curing agent to achieve desired thickening in the given time. Experimentation indicated that curing of 25 grams of EPON 828® (unthinned EPON 815®) with 10 phr DEP produces a sufficiently thick resin in 5-1/2 hours.

The models were assembled and held in a simple jig for 48 hours while the intersection weld cement cured. Weight equivalent to about 2 psi of intersection weld area was applied to the brace during curing so as to provide a thin glue line. The assembled connection is shown in Figure 8. Details of model assembly are discussed in Appendix F.

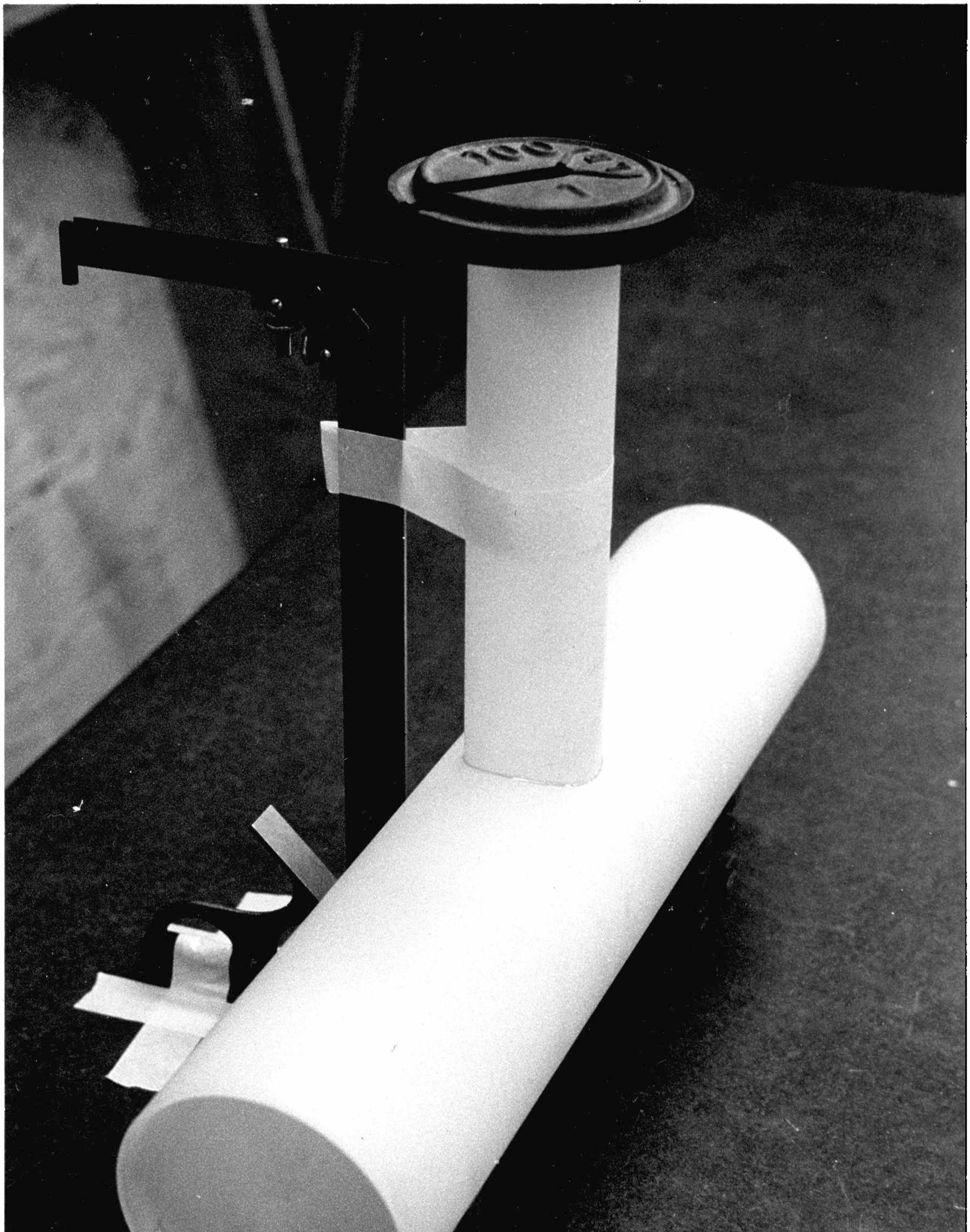

Fig. 8 - T-connection model intersection weld curing under load while held in position by tri-square jig

Chapter 5

LOCKED-IN DEFORMATIONS

The ability to retain deformations in photoelastic models makes three-dimensional photoelasticity a powerful analytic technique. Three methods are available for locking deformations into the models (Dalley 1965):

1) stress freezing,

2) creep, and

3) curing.

In these methods, deformations are fixed into the model on a molecular scale, thereby permitting the model to be cut into slices without relieving locked-in deformations. Stress freezing is the most popular technique for producing locked-in deformations because of ease of application and consistency of results.

The basis for stress freezing is the diphase behavior of resins when heated (Hetényi 1938). In gross simplification, the resins can be likened to ice in which an assemblage of springs is imbedded. Melting of the ice permits the springs to assume the load previously carried by the ice. Refreezing locks in the spring deformations. In an analogous fashion, heating of plastic under load permits secondary molecular bonds to assume the imposed load. The temperature at which primary bonds of the plastic relax is the critical temperature, T_{cr}, 92-95°C for the amine cured plastic used for tubular connection models.

STRESS FREEZING PROCEDURE

Stress freezing requires slow cooling to avoid locking in thermal deformations. Care must be exercised to avoid extraneous loads and excessive deformations which can affect the results. These problems were avoided by (1) heating and cooling models in a controlled temperature oven, Figure 9, and (2) noting model dimensions before and after stress freezing, Appendix B.

Supporting and Loading Models

External bending moments were eliminated from chord ends by providing a special support fixture, Figure 10. Chord ends were fitted with a stiff diaphragm which was cemented in place. Connected to each diaphragm was a pair of mating plates with a spherical cavity between them. These plates were assembled so as to "capture" spherical balls mounted on a shaft. The ball at one end of the connection was affixed to the shaft. The ball at the other end of the shaft was free to move.

The model was mounted horizontally with the brace facing downward, Figure 11. A calibration bar and load were attached to the brace by means of an end plate which was provided with a hemispherical cavity, spherical ball, and loading fixture, Figure 10. The calibration bar was provided for determining the sensitivity of the model plastic under temperature and load conditions imposed on the model. A weight was hung from the bar adapter after the model reached stress freezing temperature, that is, 90°C, Figure 11.

All models were loaded in a similar fashion. Loads used for each model are shown in Table 2.

Fig. 9 - Stress freezing oven

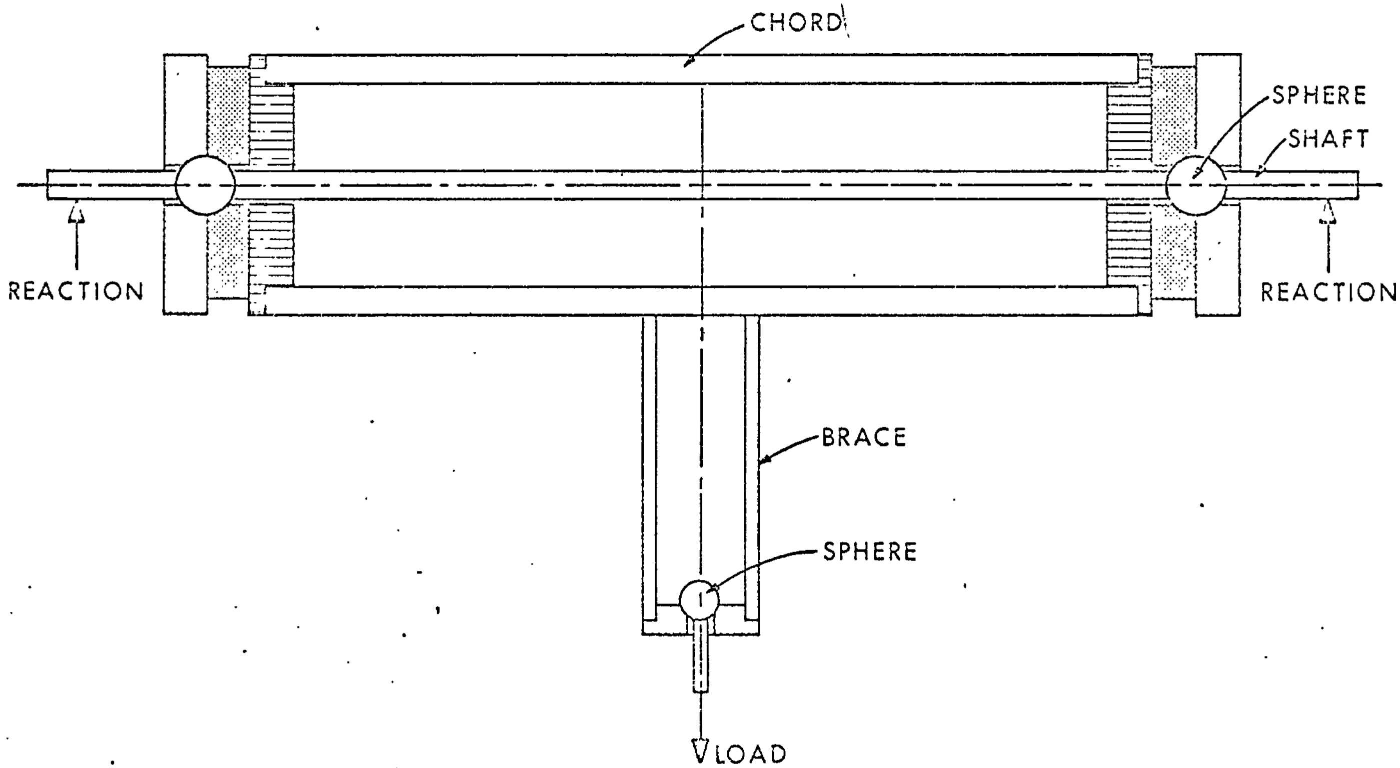

Fig. 10 - T-connection model loading fixture

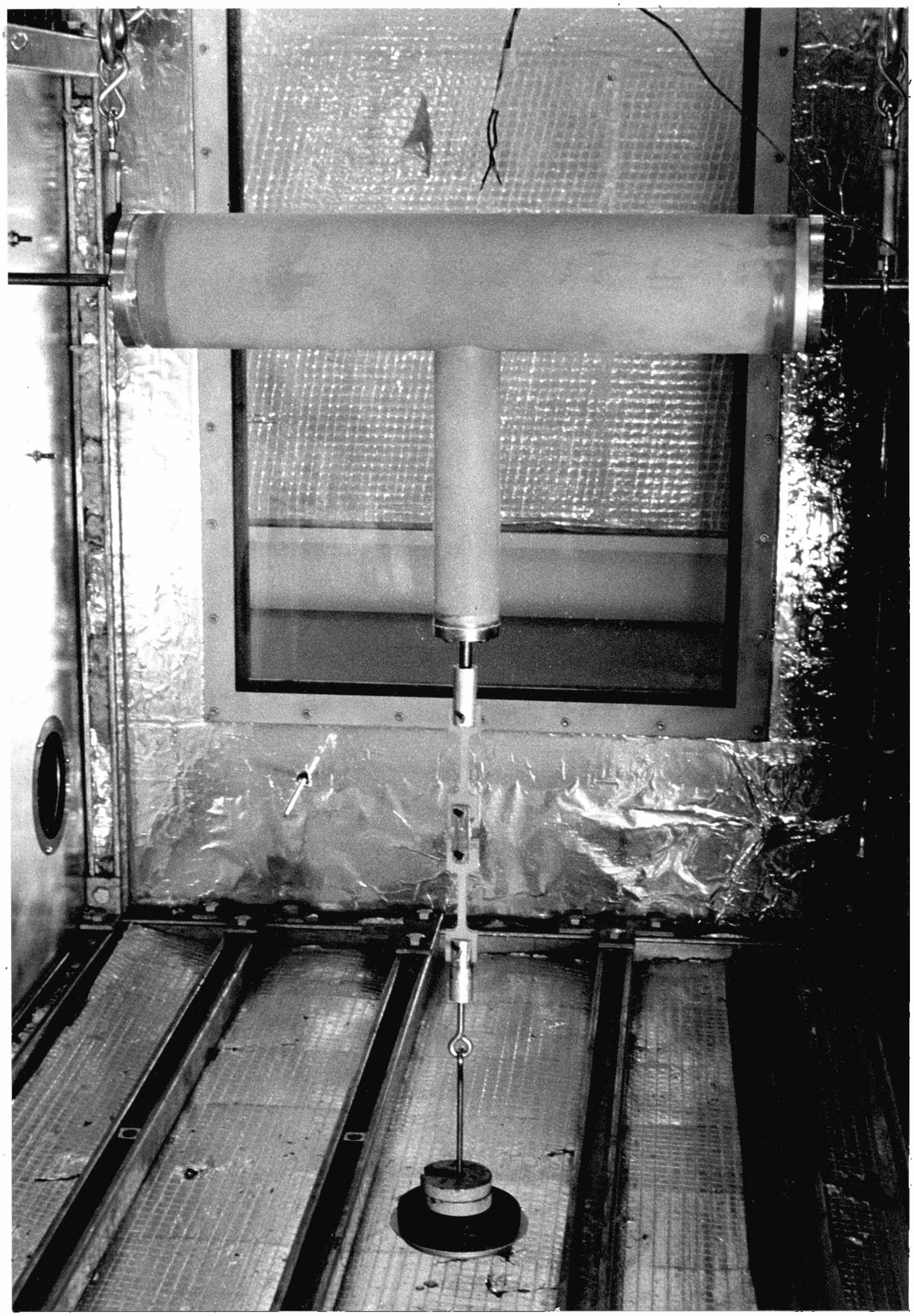

Fig. 11 - T-connection model mounted in oven. Gravity load applied to brace through calibration bars

Table 2

T-Connection Model Test Conditions During Stress Freezing

Model No.	Heating: Time Duration hr - min	Heating: Final Temperature °C	Loading: Time Duration hr - min	Loading: Temperature °C	Loading: Weight On Calib. Bar g	Loading: Weight On Model g	Cooling: Time Duration hr - min	Cooling: Final Temperature °C
1	2-0	90	4-0	90	978.36[a] 941.92[b]	1217.14	22-0	37
2	3-0	90	4-15	90	942.20	1180.0	36-0	35
3	2-0	90	4-0	90	942.1	1180.02	34-0	35

[a] Chord calibration bar.

[b] Brace calibration bar.

Temperature and Time of Loading

Each model was individually stress frozen. The temperature of the model was raised from about 37°C to 90°C over a period of approximately 2 hours, Table 2. The model brace was loaded as soon as the stress freezing temperature of 90°C was attained, Appendix C. Oven temperature was maintained at 90°C for about 4 hours during loading, Table 2, by a set point temperature controller, Figure 12. Model temperature was sensed by a thermocouple located above the model, Figure 11. Model temperature was independently monitored by a remote indicating thermocouple.

While the cooling cycle for Model 1 was manually controlled and resulted in an erratic cooling trend, Figure 13, an average cooling rate of 2 - 2.4°C/hr was maintained. This was considered sufficiently slow to avoid residual thermal stresses in thin sections based on experience of Galle (1959).

Cooling cycles for Models 2 and 3 were controlled mechanically by a clock-driven temperature adjuster mounted on the controller, Figure 14. A representative stress freezing cycle provided by mechanical cooling cycle control is shown in Figure 15. The resulting average cooling rate was about 1.3°C/hr.

MODEL SLICING

Three-dimensional photoelastic models are cut into two-dimensional slices for analysis. The general procedure is:

1) locate the slices,
2) scribe slice center lines and edge lines,

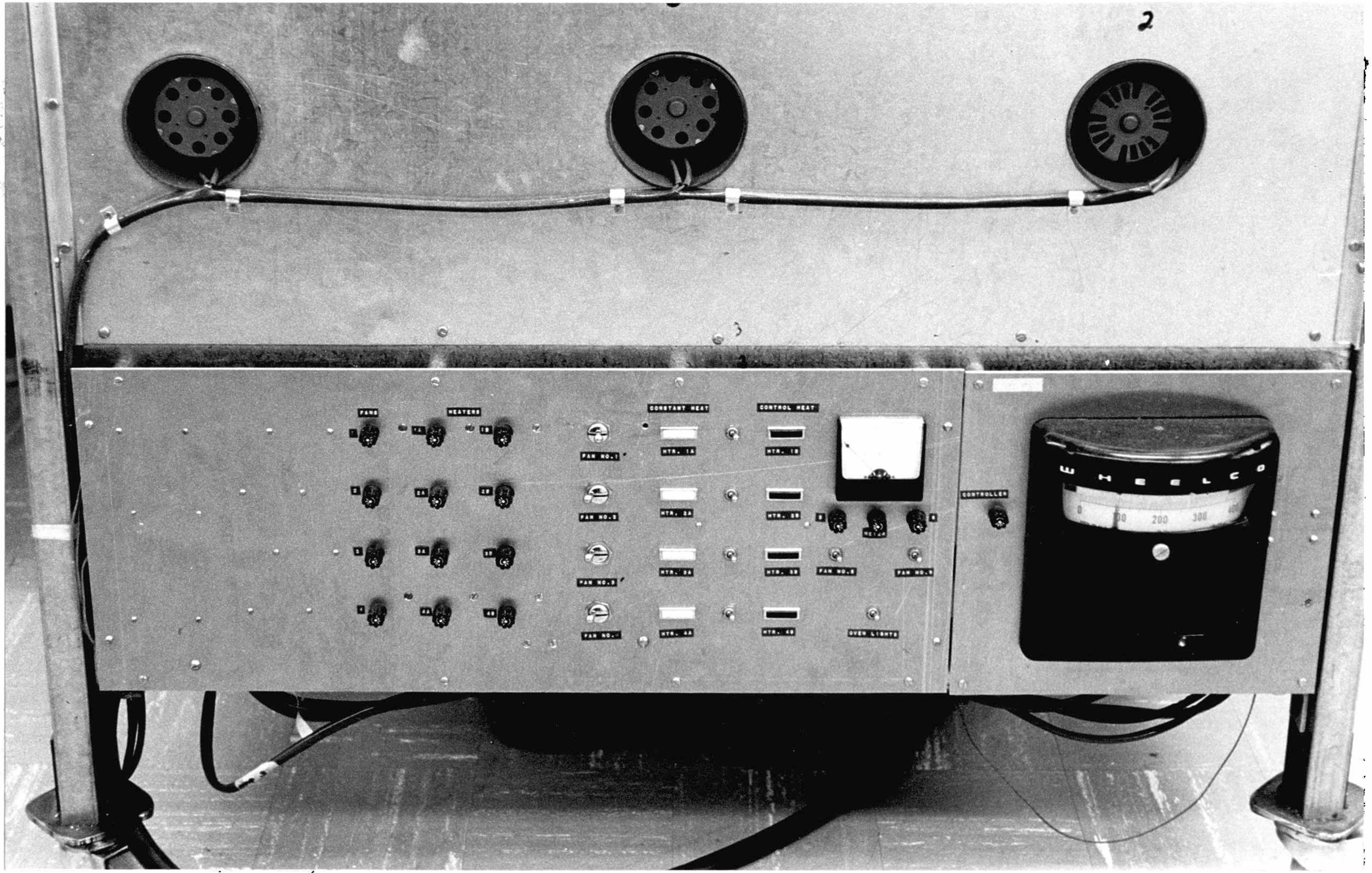

Fig. 12 - Stress freezing oven control panel. Temperature controller is located at right end of panel

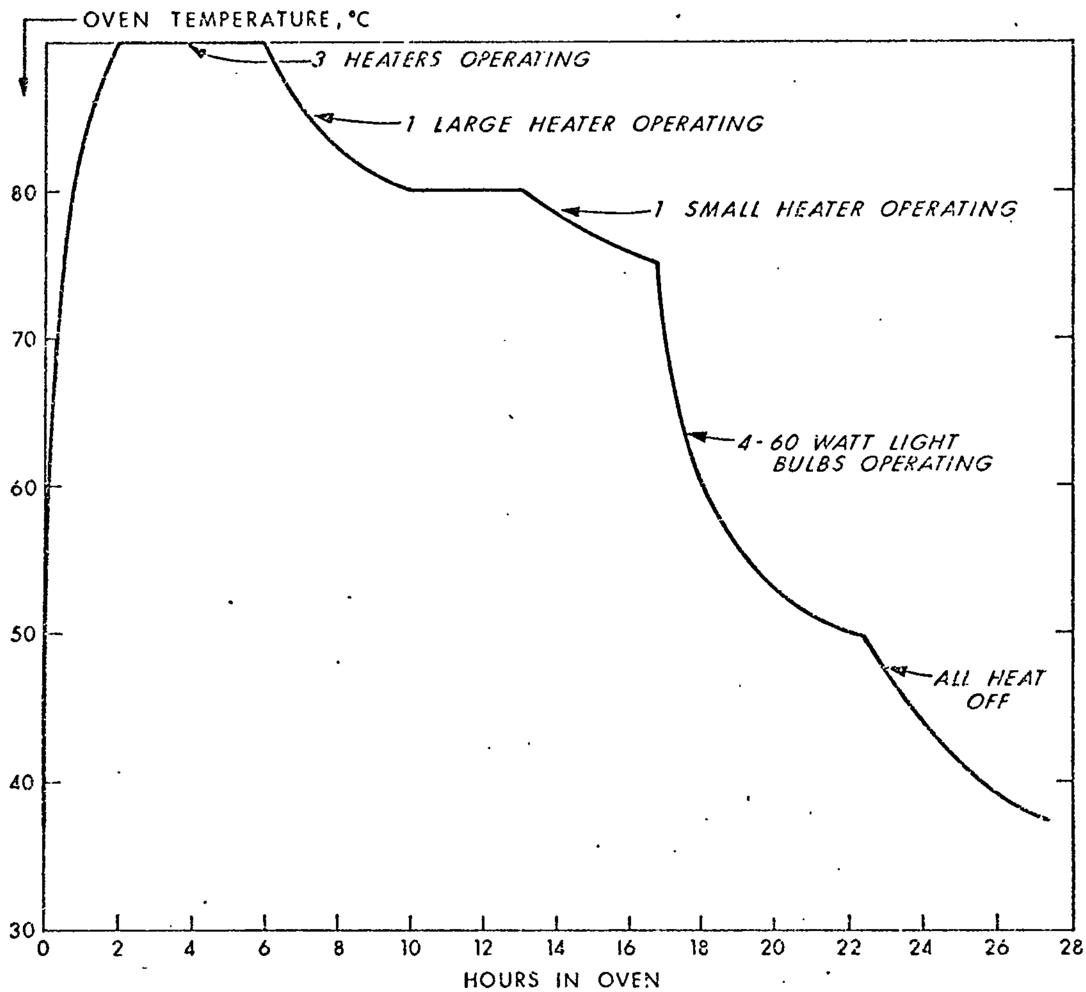

Fig. 13 - Stress freezing cycle for T-connection Model 1

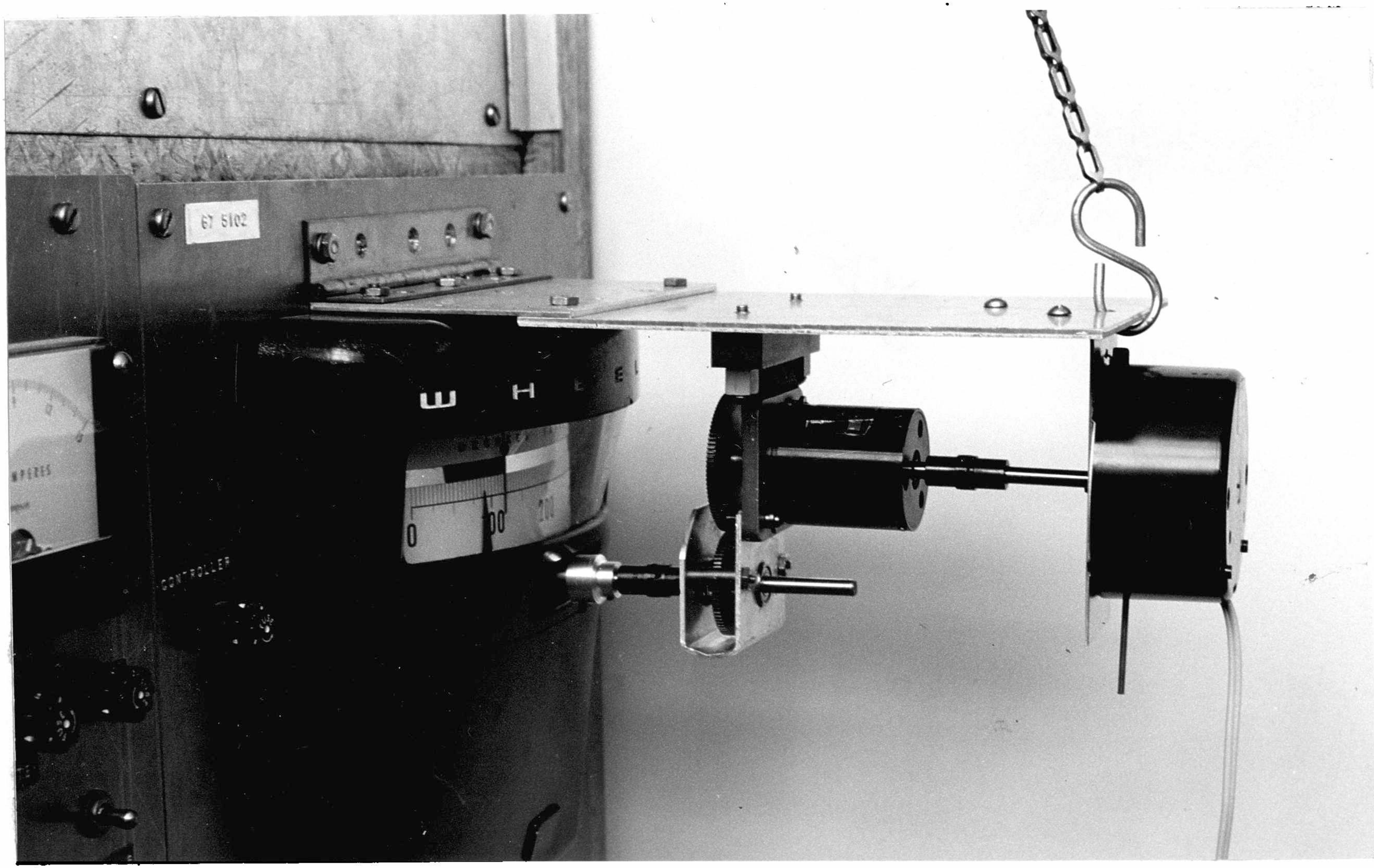

Fig. 14 - Stress freezing oven cooling cycle adjuster fitted to temperature controller

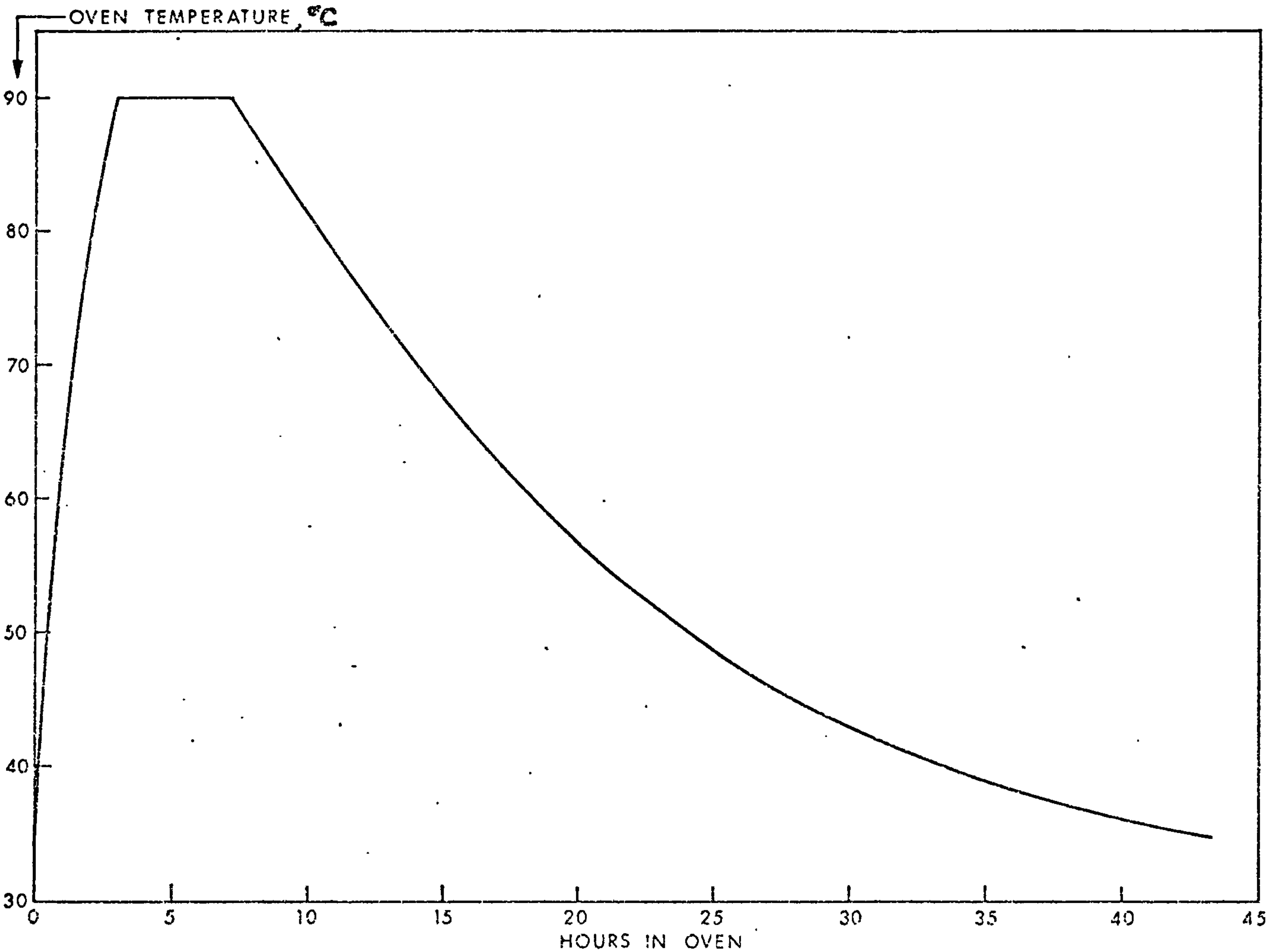

Fig. 15 - Typical stress freezing cycle for T-connection Models 2 and 3

3) rough cut the slices, and

4) finish slide edges.

Care must be taken during slicing and finishing operations to avoid relieving the locked-in deformations by heat from the tools.

Locating and Scribing Slices

Slices were laid out along the two principal planes of symmetry containing the model connection origin:

1) parallel to chord axis and

2) normal to chord axis.

Slices were scribed every 30° around the brace circumference. Figure 16 shows the center and edge lines scribed in the marking ink painted on the T-connection. The edge lines are 1/4 inch apart. Refer to Appendix G for details of locating and scribing procedure.

Cutting and Finishing Slices

Slices were rough cut from the model using a high speed grinder equipped with a dentist's burr, Figure 17. Cuts were made about 1/16 inch outside of outer scribe lines, Figure 18. Finishing was performed by fly-cutting slices which were held by molding clay, Figure 19. Finished slices are shown in Figure 20. Details of slice cutting and finishing operations are included in Appendix G. Because the loading is symmetrical, only one quadrant of the T-connection need be analyzed. Thus, four slices were cut, ψ = 90-270°, 120°, 150°, and 180°, Figure 21. Finished thicknesses of each slice are summarized in Table 3. The 90-270° and 180° slices lie along principal planes of symmetry. Brace sections of the 120° and 150° slices are also along principal planes of symmetry. Chord sections of the 120° and 150°

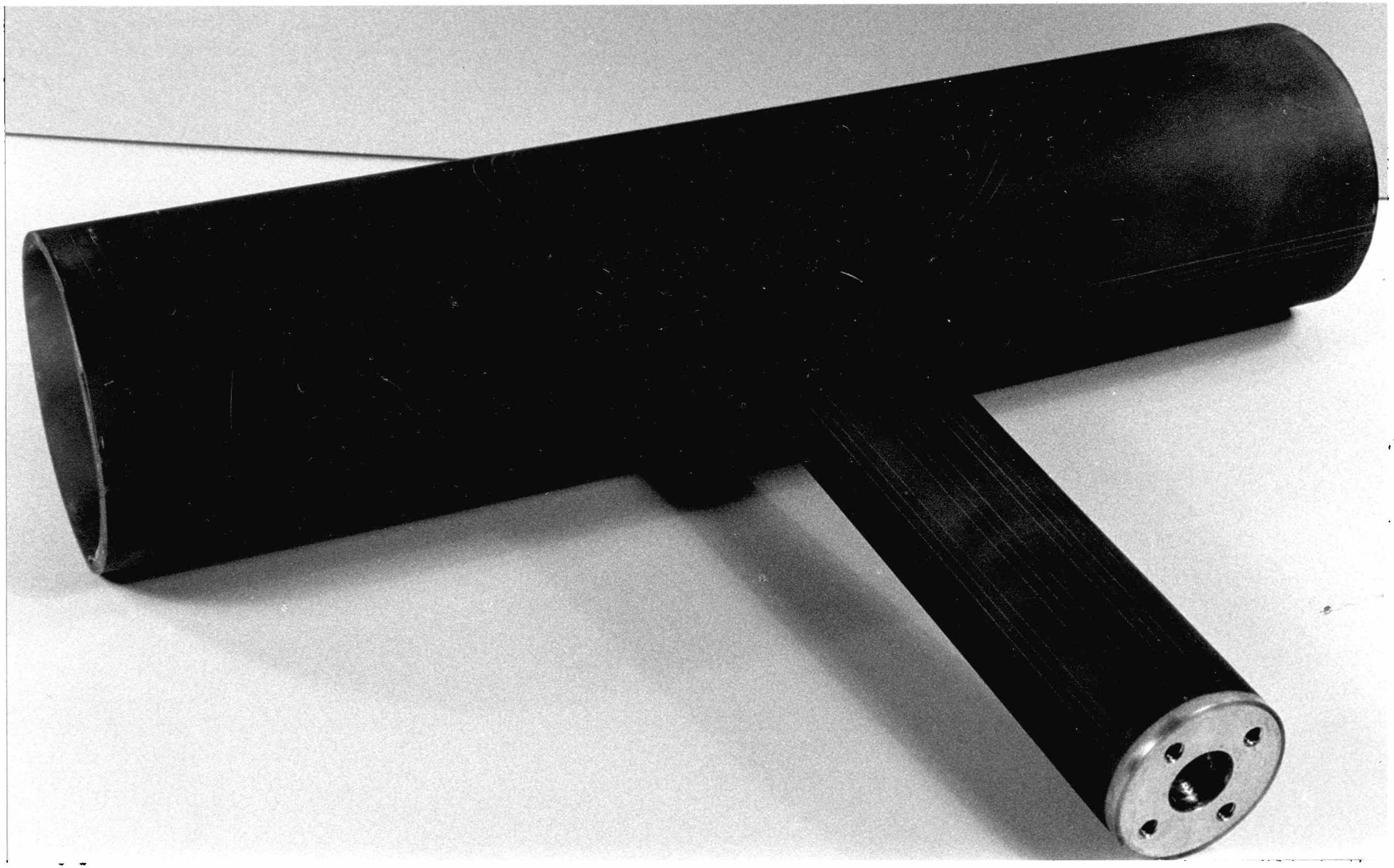

Fig. 16 - T-connection model scribed every 30° around brace after stress freezing

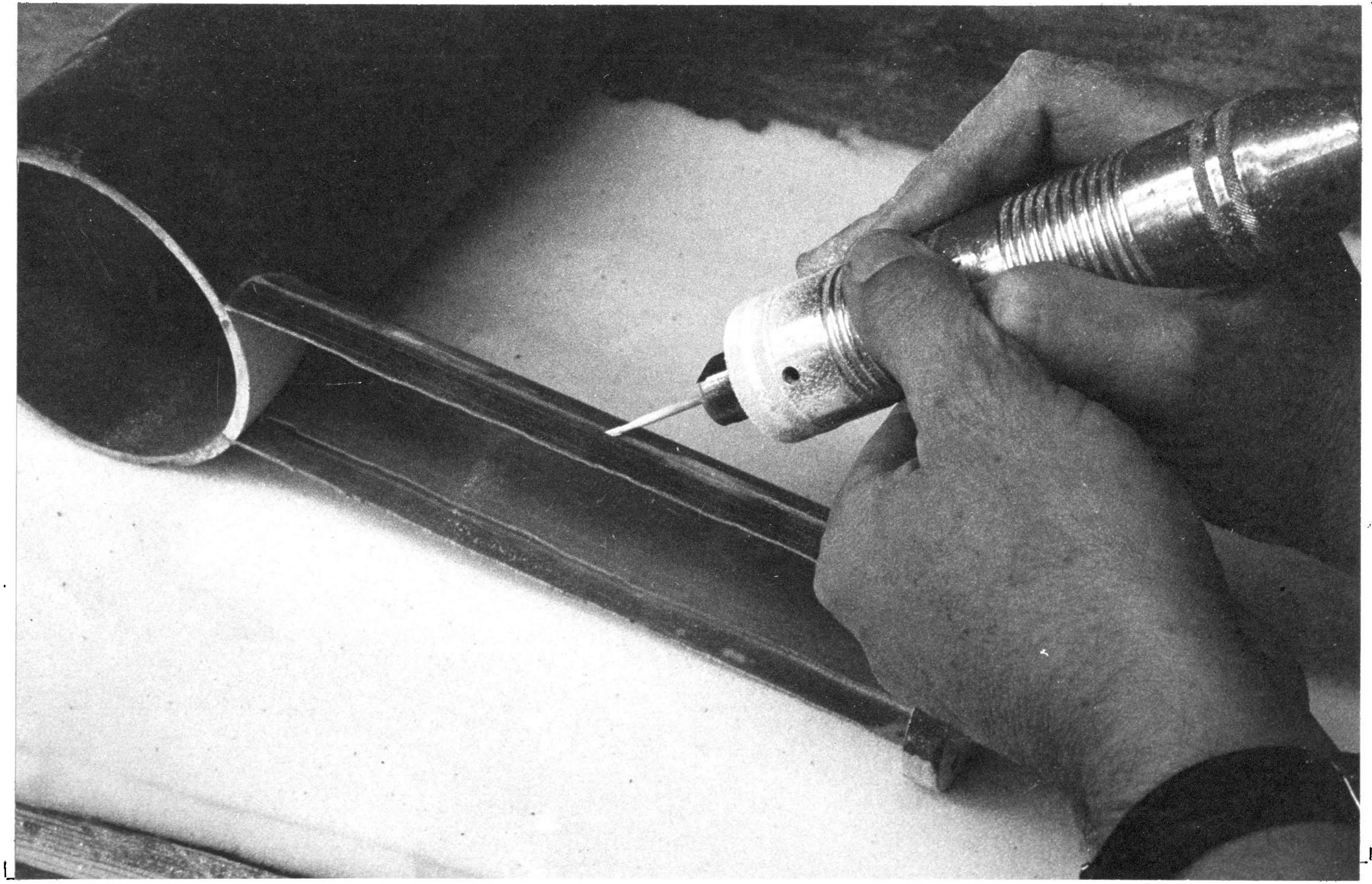

Fig. 17 - Cutting slice from T-connection model chord with high speed grinder and dentist's burr

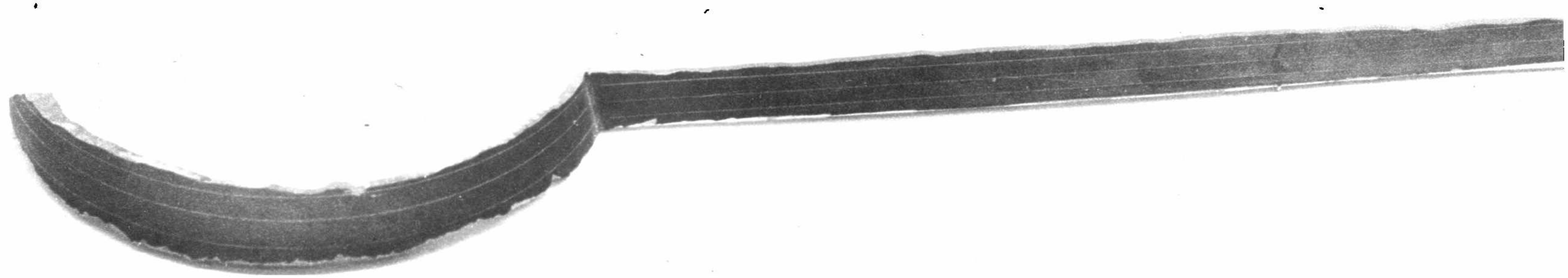

Fig. 18 - Rough cut slice showing scribe lines on brace and chord

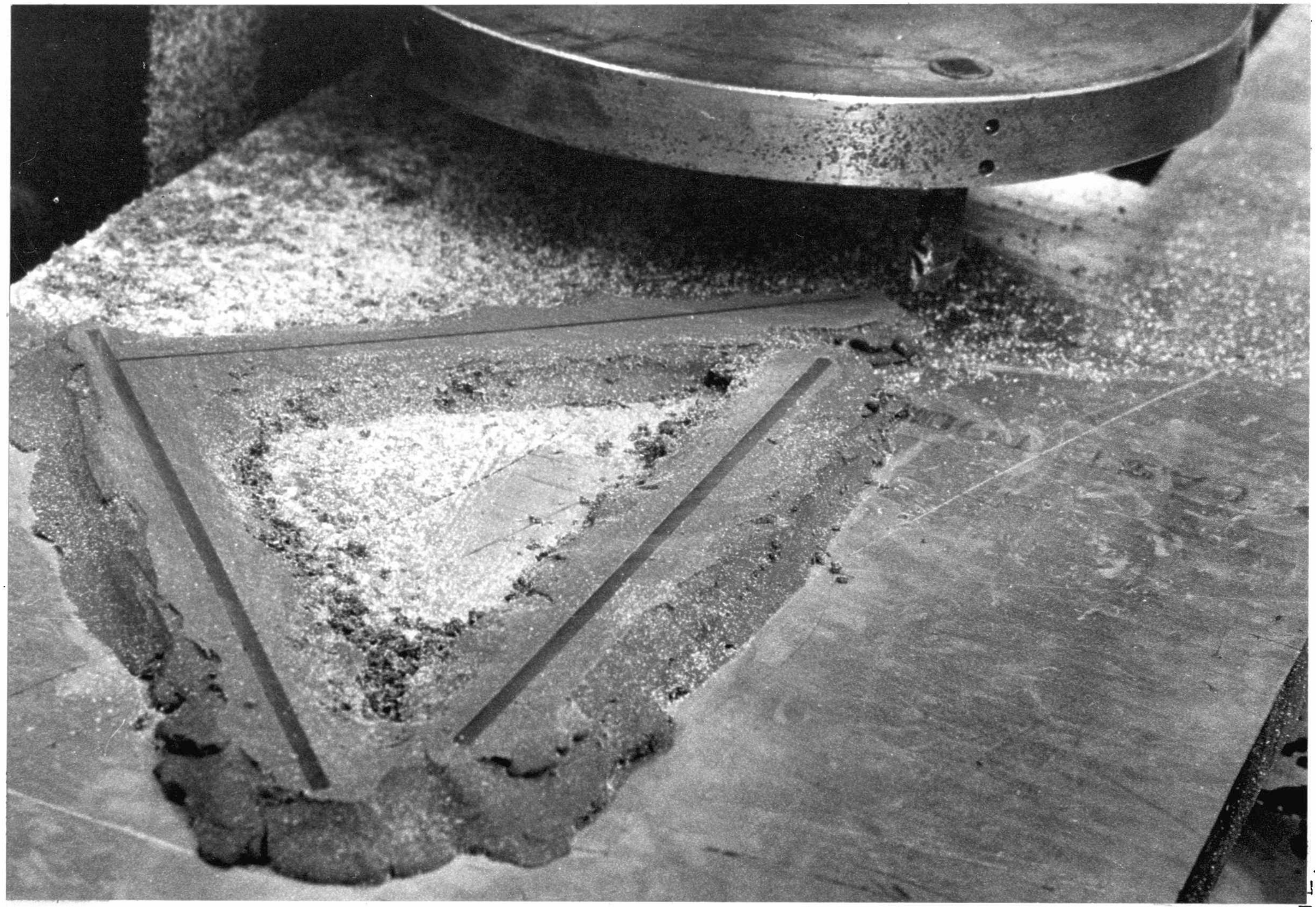

Fig. 19 - Fly-cutting T-connection model slice to finished thickness. Slices are embedded in modeling clay for support

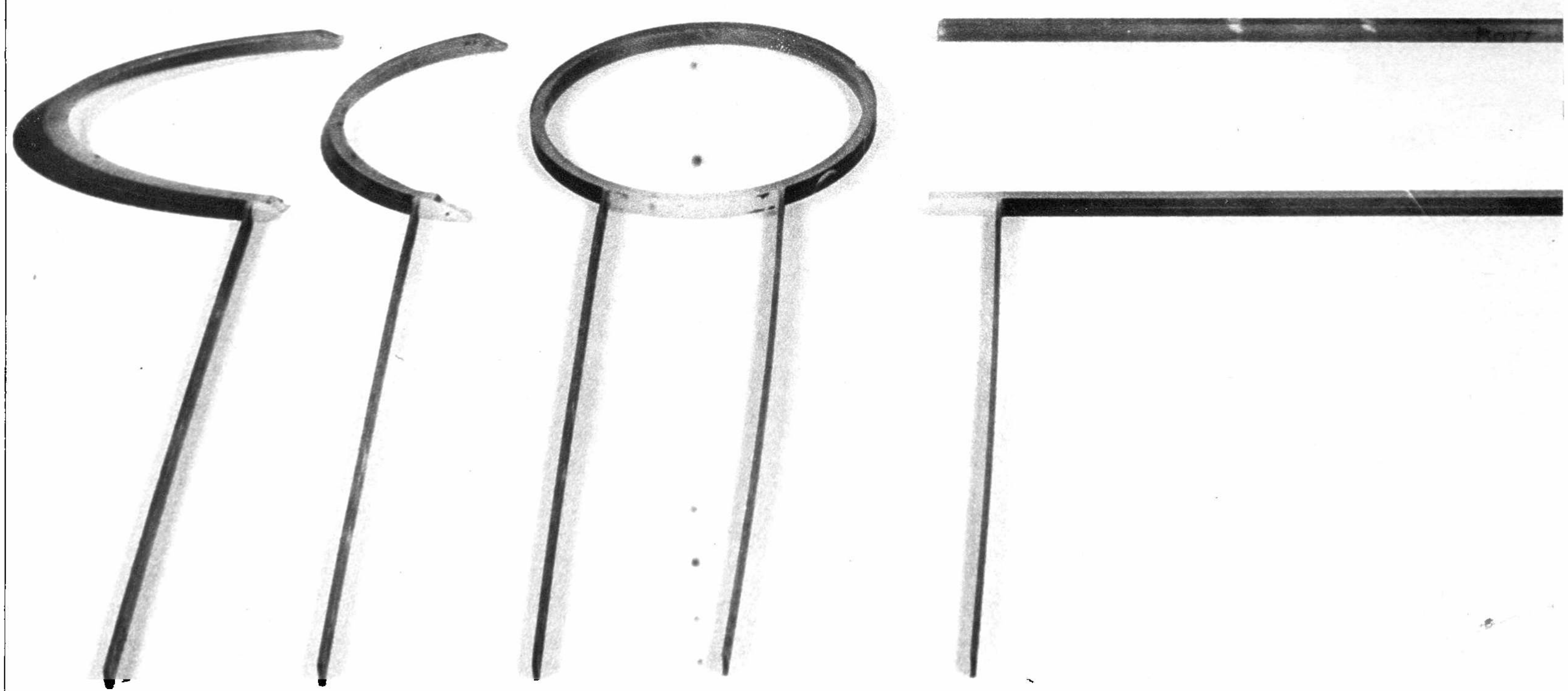

Fig. 20 - Finished slices of T-connection model

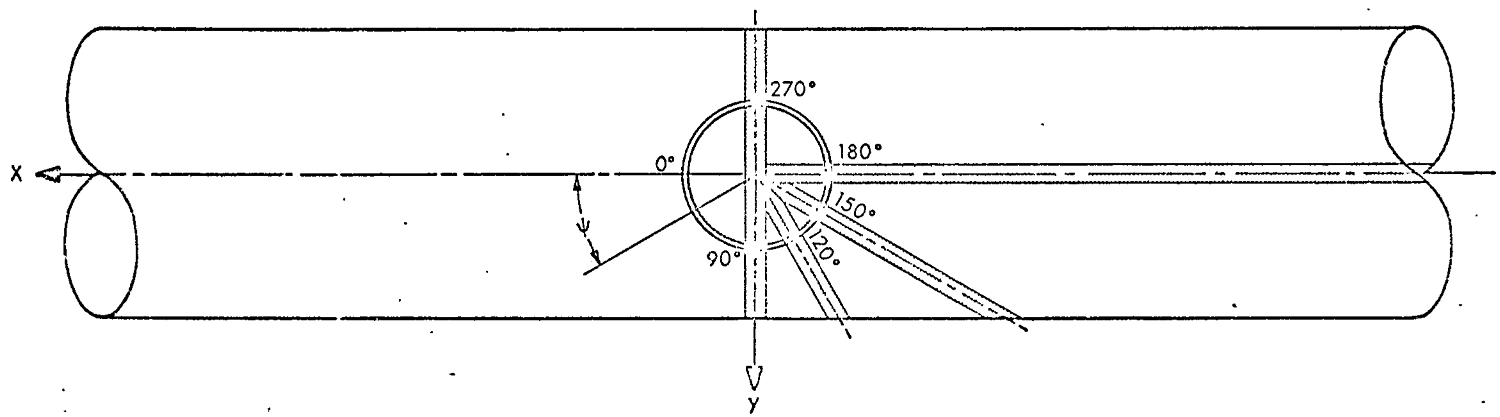

Fig. 21 - T-connection model slice locations

Table 3

T-Connection Model Slice Thickness

Model No.	Slice Thickness, inches				
	Slice Location ψ, Degrees				
	90	120	150	180[a]	
				$\varphi = 0°$	$\varphi = 180°$
1	0.246	0.224	0.221	0.224	0.226
				0.184[b]	-
2	0.233	0.233	0.237	0.234	0.237
3	0.255	0.250	0.255	0.256	0.251
	0.1985[b]				

[a] Refer to Fig. 1 for location of angle φ.

[b] Slice thinned to improve accuracy of analysis.

slices are not along principal planes. This distinction is important since it affects the method of analysis as discussed in Chapter 6.

Model Subslicing

Complete analysis of the models requires further cutting of the slices into subslices. Two types of subslices can be cut from a slice, Figure G-4:

1) surface subslice, and

2) transverse subslice.

Surface subslicing produces thin (0.015± inch) slices taken parallel to the outer and inner free surfaces of the model, Figure 22. Transverse subslicing results in taking a small parallepiped of material through the slice thickness, Figure 22.

Both types of subslices were used during the analysis of the T-connection models.

Details of the preparation of the subslices are presented in Appendix G.

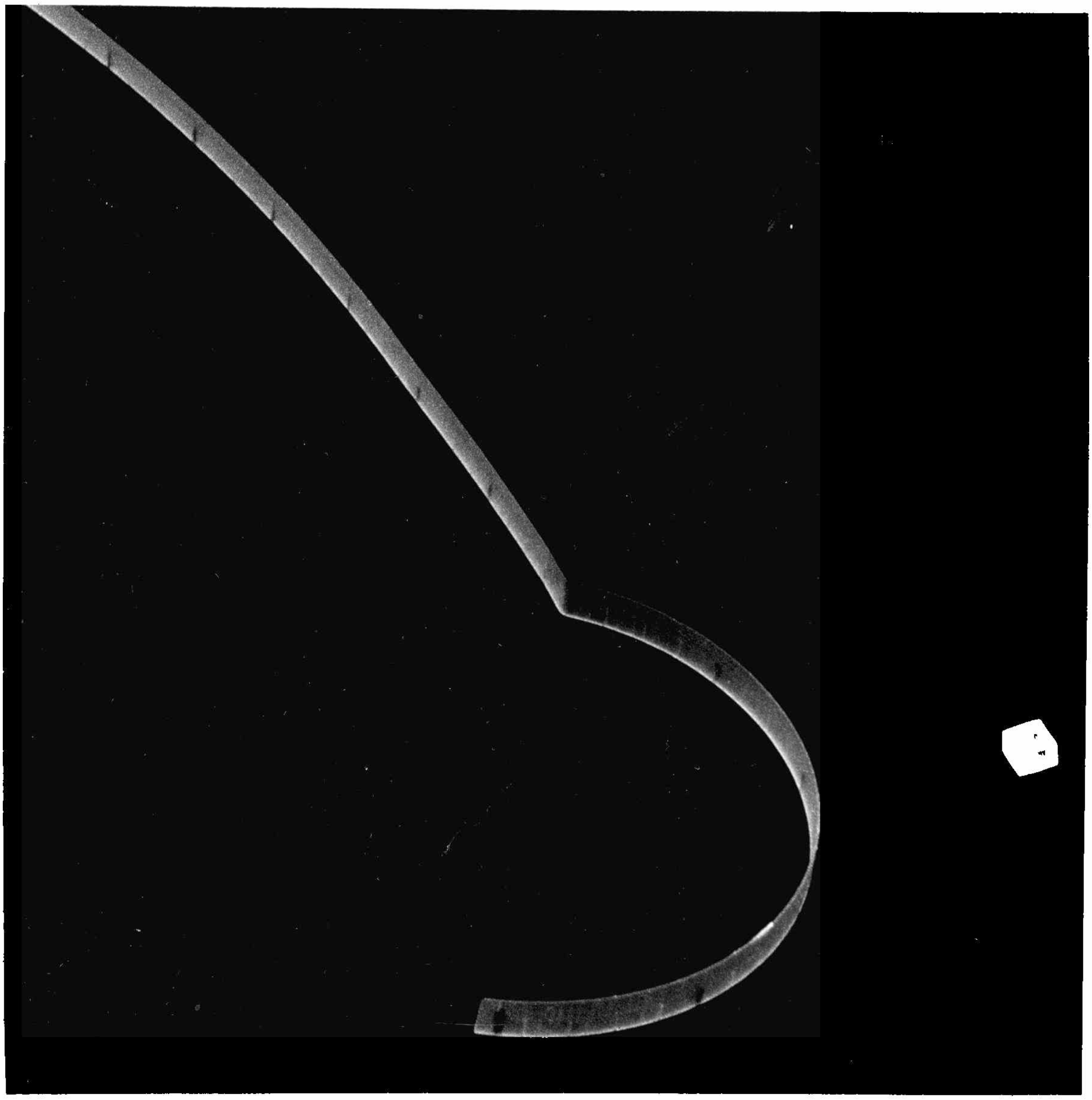

Fig. 22 - Surface subslice (left) and transverse subslice (right) cut from a T-connection model slice

Chapter 6

STRESS FRINGE ANALYSIS

As discussed in Chapter 5, photoelastic models must be cut into two-dimensional slices for analysis. Therefore, it is important to establish proper fringe development before cutting the model. This was accomplished by determining the material stress fringe constant, f_σ, from the calibration bar. If the patterns are not fully developed, the model and calibration bar can be re-stress frozen.

CALIBRATION BAR ANALYSIS

The material stress fringe constant, f_σ, was determined from equation

$$f_\sigma = \frac{P}{wN} \quad , \qquad (6\text{-}1)$$

where

P = calibration bar load

w = calibration bar width, and

N = isochromatic fringe order.

Values for w and P were obtained from Tables 1 and 2, respectively. Fringe order, N, was determined by observing the stress-frozen bar in a polariscope, Figure 23, adjusted to produce circular polarized light (Dalley, 1965). Bars were submerged in a glass tank containing 2/3 Hallowax oil and 1/3 Paraffin oil. This mixture has the

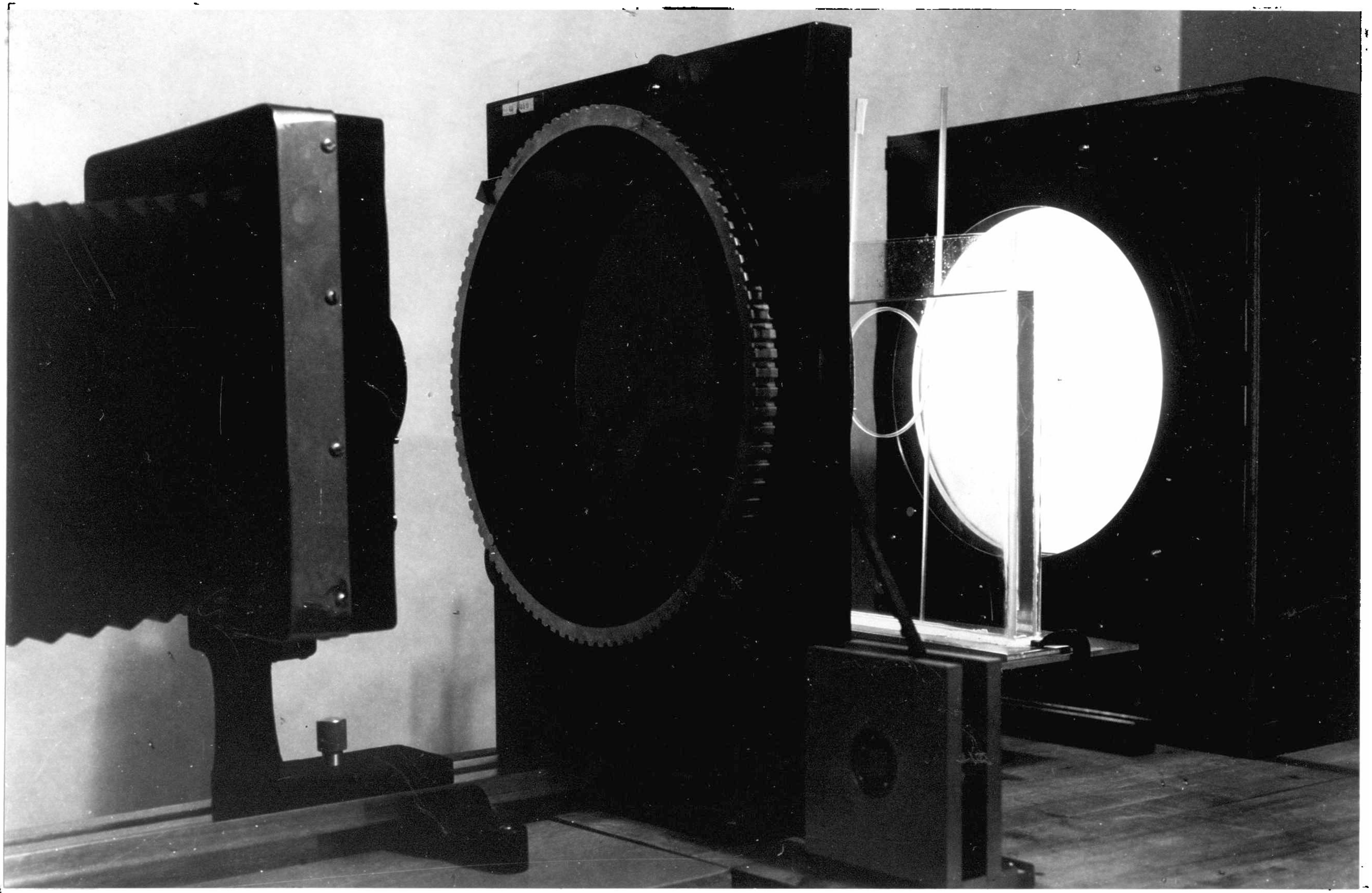

Fig. 23 - 12-inch diffused light polariscope and bellows camera

same index of refraction as the plastic. Thus, model transparency was improved without distorting the bar image.

Integer fringe orders were determined by a compensator fashioned from a stress frozen calibration bar which was milled wedge shape near the center of the shank, Figure 24. Fractional fringe orders were measured by Tardy Compensation, Appendix H and Figure 25.

The material stress fringe constants for each model were determined before slicing, Table 4.

Table 4

T-Connection Model Material Stress Fringe Constants

	Calibration Bar				
Model No.	Bar No.[a]	Load P (g)	Width w (inches)	Fringe Order	Material Stress Fringe Constant $f\sigma$ (psi/fringe/inch)
1	IB-1	941.92	0.251	3.69	2.24
	IC-1	978.36	0.253	3.58	2.38
2	2	942.20	0.251	3.78	2.19
3	3	942.10	0.251	3.89	2.13

[a] B-brace calibration bar
C-chord calibration bar.

MODEL SLICE ANALYSIS

Analysis of each slice was performed in a manner similar to that used on the calibration bars; however, since the brace thickness was only 0.050 inch, observation of the fringe pattern was aided by a telescope and reading glass, Figure 26. Each slice was submerged in Hallowax oil solution during analysis and photography to eliminate distortion caused by index of refraction changes.

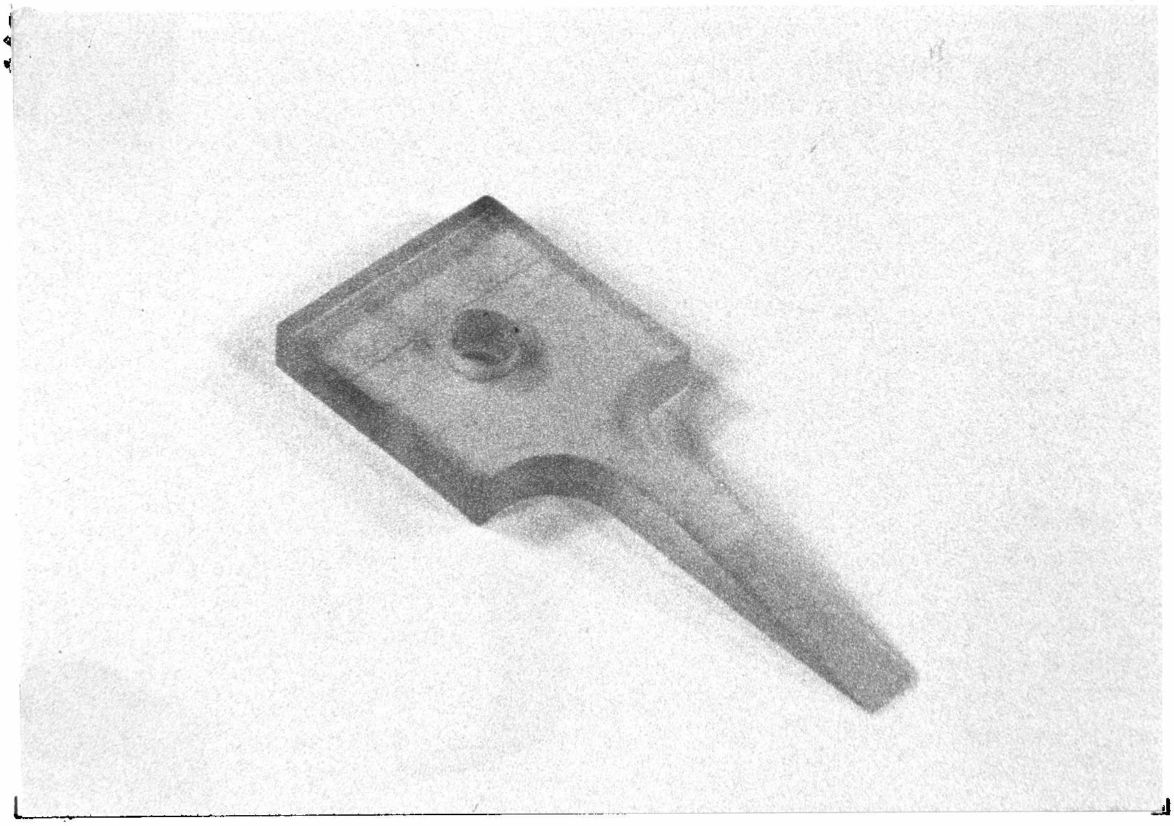

Fig. 24 - Compensator fashioned from stress frozen calibration bar

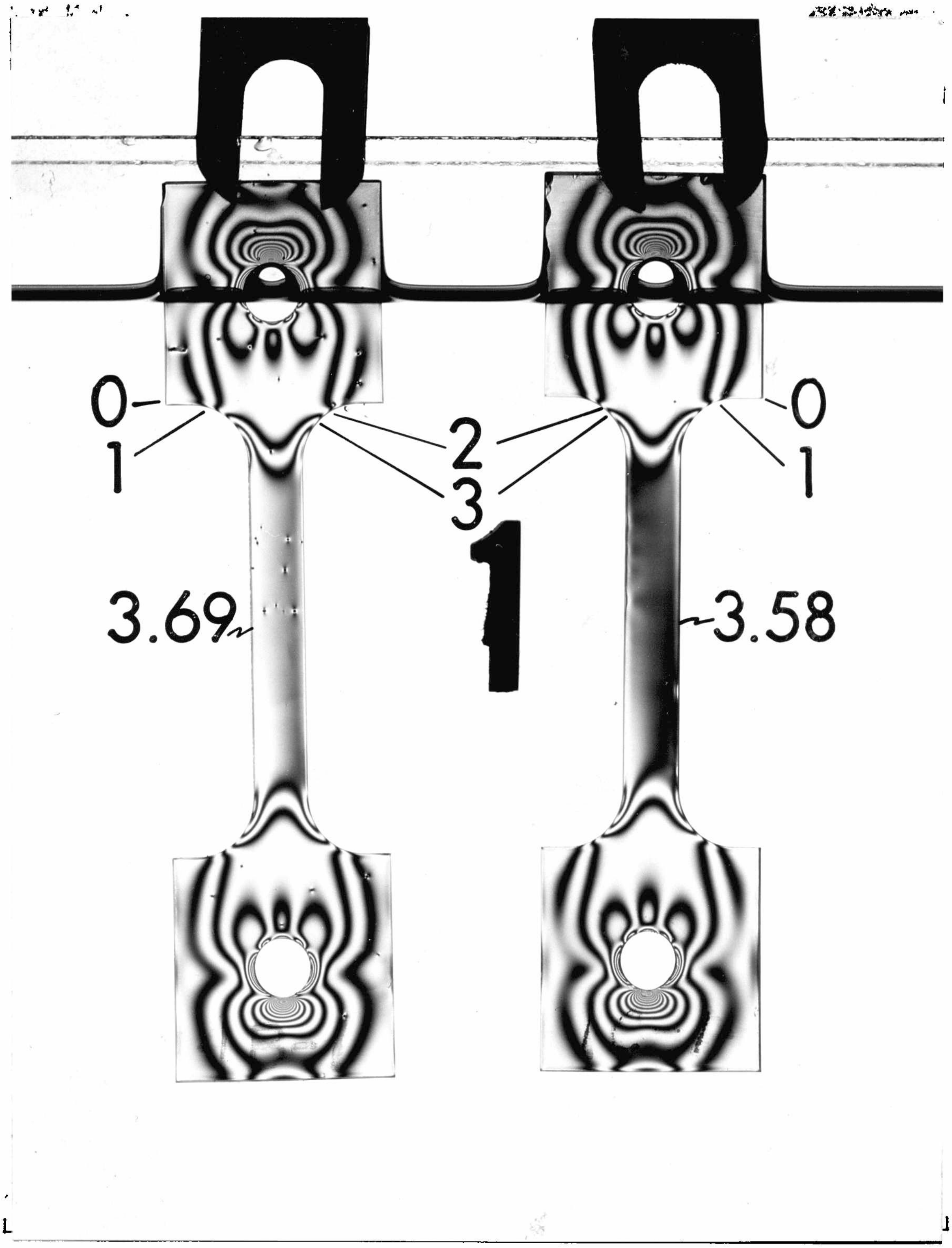

Fig. 25 - Brace calibration bar (left) and chord calibration bar (right) for T-connection Model 1: Bars are submerged in glass tank containing Hallowax oil mixture

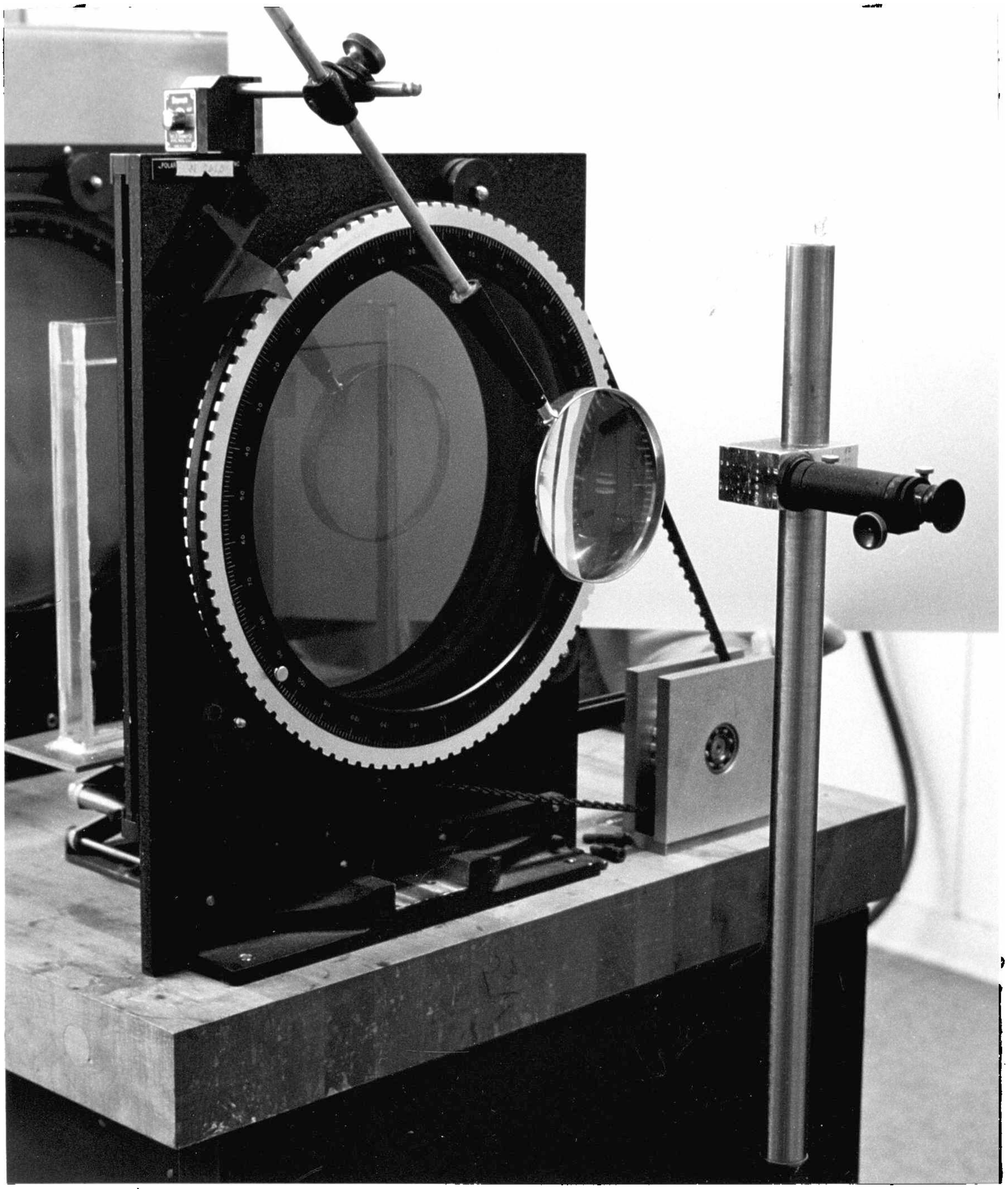

Fig. 26 - Telescope and reading glass used to improve viewing of thin portions of model slices

The fringe orders were recorded photographically as a means of accurately locating the fringes, Figure 27. During analysis of the slices from Model 1, it was learned that the fringe could be located better if lines were scribed across the slice face at 1/4-inch intervals. This technique was used during analysis of Models 2 and 3.

Photographs of the slices were taken with a bellows camera, Figure 23, using Tri-X Ortho sheet film, green light, and a Wratten 77 filter. Sharpest fringes were obtained at f32 aperature opening and 20 seconds exposure. A light field background was used while photographing so as to improve edge resolution, Figure 27.

Stresses in two directions were analyzed: (1) tangential stress, σ_t, and (2) orthogonal stress, σ_0, Figure 28. Results of the analyses are given graphically as stress concentration factors, K_t and K_0 in Appendix I. K_t and K_0 are defined as

$$K_t = \frac{\sigma_t}{\sigma_n} \qquad K_0 = \frac{\sigma_0}{\sigma_n} \tag{6-2}$$

where

σ_t = tangential stress at the point of interest, psi, Figure 28

σ_n = nominal tangential stress in the brace remote from the intersection curve, psi, and

σ_0 = orthogonal stress at the point of interest, psi, Figure 28.

Stress concentration factors, equation (6-2), were selected to present the data because of their extensive use in offshore engineering literature (Toprac and Brown, 1966).

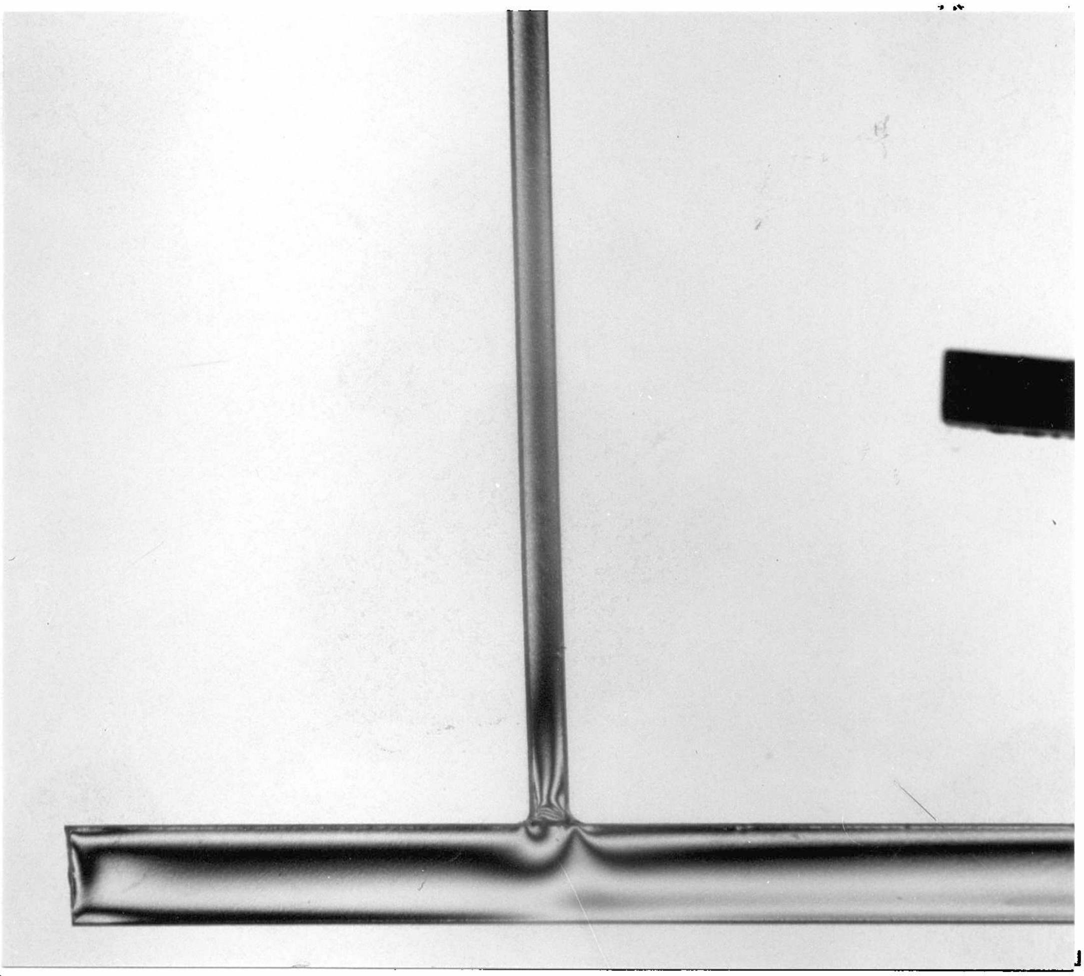

Fig. 27 - Light field photograph of T-connection Model 1 - 180° slice $f_{\sigma} = 2.38$ psi/fringe/inch, $h = 0.224$ inch, $h_b = 0.050$ inch, and $h_c = 0.147$ inch

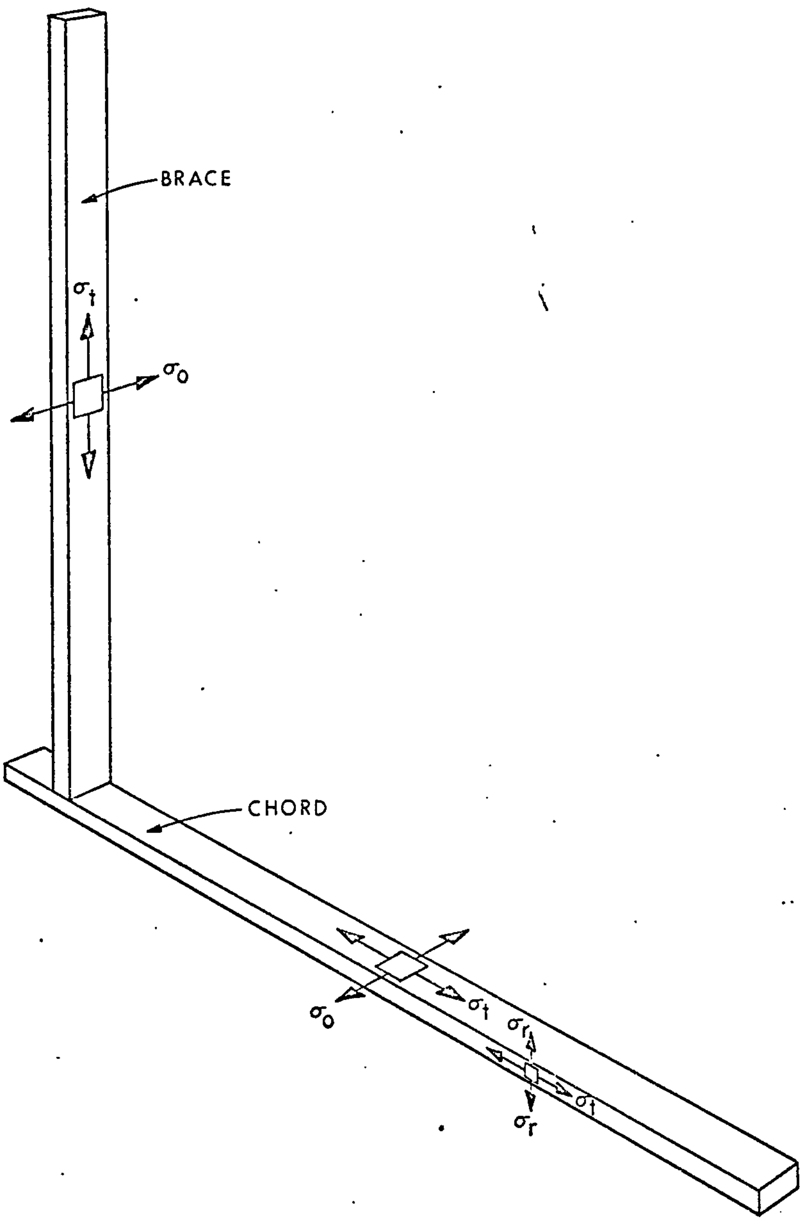

Fig. 28 - 180° slice showing direction of tangential, σ_t, and orthogonal, σ_0, stresses on chord and brace surfaces

Nominal stress, σ_n, was calculated from

$$\sigma_n = \frac{P}{A} = \frac{P}{\pi (D_b - h_b) h_b} \qquad (6\text{-}3)$$

where

P = load imposed on the model brace, pounds, Table 2

A = brace cross sectional area, square inches

D_b = outside diameter of brace, inches

h_b = wall thickness of brace, inches.

Tangential Stress Analysis

Fringe patterns associated with the tangential stresses were analyzed by viewing the slice normal to the cut surface, that is, parallel to σ_0, Figure 28. Patterns seen along the edges of the slice, Figure 27, are representative of tangential stresses.

In general, the magnitude of stress can be determined along principal planes of symmetry from the fringe patterns using

$$\sigma_t - \sigma_0 = \frac{N f_\sigma}{h}, \qquad (6\text{-}4)$$

where

$\sigma_t = \sigma_1$ = maximum principal stress, psi

$\sigma_0 = \sigma_2$ = minimum principal stress, psi

N = stress fringe order in the "t" direction

f_σ = material stress fringe constant, psi/fringe/inch

h = slice thickness, inches.

Along free edges $\sigma_2 = \sigma_0 = 0$, Figure 28. Thus, equation (6-4) reduces to

$$\sigma_t = \frac{Nf_\sigma}{h} \tag{6-5}$$

Equations (6-4) and (6-5) are not applicable to the chord sections of the 120° and 150° slices, Figure 21, since viewing normal to the slice cut surface does not eliminate σ_0. Oblique incidence analysis must be used in these portions of the model (Leven, 1966), but since the stresses are known to be low in these areas (Toprac and Brown, 1966), these chord slices were not analyzed.

Values of σ_n were determined by computer for each model, Table 5.

Table 5

Average Tangential Stress in T-Connection Model Brace

Model	σ_n psi
1	8.39
2	8.00
3	8.48

N was determined as integer fringe orders where possible; however, to improve accuracy, fractional fringe orders were determined by Tardy Compensation, Appendix H, at many of the lines scribed on the slice faces. In areas of high stress, that is, at or near the intersection curve, values of N determined from full thickness slices (0.22 to 0.26 inch) were checked by thinning critical areas of the slices, Table 3.

The tangential stress concentration factors, K_t, were calculated using equation (6-5) and presented graphically in Appendix I.

Orthogonal Stress Analysis

The orthogonal stresses, σ_0, were determined for the five slices of Model 1, Figures I-1 through I-5. The results of this analysis indicated the tangential stresses were critical. Thus, orthogonal stresses for Models 2 and 3 were not determined.

The orthogonal stresses were analyzed from fringe patterns observed in subslices, Appendix G. Two types of subslices were used: (1) surface subslices, and (2) transverse subslices, Figure G-4. Surface slices were viewed in the polariscope normal to the model surface, that is, parallel to σ_r, Figure 28. Orthogonal stresses were calculated from equation (6-4) using the previously determined values of σ_t at the points of interest substituted into the equation. The correct form of equation (6-4), that is $\sigma_t - \sigma_0$ or $\sigma_0 - \sigma_t$, was ascertained by observing the direction of the isoclinic fringes. Equation (6-4) was used as shown if the isoclinic was parallel to the "t" direction. If the isoclinic was parallel to "o", then the left side of the equation was reversed.

Transverse subslices were viewed in the polariscope normal to the free surfaces, that is, parallel to σ_t, Figure 28. Orthogonal stresses were determined from an equation analogous to equation (6-5) since σ_r was zero at the free surface.

Chapter 7

ANALYSIS OF RESULTS

Three photoelastic T-connection models were fabricated, stress frozen, and analysed during this investigation. The analysis was performed on slices, Figure 21, cut from the stress frozen models. Because of symmetry of the models, five slices were adequate to provide representative stress distributions, Appendix I.

T-connections were selected because of (1) frequent use in platforms, and (2) simplicity of design. Thus, they represent a logical beginning for an in-depth investigation of elastic stress distributions in tubular connections. In addition, analysis of T-connections may be considered as an upper bound solution of the maximum stress in more complex in-plane connections, i.e., Y or K-connections, since the literature (Toprac 1966c) suggests stress concentrations are higher in T-connections than in other in-plane connections.

QUALITATIVE ANALYSIS

The visual presentation of stress distributions afforded by photoelasticity is a significant advantage offered by this technique because areas of high stress gradient can quickly and easily be discerned. Even a casual study of the stress fringe patterns suggests areas of probable high or low stress concentration because of the presence of closely spaced patterns or lack of patterns, respectively.

Thus, it is readily apparent which areas require careful analysis. This concept is shown in Figures 29a, b, and c, which are photographs of the intersection weld areas (90° slices) of photoelastic Models 1, 2, and 3, respectively. It is apparent that (1) the maximum stress probably occurs at the intersection weld toe, because of the high density of fringes, and (2) the magnitude of stress concentration increases as the chord becomes thinner because of the increasing number of fringes. Carrying qualitative analysis a step farther results in making a reasonable selection of the probable best design, i.e., all other things being equal, the connection with the thickest chord, Figure 29a, would be preferred since the magnitude and gradient of stress appear smallest.

MODEL SCALING

The validity of any experimental analysis depends on the accuracy with which the prototype is modeled, fabricated, and loaded. Scaling factors were selected carefully to provide true models of prototype connections. Also, the magnitude of load was purposely restricted to assure development of elastic stresses.

Modeling

The experimental stress analysis is limited to in-plane T-connections having the dimensionless ratios shown in Table 1. While restricted in number, the ratios are representative of those either in use on existing platforms or on platforms under construction. The current trend is toward thick chord members, a move which is well founded based on the results of this photoelastic investigation.

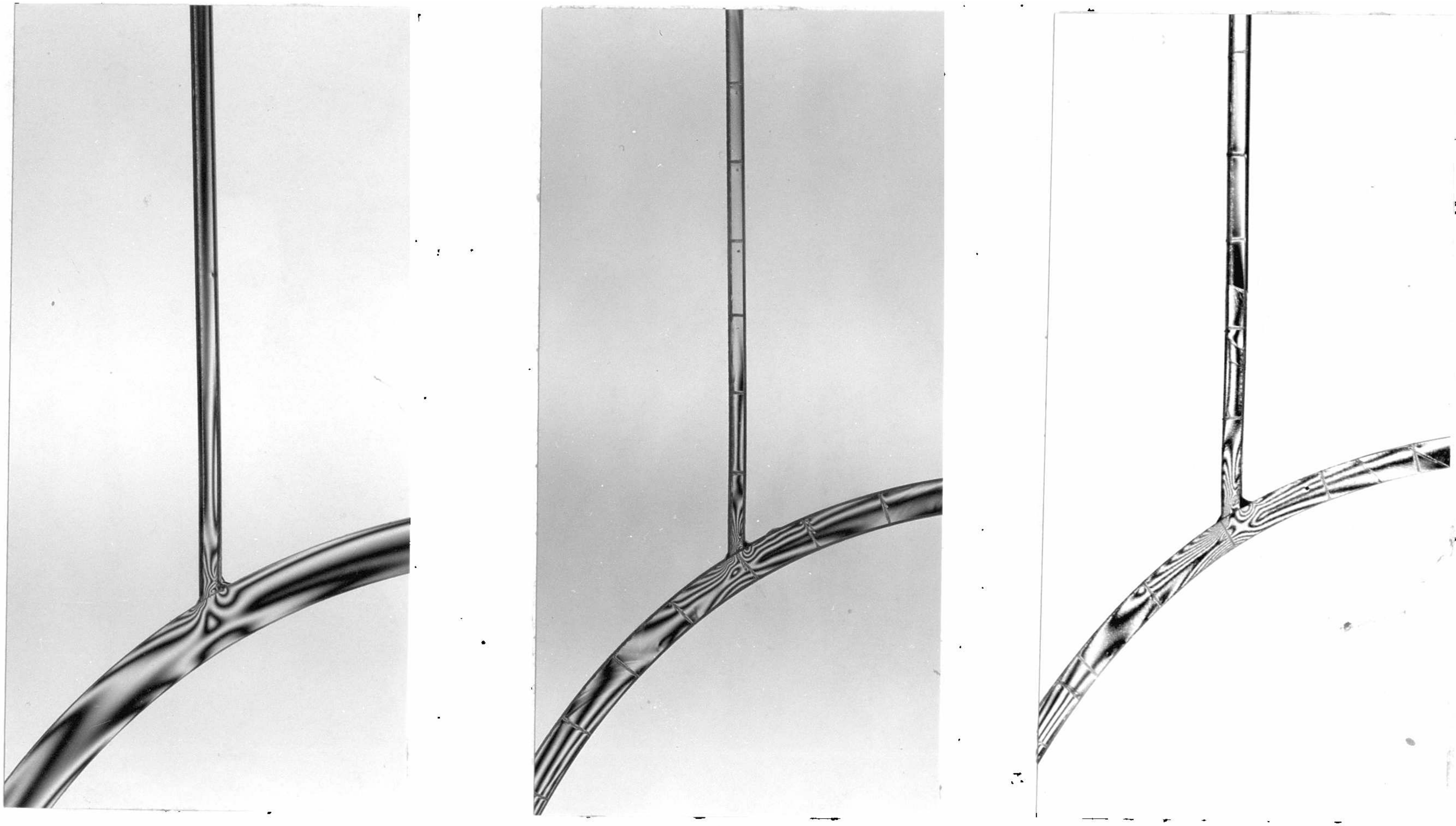

a b c

Fig. 29 - Qualitative comparison of stress concentrations in T-connection models having a) $\tau = 0.354$, b) $\tau = 0.486$, and c) $\tau = 0.610$

The scaling of tubular members is relatively simple and well documented (Murphy 1950). On the other hand, scaling of butt welds, as used at the chord-to-brace intersection, presents considerable difficulty. This is particularly true of steel models because of the difficulty of controlling the weld deposit size in relation to the model size. Comparisons of welds from steel models (Toprac 1966c) with those shown in Figure 29 indicate that the photoelastic model welds are in better proportion to the brace and chord wall thickness. In general, the weld size for steel model approximates the brace wall thickness whereas the photoelastic weld is about 20 percent of the brace wall thickness and thus closely conforms to prototype welding practices.

The major difference between the prototype weld and the photoelastic weld is in the weld reinforcement existing inside of the brace. The photoelastic weld has a definite weld bead visible on the inside surface of the brace, Figure 29, that does not exist in the prototype or steel model connection. This weld probably has little effect on the stress distribution at the intersection since in steel connections every effort is made to provide a full penetration weld of the brace to the chord. If the photoelastic inside weld reinforcement has an effect, it most probably is to decrease the stress concentration at the intersection because of the increased area of contact between brace and chord.

<u>Fabrication</u>

Literature (Godden 1969) indicates that plastic model components made by machining have inherent inaccuracies, i.e., out of roundness and taper. During this investigation, careful measurements were made of each model after assembly, Appendix B. The measurements indicate a maximum (1) ovality of 0.25 percent, and (2) taper of 0.001 inch/inch of length, which are well within permissible limits (API 1969) for commercial tubular components for platforms. In addition, the accuracy of the photoelastic models compares favorably with the one percent accuracy for plexiglass true models of a pipeline Y-connection recently reported by Godden (1969).

Loading

Accurate loading of the photoelastic models is adequately demonstrated by the symmetry of the connections after stress freezing, Appendix B. Also, the absence of bending moments applied to the brace during loading can be noted from (1) lack of change in the brace end-angle, and (2) uniformity of elongation of the brace. Further, the magnitude of load was satisfactory since adequate fringe patterns were formed, Figure 29, without excessive deformation as discussed below.

CONNECTION DEFORMATIONS

Directly associated with the accuracy of the stress analysis of the photoelastic models is the change in shape of the models during stress freezing. Since stress freezing locks in deformations, it must be recognized that the models will deform under the imposed load.

The deformation of the individual components is representative of the shape taken by the prototype connection under similar load; however, the correlation only can be qualitative since the elastic modulus and Poisson ratio for plastic are vastly different from those for steel.

Photoelastic Model Deformations

The photoelastic model lends itself admirably to the observation of deformations of tubular connections under load because the displacements are large and the model is sufficiently small to permit accurate measurements. Careful measurements of brace and chord diameters, lengths, and end-diaphragm angular changes were made after each model was stress frozen.

The measurements indicate that both the chord and brace become oval shaped when a tensile load is applied to the brace end, Figure 30. As would be expected, the chord cross section elongates in the direction of the load application; however, the brace cross section elongates in the plane normal to the chord generator; i.e., the brace diameter shortens parallel to the chord generator.

Chord radial deformations. Chord diameters were measured before and after stress freezing in the XY and XZ planes, Figure 30, and Appendix B. These planes were selected because they represent the principal planes of symmetry and as such they would experience the maximum displacements. The chord ovalled as a result of imposing a tensile load on the brace, Figure 10. The long axis of the chord oval was parallel to the Z-axis, Figure 31, and the short axis was parallel to the Y-axis, Figure 32. As expected, the ovalling was more pronounced at the center of the chord than at the ends because of the effect of the end diaphragms and the application of the load at the center of the model.

The maximum chord displacement occurred along the generator passing through the brace axis, apex generator, Figure 33. The

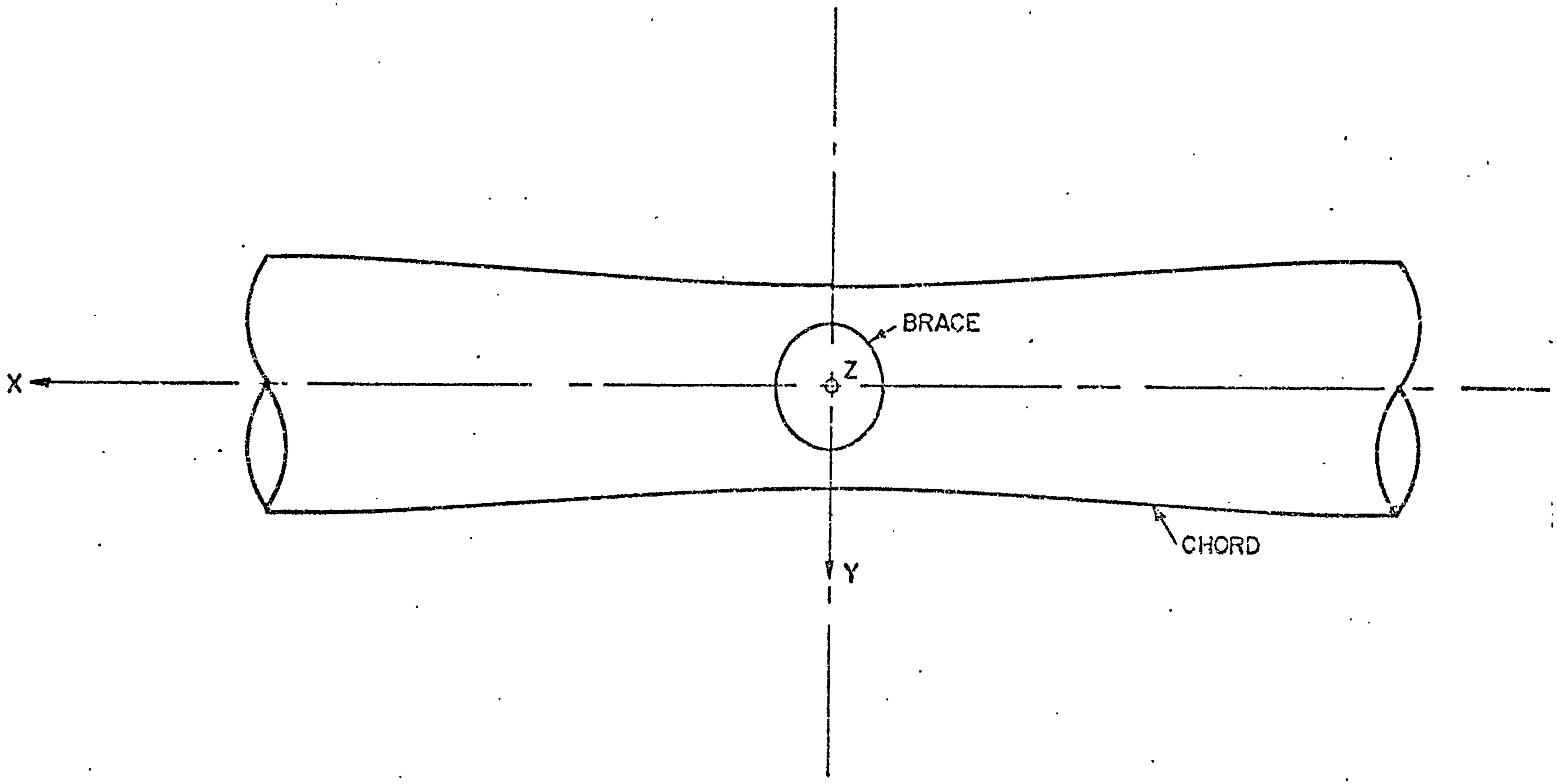

Fig. 30 - Schematic representation of deformed shape of T-connection models after stress freezing

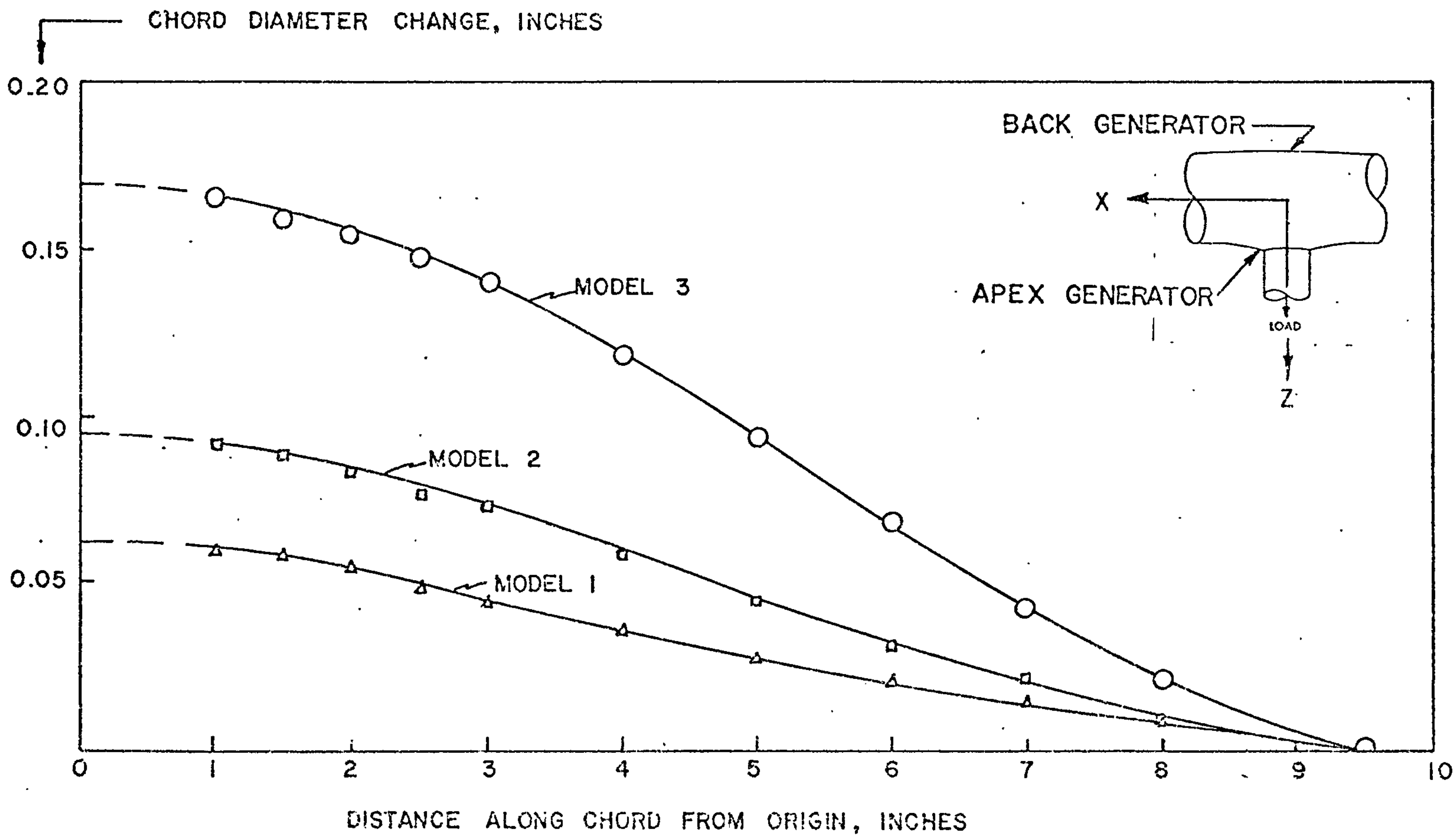

Fig. 31 - Chord diameter change in XZ plane resulting from stress freezing

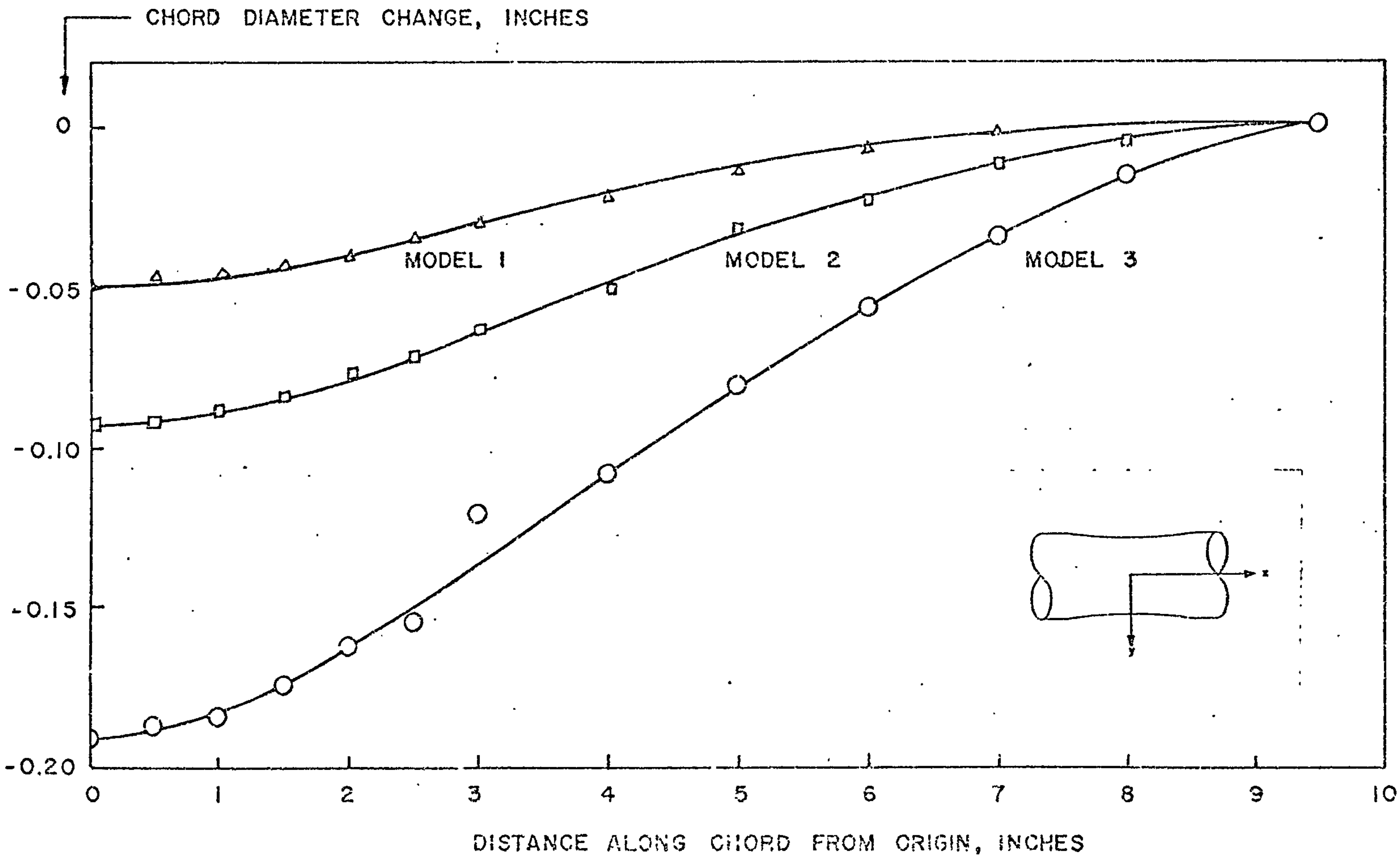

Fig. 32 - Chord diameter change in XY plane resulting from stress freezing

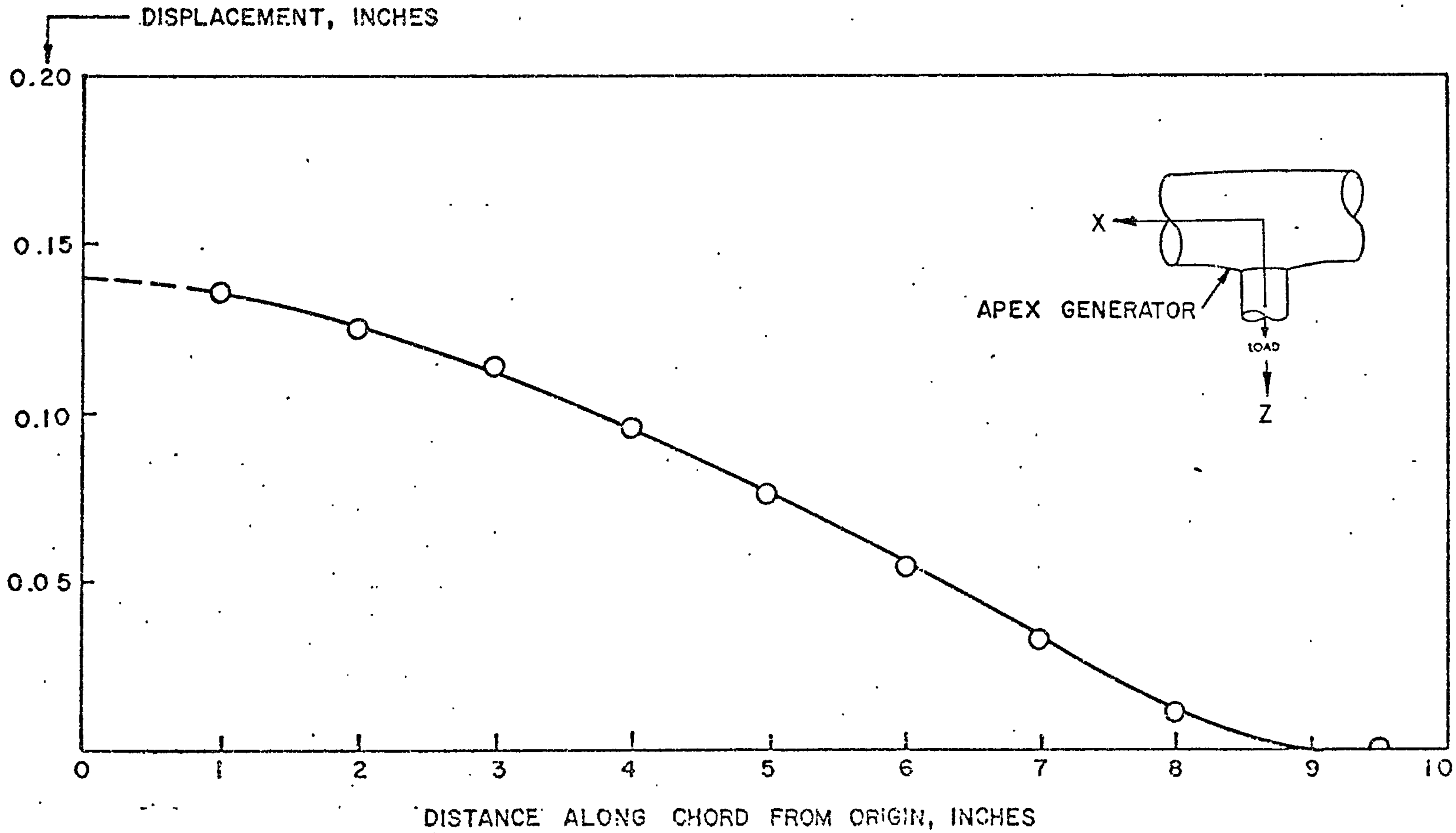

Fig. 33 - Profile of chord APEX generator resulting from stress freezing Model 3

deformation of the chord generator opposite the brace, i.e., back generator, was relatively small. For Models 1 and 2, this deformation was so small that no measurements were considered necessary. Sub-slicing of the models precludes the possibility of obtaining these measurements now. However, the displacement of the back generator of Model 3 was visually apparent and measurements were taken. As a result of the brace tensile load, the back generator was displaced outward away from its unloaded position, Figure 34. This movement suggests (and was confirmed by analysis of the model slices) that large bending stresses are imposed on the chord by the brace loading.

Comparing the radial deformations parallel to the Y and Z-axis shows that the maximum deformation occurs parallel to the Z-axis, Figures 31 and 32, and is equal to 4.75 percent of the original chord diameter, Table 6. This magnitude of radial deformation is less than half of the maximum permissible deformation of 10 percent which would preclude satisfactory analysis of elastic stress distributions in photoelastic models (Murray 1969). Based on the geometry of the connections and the loads imposed during this study, deformations would exceed the maximum permissible amount at a τ-ratio of about 0.75, Figure 35. Thus, in order to stress freeze a model having a τ-ratio of 1, the load would have to be reduced.

The chord end-diaphragms appear to have an important effect on the shape of the chord deformed shape since the chord cross section becomes round close to the diaphragm, Figure 34. It is believed that the oval shape would persist for a greater distance if the chord was longer.

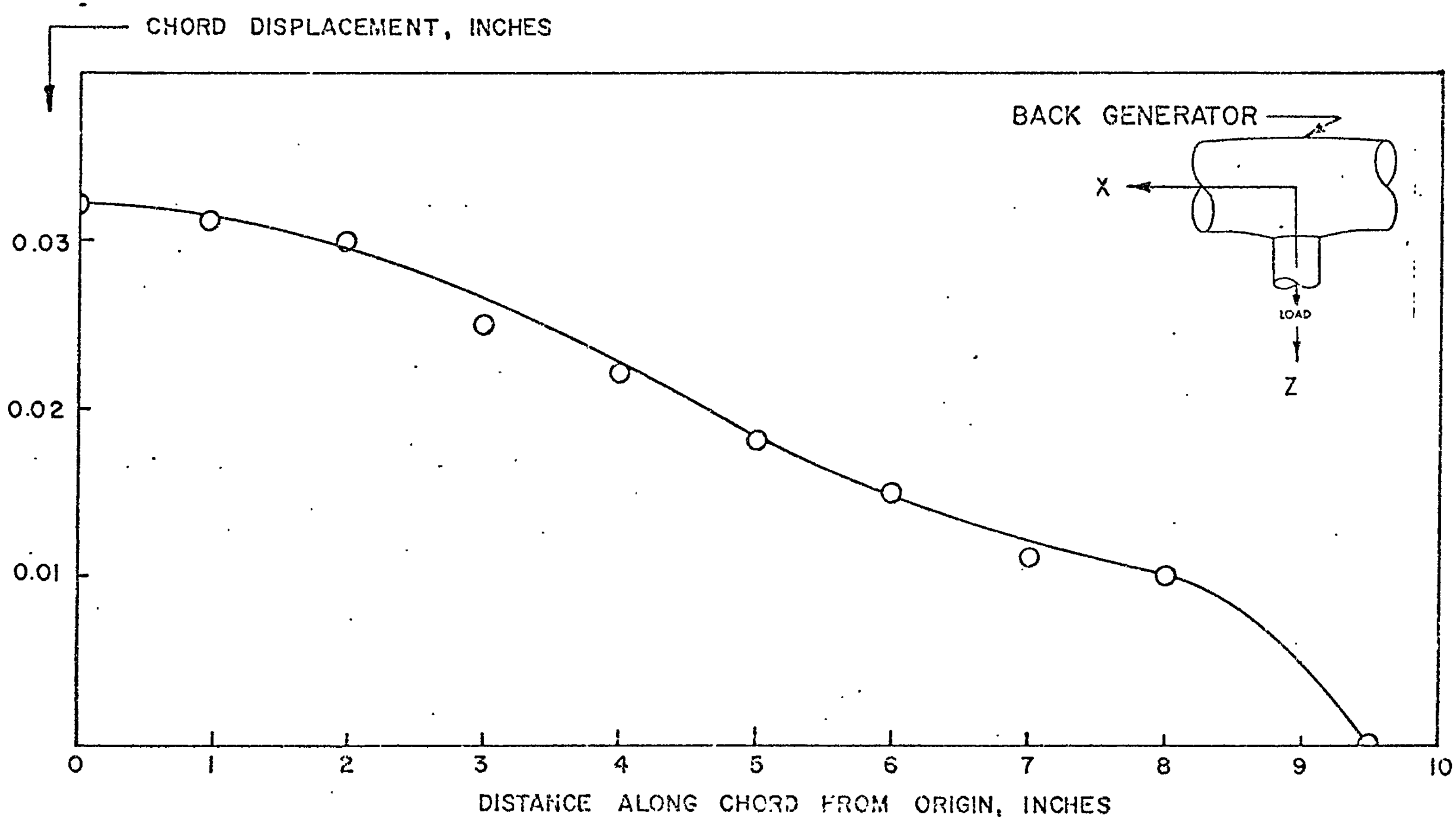

Fig. 34 - Profile of chord back - generator resulting from stress freezing Model 3

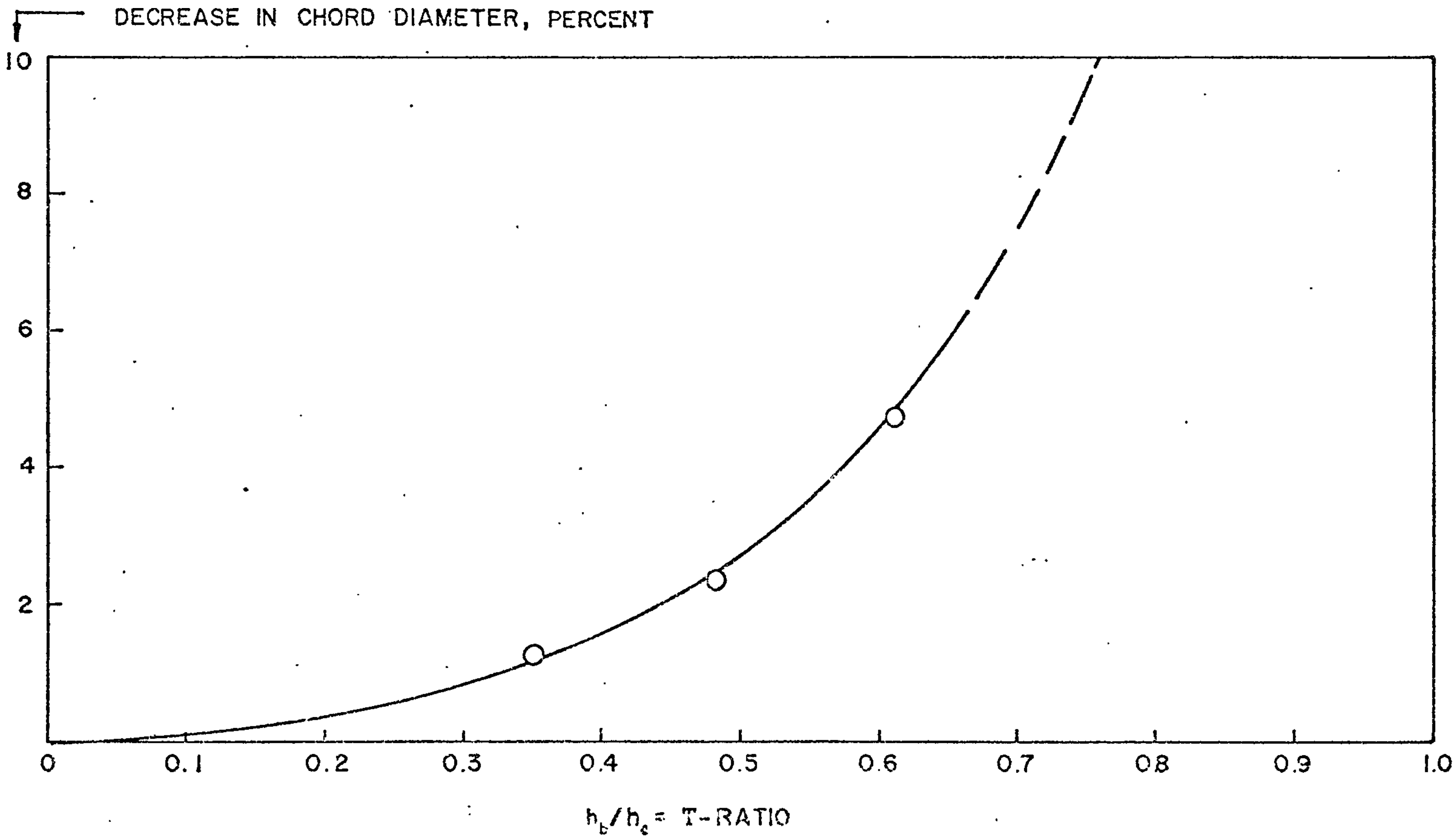

Fig. 35 - Limiting τ-ratio to preclude excessive deformation

Table 6

T-Connection Model Maximum Deformations

Model	Diameter				Length[a]				Angular Displacement Chord	
	Chord		Brace		Chord		Brace			
	XY-Plane Percent[b]	XZ-Plane Percent[b]	XZ-Plane Percent[b]	YZ-Plane Percent[b]	Back Generator Percent[c]	Apex Generator Percent[c]	Right Percent[c]	Left Percent[c]	Right in	Left in
1	-1.28	+2.39	-0.54	+0.45	-0.11	+0.13	+0.19	+0.16	+0.026[d]	+0.028[d]
2	-2.34	+2.29	-0.80	+0.76	-0.05	+0.17	+0.16	+0.17	+0.025	+0.023
3	-4.75	+4.11	-1.19	+0.93	-0.14	+0.17	+0.17	+0.16	+0.022	+0.021

[a] Measured in XZ plane.

[b] Expressed as a percentage of component diameter. Plus sign indicates an increase in dimension; minus sign indicates a decrease in dimension.

[c] Expressed as a percentage of component length. Plus sign indicates an increase in dimension; minus sign indicates a decrease in dimension.

[d] Plus sign indicates inward displacement from vertical measured from bottom of chord after stress freezing, Figure B-1.

Chord axial deformation. The chord undergoes a marked axial length change under load, Tables 6 and 7, i.e., (1) the chord apex generator and center line lengthen and (2) the chord back generator shortens, Figure 36. The back generator length measurement after stress freezing, for Model 3, appears in error since the slope of the curve representing Model 3 is different from the other two models, Figure 36. This is seen more clearly in Figure 37, which compares the change in half chord length with the average end displacement. Here the comparison suggests an error of about 0.008 inch in the measured half-length change for Model 3. Unfortunately, no method is available to recheck the accuracy of the chord measurement since slicing destroyed the model. Applying the 0.008 inch correction to the chord length of Model 3, Table 7, the chord end-displacement correlates well with the values for the other models, Figure 36.

Table 7

Photoelastic T-Connection Model Chord Axial Deformations After Stress Freezing

Model	Chord Half Length Change	
	Along Apex Generator inches	Along Back Generator inches
1	0.0129	-0.0105
2	0.0169	-0.0051
3	0.0163	-0.0134 (-0.0054)[a]

[a] Corrected by 0.008 inch based on Figure 37.

Chord end displacements, as measured by angular displacements of the chord end-diaphragms, Table 8, are reasonably similar, i.e.,

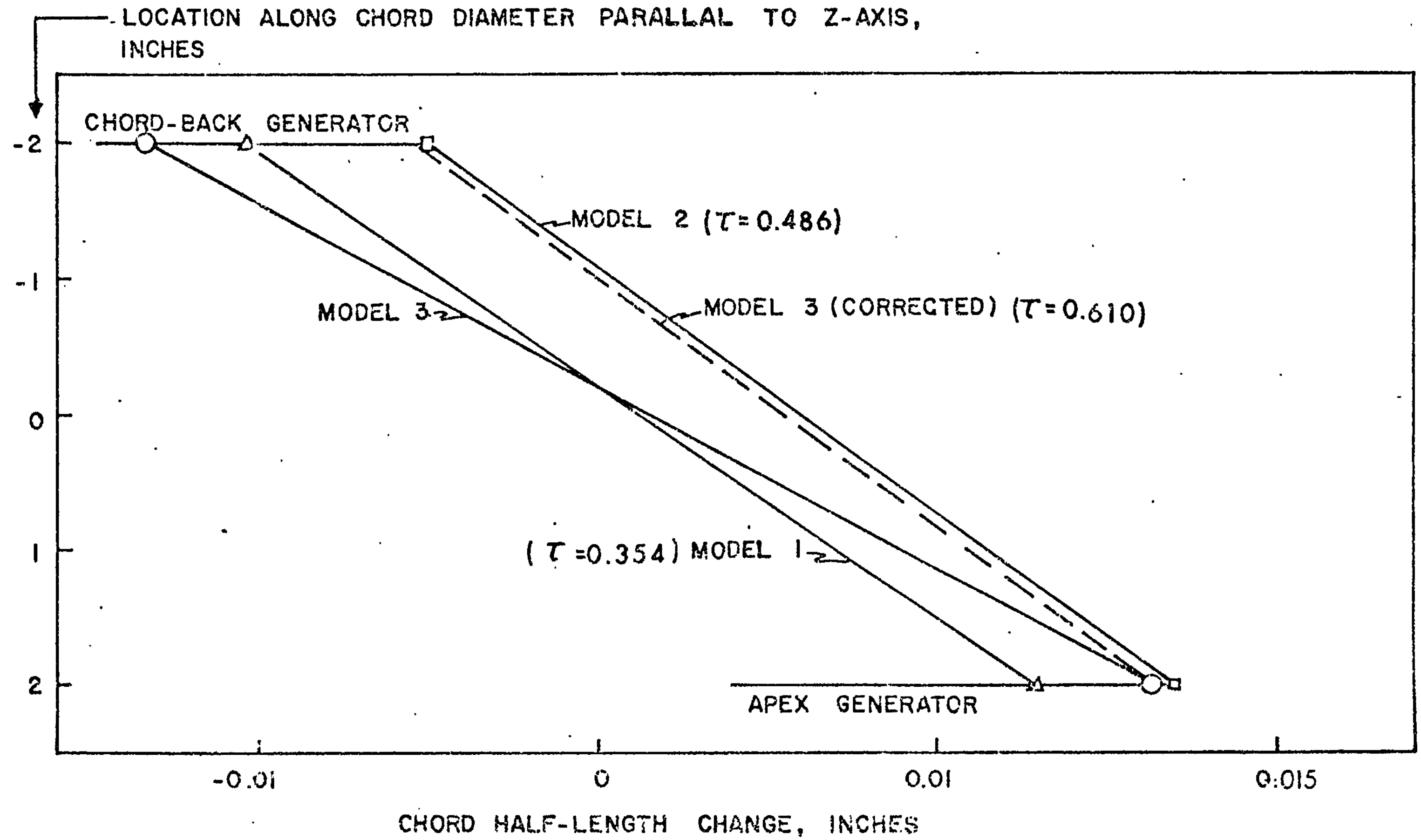

Fig. 36 - Chord end displacements resulting from stress freezing

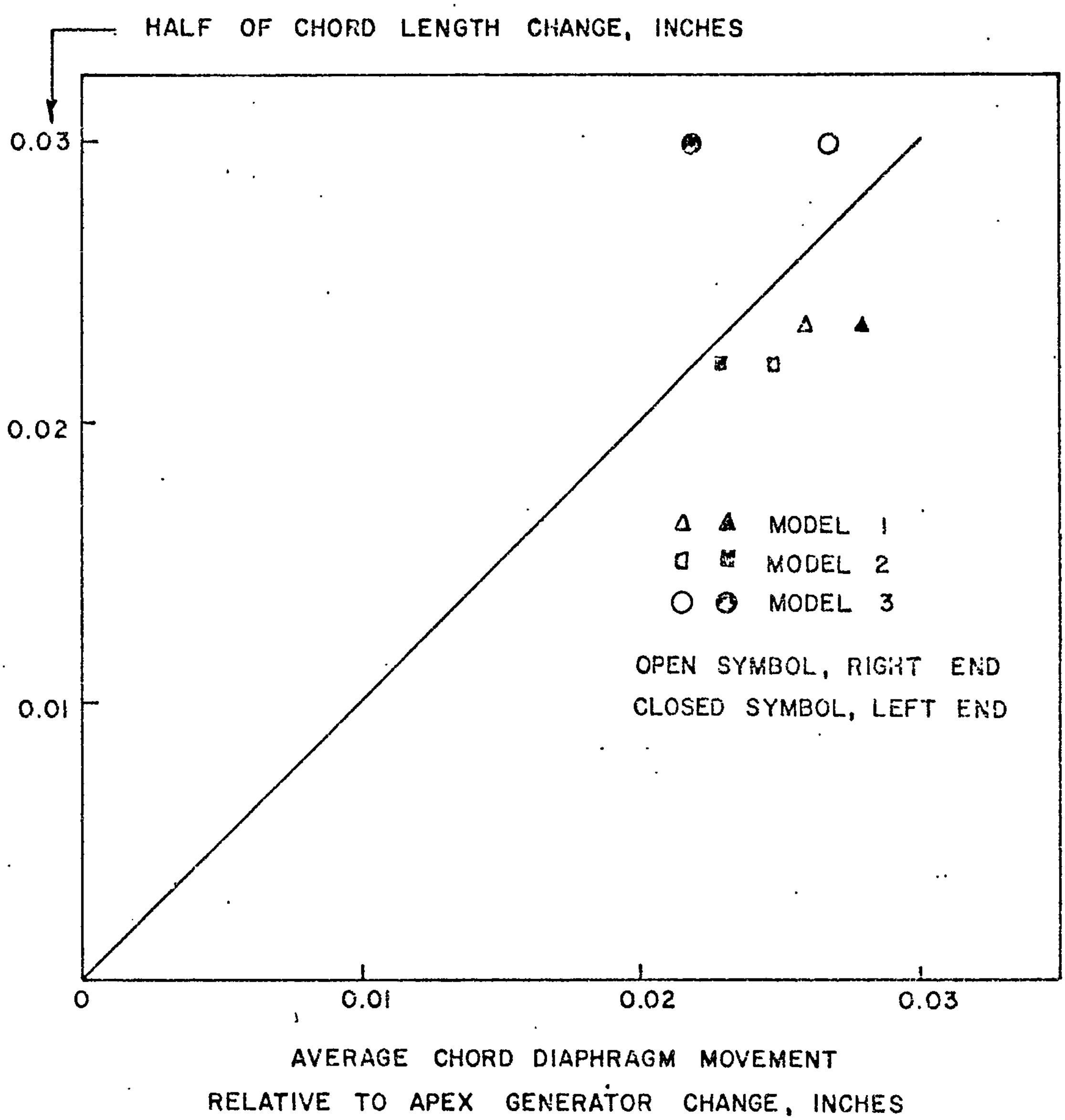

Fig. 37 - Comparison of chord axial length change resulting from stress freezing

0.004 inch variation, Figure 38. A maximum variation of 0.005 inch in the chord half length is evident from Figure 36 (based on using the Model 3 corrected value). In addition, Figure 36 suggests that the magnitude of chord length reaches a maximum somewhere near a τ-ratio of 0.5 for the models tested. No conclusion can be drawn from Figure 38 relative to the end diaphragm angular change since (1) at the right-hand end of the chord, the displacement increases as the τ- and γ-ratios decrease, and (2) at the left-hand end, the displacement shows no consistent trend. It is believed that the trend indicated at the right-hand end is correct since the back generator radial displacement is small, thus causing a substantial end rotation even for moderate apex generator lengthening. Slicing of the model preparatory to analysis precludes the possibility of re-assessing the end diaphragm rotations.

Table 8

Photoelastic T-Connection Model Chord-End Diaphragm Displacements After Stress Freezing

Model	Chord-End Diaphragm Movement Relative to Apex Generator Length	
	Left-Hand End inches	Right-Hand End inches
1	0.028	0.026
2	0.023	0.025
3	0.027	0.022

Brace radial deformation. The brace also experiences ovalling as the result of axial loading. It is reasonable to expect that the decrease in the chord transverse diameter, Figure 32, would cause a

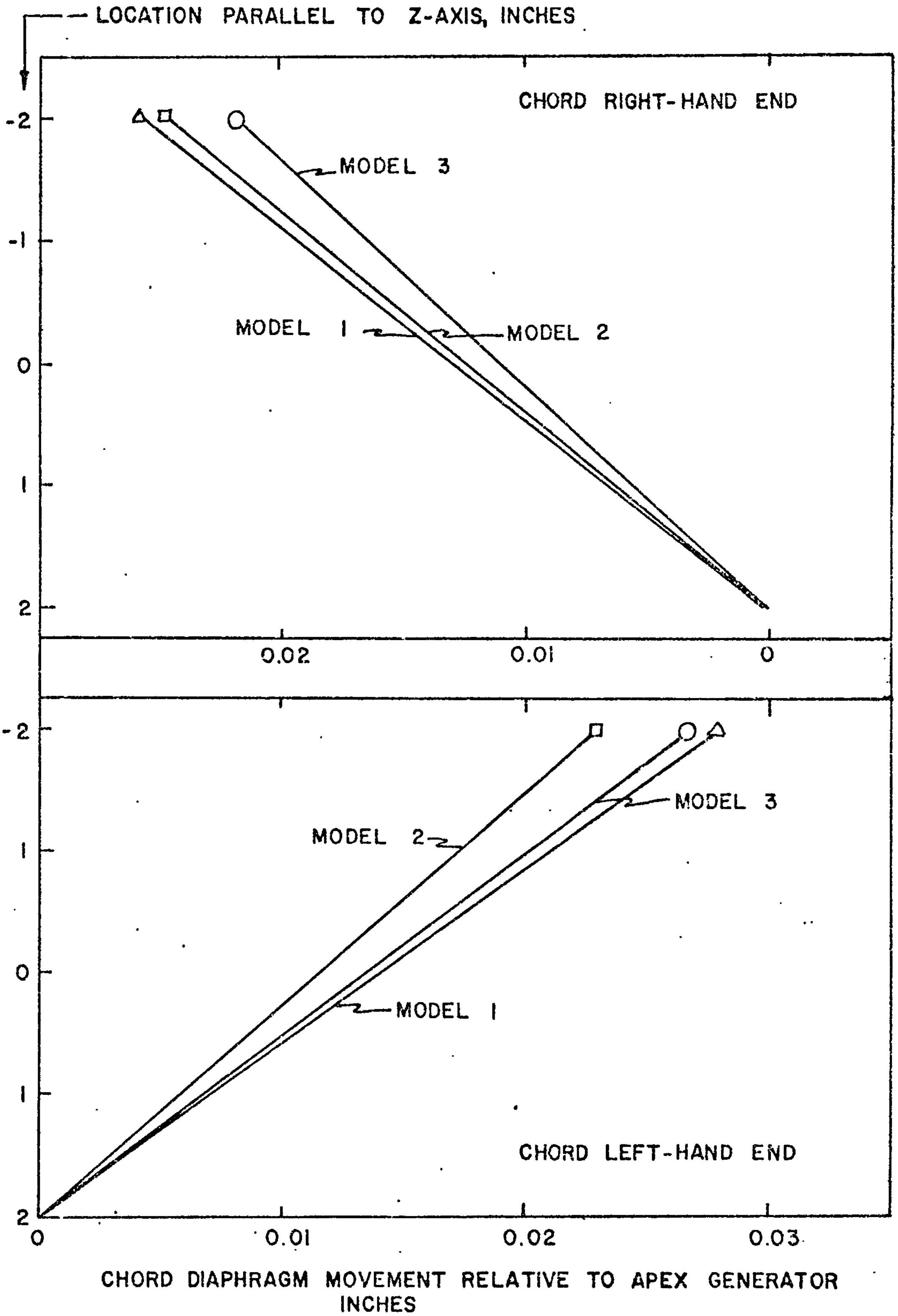

Fig. 38 - Chord-end diaphragm angular displacements resulting from stress freezing

corresponding decrease in the brace diameter at the intersection. However, this was only partially realized since the brace diameter decreased in the YZ plane only immediately above the intersection and then abruptly increased in diameter, Figure 39. Conversely, the brace diameter increased in the XZ plane immediately above the intersection and then became smaller, Figure 40. These unpredicted deformations, Figure 30, are the result of localized bending of the chord wall near the intersection as previously discussed. The influence of this bending dissipates quickly, i.e., within 1/4 of brace diameter, Figures 39 and 40. Figures 39 and 40 show that (1) the maximum brace diameter change occurs at a distance of about 1.5 times the brace diameter above the intersection curve, and (2) the magnitude of the brace cross section deformation is proportional to the τ-ratio.

The shape of the brace cross section is affected by the presence of the rigid aluminum brace end-diaphragm which forces the brace to return to the original circular shape at eight inches (four brace diameters) from the intersection, Figures 39 and 40.

Brace axial deformation. As anticipated, the brace elongates uniformly under load since all models were provided with almost identical brace components, Appendix B. The elongation averaged about 0.013 inch for each model. Elongation of the brace is independent of the τ-ratio, as would be expected, Appendix B.

Comparison of Photoelastic Model and Steel Model Deformations

Dimensional analysis correlating deformation with mechanical and geometric properties (Murphy 1950) indicates model distortions

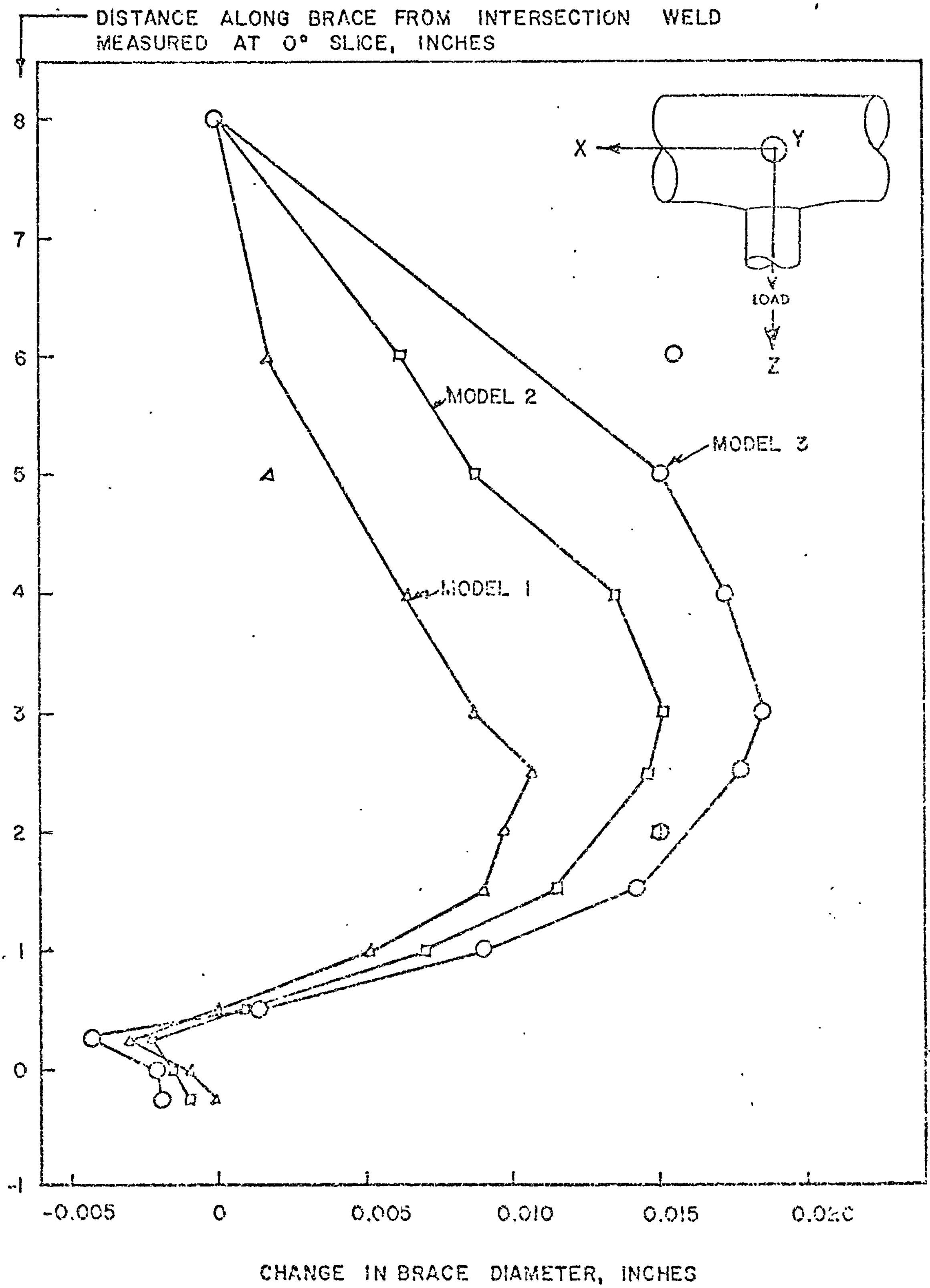

Fig. 39 - Brace profile in YZ plane resulting from stress freezing

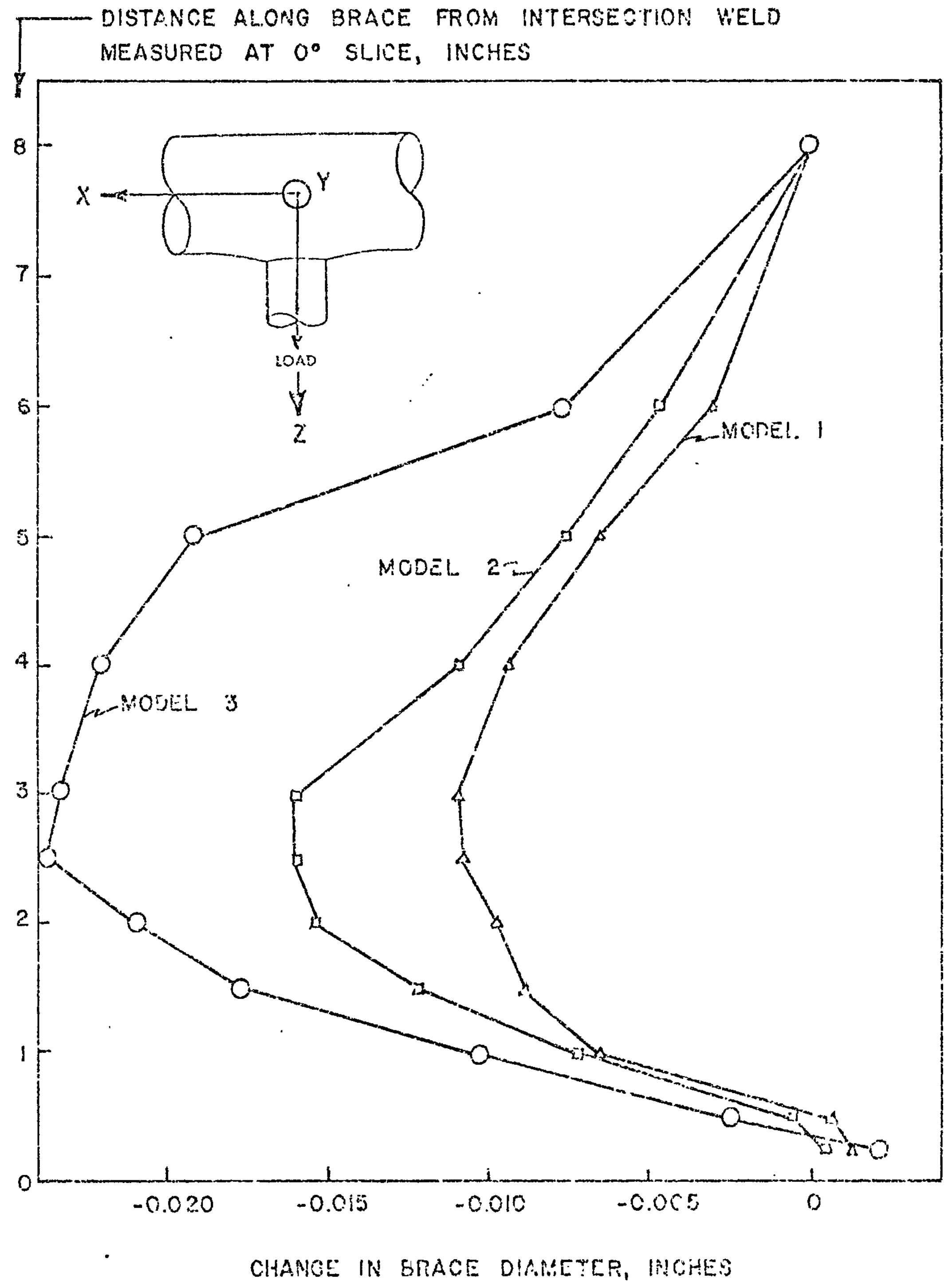

Fig. 40 - Brace profile in XZ plane resulting from stress freezing

will exist if the following ratios, equation (7-1), are not satisfied, or distortion factors are not determined.

$$\frac{\delta}{L} = f\left[\frac{\ell}{L}, \frac{P}{EL^2}, \frac{\sigma_y}{E}, \frac{\sigma_y}{\tau_y}, \frac{G}{E}\right] \qquad (7\text{-}1)$$

where

δ = displacement

ℓ = any length dimension

L = chord length

P = load

E = elastic modulus

σ_y = tensile yield strength

τ_y = shear yield strength

G = shear modulus.

Noel (1965) and Toprac (1966a) reported chord radial displacements as part of an investigation of T-connection models fabricated from steel pipe. None of the steel models possessed dimensionless ratio, α, β, γ, or τ, similar to the photoelastic models. Thus, distortion factors must be determined, but this requires either (1) experimental data, or (2) theoretical analysis (Murphy 1950). Since it is desired to correlate experimentally determined displacements, the same experimental data cannot be used for establishing the distortion factors. Further, no adequate or even acceptable theoretical analysis of tubular connections is available, thus, no method is available to qualitatively correlate the chord radial displacements. However, to provide a qualitative relationship, Model 5 (Noel 1965) was compared with photoelastic Model 3. It is evident, Table 9, that distortion exists since the α, β, γ, and τ-ratios are different for the two models.

Table 9

Comparison of Model Geometry

Ratio	Photoelastic Model 3	Steel Model 5 (Noel 1965)
α	4.91	2.78
β	0.50	0.645
γ	24.4	17.25
τ	0.61	0.75

Qualitatively, the chord cross section shapes are similar, i.e., the chord becomes oval when tensile loads are applied. In both the steel and photoelastic models, the long axis of the oval is parallel with the brace axis, Table 10.

Table 10

Comparison of Radial Displacements for
Steel Model 5 (Noel 1965) and Photoelastic Model 3

Location	Radial Displacement	
	Steel Model 5 (load-31,600 lbs) inches	Photoelastic Model (load-2.6 lbs) inches
Back generator	0.005	0.0325
Apex generator	0.030	0.141
Side generator	-0.050	-0.0955

The back generator displacements for both models are in the same direction, i.e., move opposite to the direction of load application, Figure 34. Also, the back generator movement represents the smallest deformation reported. This is verified also by the low magnitude of stress in this portion of the chord, Figure I-5, 10 and 15. The apex generator displacements for the two models are also in identical directions, i.e., in the direction of the load application. However, the apex generator displacement of the photoelastic model is the largest deformation reported whereas the apex generator displacement is not the largest deformation reported by Noel' (1965) for the steel model, Table 10. The side generator displacement is the largest reported.

The displacement of the side generators for the models is inward, Figures 30 and 32. Movement of the side generator represents the largest recorded displacement for the steel model. This is decidedly different than the measured displacements for the photoelastic model. It is believed that the difference in the location of the maximum chord radial displacements between the steel and photoelastic models is due to the difference in chord end constraints. The photoelastic model was loaded without appreciable end moments being imposed, Figure 10. The steel model was restrained by end diaphragm fixtures which imposed end-moments (Noel 1965). This prevents movement of the end diaphragms which lessens the change in length of the back of apex generators.

STRESS DISTRIBUTIONS

Inner and outer surface stresses for the photoelastic T-connection models are reported as stress concentration factors, K_t and K_0, Appendix I, which are based on the principal stress and the nominal brace stress, P/A, equation (6-2). Stress concentration factors are used because (1) of wide acceptance in industry (Carter 1969) and (2) they facilitate comparison of stress values with other true models, assuming the difference in Poisson ratios is neglected (Mershon 1966).

Chord Stress Concentration Factors

The highest stress in the photoelastic T-connection models occurs on the outside surface of the chord at the toe of the intersection weld of the 90° slice, Figure 2a point A, and in the circumferential direction, Figure I-5, 10 and 15. The magnitude of the maximum stress in the chord around the intersection increases as the chord wall thickness decreases, Figure 41, i.e., as the τ-ratio or γ-ratio increase, and ranges from 5.76 to 13.28 for (1) τ-ratios ranging from 0.354 to 0.610 and (2) the T-connection geometries shown in Table 1. Localized bending of the chord in the proximity of the intersection causes this high stress concentration. This is best observed by noting that the brace wall displaces at and immediately above the intersection weld, Figures 39 and 40, and because of continuity between the brace and chord at the intersection, the brace follows the movement of the chord wall. This means that the chord bends locally since the chord wall stresses dissipate quickly away from the intersection, Figures I-5, 10, and 15. The bending can be perceived in the chord wall of Model 3, Figure 29c. The occurrence of local chord bending is further substantiated by observing that a high compressive stress develops on the inside of the chord wall opposite the intersection of the 90° slices, Figures I-5, 10, and 15.

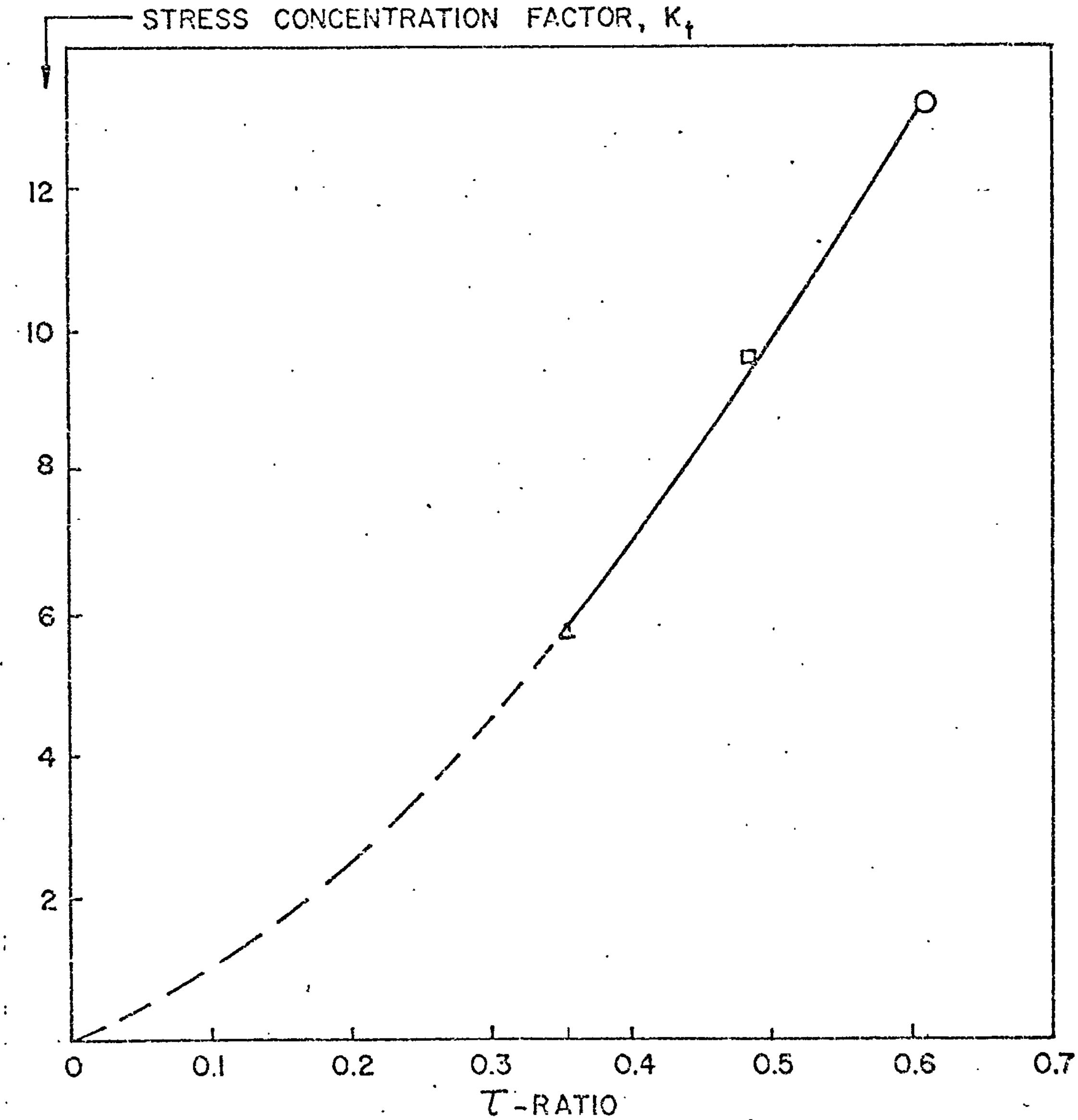

Fig. 41 - Variation of tangential stress concentration factors on the chord outside surface of the 90° slice of the photoelastic T-connection models; α = 4.91, β = 0.05, and 13.62 < γ < 24.40

The presence of the maximum chord outer surface stress at the toe of the intersection weld of the 90° slice was reported by Noel (1965) and Toprac (1966c) as the result of an experimental investigation of steel models. Unfortunately, no direct comparison between photoelastic model stresses and steel model stresses can be made because none of the photoelastic models represent true models of the Noel (1965) T-connections. However, in general, Noel's (1965) results show the same trend as obtained from the photoelastic analysis, namely, the peak stress increases as the chord wall becomes thinner, Figure 41.

Four steel models were investigated by Toprac (1966c). The dimensionless ratios, α, β, γ, and τ, for these models approximate ratios for photoelastic Model 3, Table 11. Thus, an approximate correlation was undertaken. It must be emphasized that because of the lack of true similitude between the models, no firm conclusions can be drawn from the comparison.

Based on straight line interpolation of the Toprac (1966c) data, the maximum stress concentration factor for the 90° slice is 14.2 This compares with 13.28 for photoelastic Model 3, Figures 41 and I-15. This difference in the concentration factors can be accounted for by the difference in geometry, Table 11. The stress concentration factor for the steel model should be higher than for the photoelastic model because as the α, γ, and τ-ratios increase, the stress concentration increases (Noel 1965). The magnitude of these combined effects is unknown; however, the steel model stress concentration factor should be higher than the photoelastic model factor.

Table 11

Comparison of Model Geometry

Ratio	Toprac 1	(1966c) 2	Steel 3	Model 4	Photoelastic Model 3
α	7.55	7.55	7.55	7.55	4.91
β	0.186	0.315	0.840	1.00	0.50
γ	25.5	25.5	25.5	25.5	24.4
τ	0.87	0.91	1.00	1.00	0.61

The maximum chord outer surface stress for the 180° slice is an axial stress, i.e., parallel to the X-axis and occurs immediately outboard of the weld toe, Figures I-1, 6, and 11. Again, the stress pattern is directly associated with the local bending of the chord wall near the intersection. This is indicated by the displacement of the brace, Figure 39. The associated chord bending tends to decrease the chord stress at the intersection.

The magnitude of the maximum stress on the outside surface of the 180° slice, apex generator, increases as the chord wall becomes thinner, and ranges from 3.92 to 4.54 for (1) τ-ratios ranging from 0.354 to 6.10 and (2) the T-connection geometry shown in Table 1, Figure 42. These values are low by a factor of about two in comparison with those reported by Noel (1965) and Toprac (1966c). However, the α-ratios for the steel models are about twice as large as for the photoelastic models. Graff (1970) and Toprac (1966c) indicate that the chord length has a major effect on the stress around the intersection. Toprac (1966c) shows that at a β-ratio of 0.5, doubling the chord length will about double the axial stress in the chord. τ and γ-ratio changes

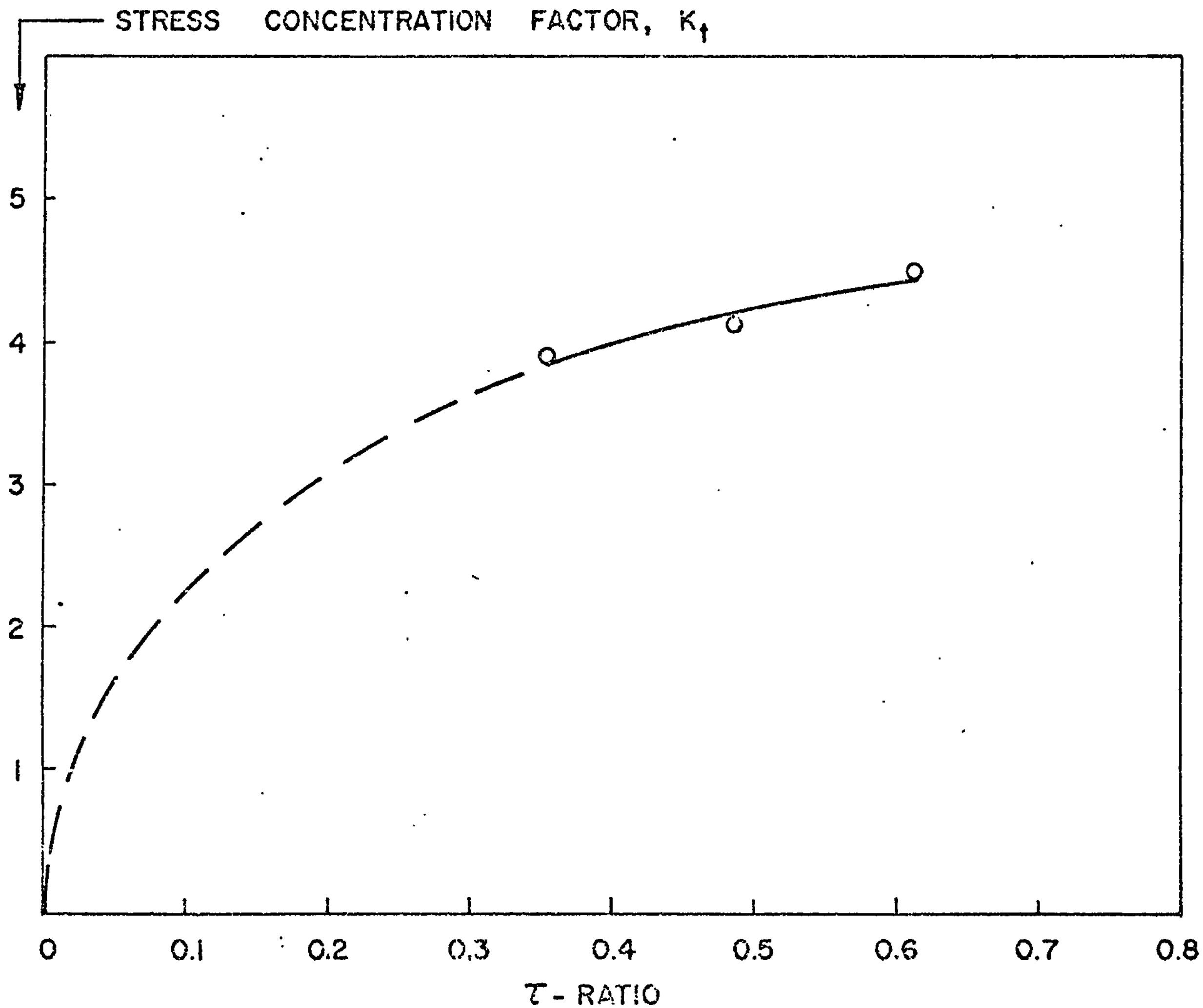

Fig. 42 - Variation of tangential stress concentration factors on the chord outside surface of 180° slice of photoelastic T-connection models, $\alpha = 4.91$, $\beta = 0.5$, and $13.62 < \gamma < 24.40$

appear to have only minor effects on the axial stresses (Toprac 1966c). Thus, the photoelastically determined concentration factors for the 180° slice appear reasonable.

The stress distributions in the 180° slices, back generators, are uniform and of low magnitude, Figures I-2, 7, and 12. No unusual information results from this analysis. The maximum stresses are associated with the thin wall model (Model 3) because of the chord wall bending, Figure 34.

Brace Stress Concentration Factors

Brace stress concentration factors in the tangential direction, Figure 28, were determined for all five slices. The orthogonal stresses were determined only for Model 1. The other two models were not analyzed for orthogonal stress since it appeared that they would not be critical.

The distribution of intersection tangential stresses on the outside surface of the brace indicates a monotonic increase as the brace angle ψ, Figure 21, increases from 0 to 90°, Figure 43. In addition, a substantial stress variation exists through the brace wall, Appendix I.

Assuming a linear distribution of stress through the brace wall permits a comparison of the areas under the stress distribution curves, Figure 44. This area is proportional to the total brace load. Agreement is very good between Models 1 and 2, the difference being two percent. The total load for Model 3 as determined from Figure 44 is about seven percent too low, indicating that the stress concentration factors are too small. A study of Figure 44 suggests that the stress concentration factors at the 30° and 60° (120° and 150°) slices are most likely in error.

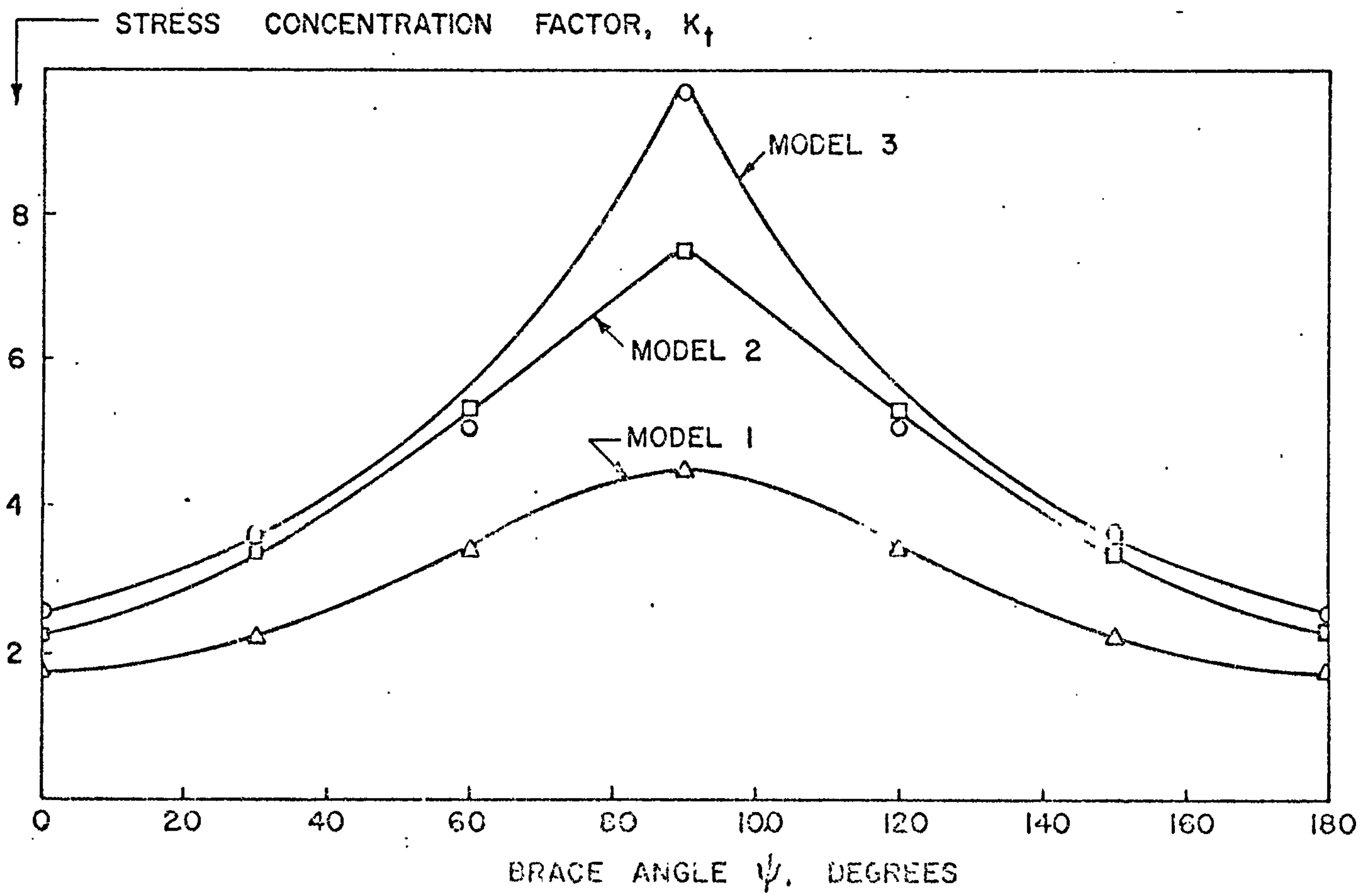

Fig. 43 - Distribution of brace outside surface tangential stress concentration factors along the intersection weld

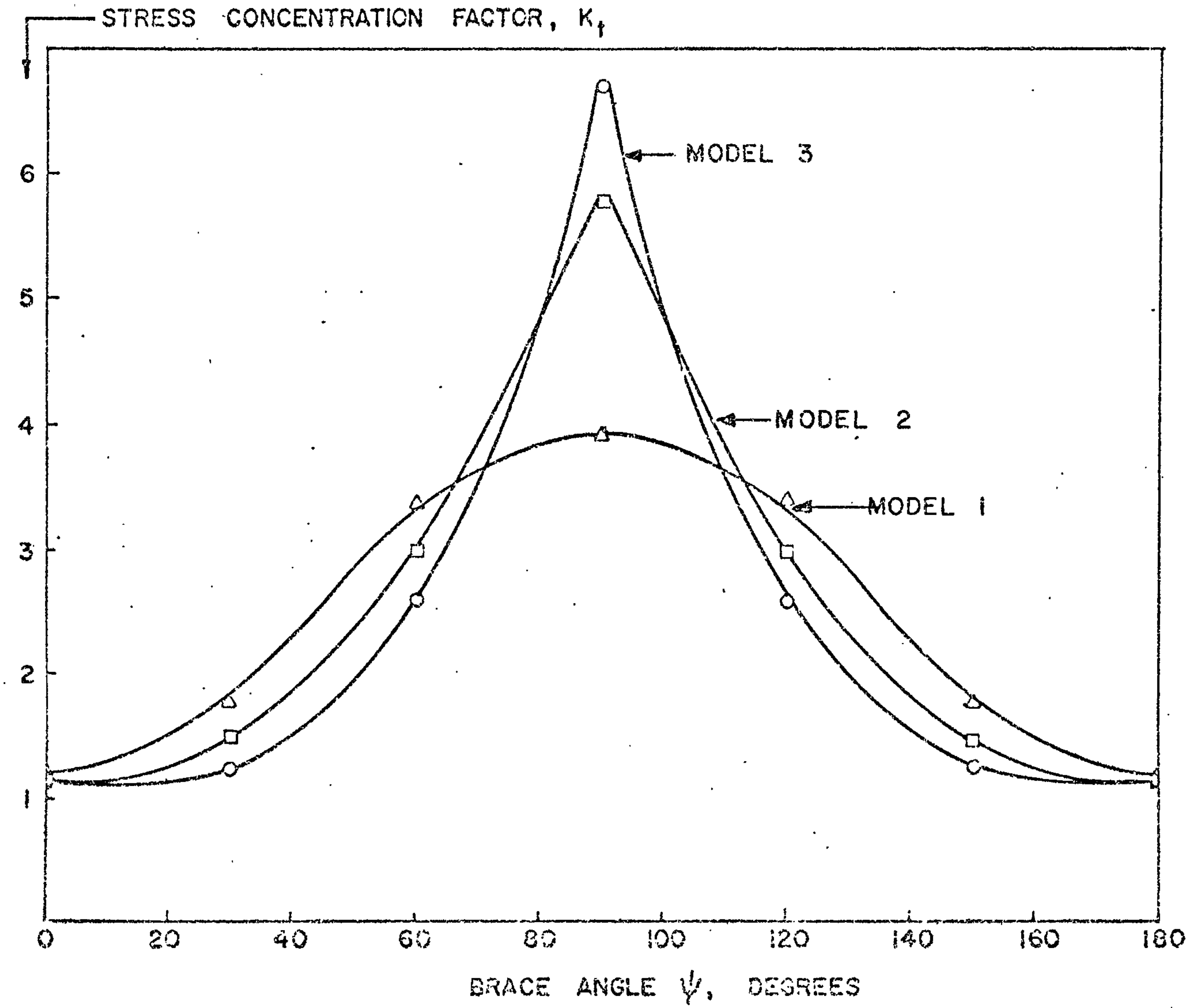

Fig. 44 - Distribution of average brace tangential stress concentration factors along the intersection weld

A re-analysis of the slices did not improve the stress values because of the difficulty of discerning the stresses on the inside surface immediately adjacent to the weld due to the "hillside" weld between the brace and chord at these locations. Nevertheless, the resulting accuracy is reasonably close to the five percent suggested by Leven (1966).

Weld Stresses

The stress distributions shown in Appendix I exclude stresses within the weld because there was insufficient data to demonstrate that the stress fringes would be visible with the butt weld. In some slices, the transparent gluing technique, Appendix F, provides easily observable fringe patterns within the weld when the slice is full thickness, Figure 45. Patterns in other slices could be made clear by milling the slice thin, Figure 46, thus eliminating the tunnel effect caused by a small tunnel-like weld. To fully utilize this technique, a calibration bar should be made from "weld" cement and the material fringe value determined.

Effect of Variation of Stress through the Connection Walls

Localized bending of the chord results in large variations of stress through the chord and brace walls, Figure 29. The presence of large stress variation through the wall casts severe doubt on the accuracy of stress values at or near the intersection when predicted by membrane theory such as done by Dundrova (1965). In addition, any shell theory which incorporates bending must be carefully selected so as to be capable of accommodating rapid changes in wall thickness stress variations.

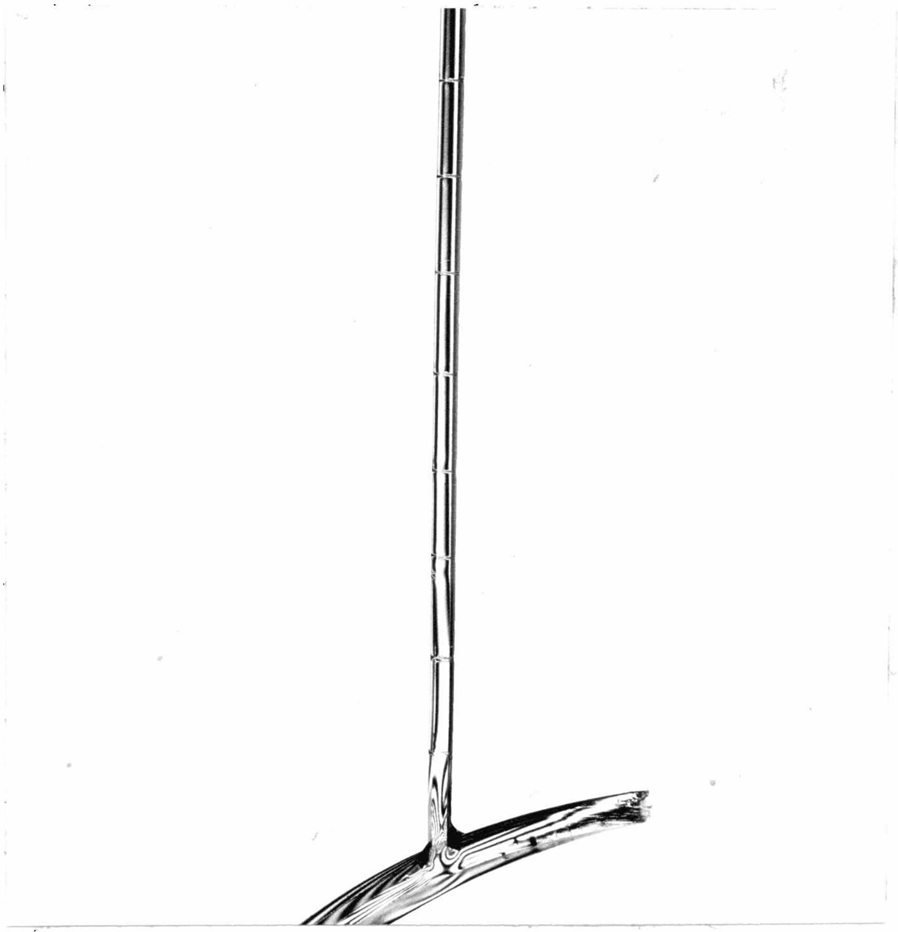

Fig. 45 - Stress fringe pattern in intersection weld of 120° slice of T-connection Model 1. Slice thickness is 0.250 inch

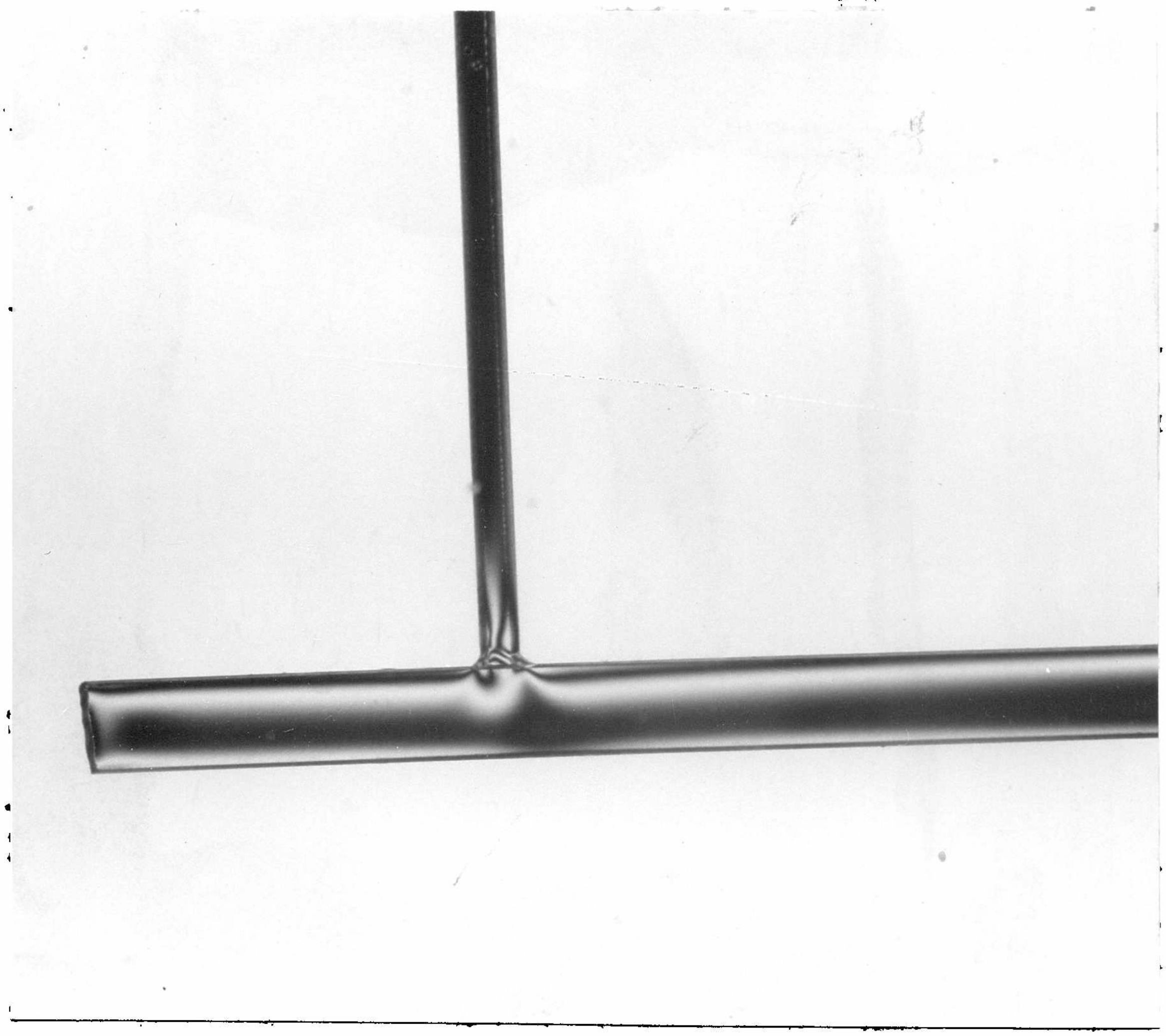

Fig. 46 - Stress fringe pattern in intersection weld of 180° slice of T-connection Model 1. Slice thickness is 0.136 inch

Design Considerations

This photoelastic study has demonstrated the capabilities of the technique to provide a visual portrayal of stresses within a tubular connection. The analysis of the fringes indicate the presence of high stresses in the chord along the intersection weld. Localized bending causes the high stress but the bending dissipates quickly away from the weld, and, in fact, the majority of the chord wall is lightly stressed, Figures I-5, 10, and 15. Thus, if economically attractive, consideration should be given to forming the T-connection chord can, i.e., chord section in the immediate vicinity of the tubular connection, from plates having two thicknesses, the thicker plate extending from $\varphi = -90°$ to $+90°$ across the positive Z-axis and the thinner plate extending from $\varphi = +90°$ to $-90°$ across the negative Z-axis. This design would decrease the weight of steel used without proportionally decreasing the connection strength.

The above suggestion does not encompass the saddle or ring reinforcement type of chord thickening, Figure 2g and h, since the resulting chord is layered and thus has almost no improvement in resistance to radial bending.

Chapter 8

CONCLUSIONS

1. Three-dimensional photoelasticity has been demonstrated to provide detailed stress distributions of tubular structural T-connections even in areas of high stress concentration.

2. Maximum stress in the chord occurs at or very near the intersection weld for all locations around the brace.

3. The maximum chord stress in the T-connection models investigated occurs at the intersection weld of the transverse slice, $\varphi = 90°$.

4. The high stress at the intersection weld is caused by local bending of the chord wall.

5. The chord does not act as a beam in bending because the neutral axis shifts and the chord cross section deforms.

6. The stress decreases rapidly away from the intersection weld along both the chord and brace.

7. The stress varies rapidly through the brace and chord walls thus imposing severe restrictions on the type of shell theory which can be used satisfactorily in analytic solutions.

8. During loading, the chord becomes ovalled with the long axis parallel to the tensile load axis.

9. The brace also becomes ovalled under load. The direction of the short axis is parallel to the chord generator when the brace is loaded in tension.

10. Economics permitting, the chord section containing the intersection can be fabricated from two plates having two thicknesses and two longitudinal welds. The thicker plate should contain the positive Z-axis of the T-connection.

11. Saddle-type reinforcements are not satisfactory for increasing the thickness of chord walls.

REFERENCES

Anderson, G. W., 1961, "Circumferential Stresses in a Joint Between Structural Tubes", Special Report No. 22, Commonwealth Experimental Building Station, Dept. of Works, Sydney, Australia, May.

Andrain, L. E., Sewell, K. A., and Womack, W. R., 1958, "Partial Investigation of Directly Loaded Pipe T-Joints," Unpublished Bachelor's Thesis in Civil Engineering, Southern Methodist Univ., Dallas, Texas.

API, 1969, "Specification for Fabricated Structual Steel Pipe", Standard 5B, First Edition, American Petroleum Institute, Div. of Production, Dallas, Texas.

Beale, L. A. and Toprac, A. A., 1967, "Analysis of In-Plane T, Y, and K Welded Tubular Connections", SFRL Tech. Report P550-9, Univ. of Texas, Austin, Texas, April.

Bergeman, M. L., 1947,"Manufacturing Processes", Second Edition, John Wiley and Sons, Inc., New York.

Bijlaard, P. P., 1955, "Stresses from Local Loadings in Cylindrical Pressure Vessels", Trans. Am. Soc. of Mech. Engrs., pp. 805-816.

______, 1955, "Stresses from Radial Loads and External Moments in Cylindrical Pressure Vessels", The Welding Journal, Vol. 34, No. Research Supplement, pp. 608-s to 617-s.

______, 1959, "Additional Data on Stresses in Cylindrical Shells Under Local Loading", Welding Research Council Bulletin, No. 50, pp. 10-50, May.

Bouwkamp, J. G., 1965, "Behavior of Tubular Truss Joints Under Static Loads", SESM Report No. 65-4, Dept. of Civil Engineering, Univ. of California, Berkeley, Calif., Figure 1, July.

______, 1966, "Tubular Joints Under Static and Alternating Loads", SEL Report 66-15, Dept. of Civil Engr., Univ. of California, Berkeley, California, June.

Bouwkamp, J. G., 1966, "Recent Trends in Research on Tubular Connections", Petr. Trans., SPE Journal of Petr. Tech., pp. 1491-1499, November.

______ and Stephen, R. M., 1967, "Tubular Joints Under Alternating Loads", SEL Report No. 67-29, Univ. of California, Berkeley, California, November.

Bouwkamp and Stephen, R. M., 1968, "Cement-Grout Filled Tubular Joints Under Alternating Loads", SEL Report 68-16, Dept. of Civil Engr., Univ. of California, Berkeley, California, November.

Bryant, J. E., 1962, "Circular Tubular Joint Design", Unpublished Master's Thesis, Tulane Univ., New Orleans, Louisiana.

Carter, R. M., Marshall, P. W., Thomas, P. D., and Swanson, T. M., 1969, "Materials Problems in Offshore Platforms", Paper No. OTC 1043, Offshore Technology, Vol. 1, pp. 443-470.

Cleveland Twist Drill Co., 1964, "The Use and Care of Twist Drills", Cleveland, Ohio.

Dalley, J. W. and Riley, W. F., 1965, "Experimental Stress Analysis", McGraw-Hill Book Co., Inc., New York.

D'Agostino, J., Drucker, D. C., Liu, C. K. and Mylonas, C., 1955, "Epoxy Adhesives and Casting Resins as Photoelastic Plastics", Proceedings of Soc. of Stress Analysis, Vol. 12, No. 2, pp. 123-128.

Donnell, L. H., 1933, "Stability of Thin-Walled Tubes Under Torsion", NACA Report No. 479.

Drucker, D. C., 1950, "Handbook of Experimental Stress Analysis", Ed. by M. Hetenyi, Chapter 17, Photoelasticity II, Three-Dimensional Photoelasticity, John Wiley and Sons, New York, pp. 924-976.

Dundrova, V. and Toprac, A. A., 1965, "Stresses at Intersection of Tubes - Cross and T-Joints", SFRL Tech. Report P550-5, Univ. of Texas, Austin, Texas.

Frocht, M. M., 1941 and 1948, "Photoelasticity", Vol. I and II, John Wiley and Sons, New York.

______ and Pih, H., 1954, "A New Cementable Material for Two- and Three-Dimensional Photoelastic Research", Proceedings of Soc. of Experimental Stress Analysis, Vol. 12, No. 1, pp. 55-64.

Flügge, W., 1962, "Stresses in Shells", Springer-Verlag, Berlin, Germany.

Galle, E. M., 1959, "Photoelastic Analysis of The Stresses Near the Bottom of a Cylindrical Cavity due to Non-Symmetric Loading", Unpublished Masters Thesis, Rice University, Houston, April.

Godden, W. G. and Griffith, A. R., 1969, "Model Analysis of the A. D. Edmonston Pumping Plant Discharge Line Manifolds", Report 69-25, Structural Engineering Laboratory, Univ. of Cal., Berkeley, Cal., September.

Godfrey, G. B., 1958, "The Application of Tubes to Structures", Acier-Stahl-Steel, Vol. 23, No. 12, December.

Godfrey, G. B., 1959, "Joints in Tubular Structures", Structual Engineer, Vol. 37, No. 4, pp. 126-135, April.

Graff, W. J., 1970, "Design Correlations of Elastic Behavior and Static Strength of Zero Eccentricity T, Y, and K Tubular Joints", Second Offshore Technology Conference, April 22-24, Houston.

Greste, O. and Clough, R. W., 1967, "Finite Element Analysis of Tubular Joints; A Report on a Feasibility Study", SEL Report No. 67-7, Dept. of Civil Engr., Univ. of California, Berkeley, California, April.

Hebert, A. and Vafai, A., 1969, "Experimental Investigation of a Tubular K-Joint", Unpublished Thesis, Dept. of Civil Engr., Univ. of Houston, Houston, Texas, Spring.

Hetenyi, M., 1938, "The Fundamentals of Three-Dimensional Photoelasticity", Journal of Applied Mech., Vol. 5, No. 4, pp. 149-155.

______, 1939, "The Application of Hardening Resins in Three-Dimensional Photoelastic Studies", Journal of Applied Physics, Vol. 10, pp. 295-300.

Hettich, W., 1960, "Tubular Steel Frame Work in Church Construction", No. 7-8, Acier-Stahl-Steel, pp. 323-328, July-August.

Johnson, C. P., 1967, "A Finite Element Approximation for the Analysis of Thin Shells", Ph.D. Dissertation, Univ. of California, Berkeley, California.

Johnston, L. P., 1963, "The Welded Tubular Joint Problem in Offshore Structures", First Univ. of Texas Conf. on Drilling and Rock Mechanics, Univ. of Texas, Austin, Texas, January.

Lee, G. C., 1968, "Offshore Structures, Past, Present, Future, and Design Considerations", Proceedings of OECON, pp. 169-196.

Leven, M. M., 1948, "A New Material for Three-Dimensional Photoelasticity", Proceedings of Soc. of Experimental Stress Analysis, Vol. 6, No. 1, pp. 19-28.

______, 1963, "Epoxy Resins for Photoelastic Use", Proceedings of the International Symposium on Photoelasticity, Pergamon Press, New York, pp. 145-165.

______, 1966, "Photoelastic Determination of the Stresses in Reinforced Openings in Pressure Vessels", Welding Research Council Bulletin 113, pp. 25-52, April.

Mershon, J. L., 1966, "Preliminary Evaluation of PVRC Photoelastic Test Data on Reinforced Openings in Pressure Vessels", Welding Research Council Bulletin 113, pp. 53-70, April.

Murphy, G., 1950, "Similitude in Engineering", The Ronald Press, New York, pp. 17-47.

Murray, W. M., 1969, Personal Communication.

Noel, J. S., Beale, L. A. and Toprac, A. A., 1965, "An Investigation of Stresses in Welded T-Joints", SFRL Tech. Report P550-3, Univ. of Texas, Austin, Texas, March.

Pease, F. T., 1960, "Experimental Stress Analysis of a Structural Pipe T-Joint", Unpublished Master's Thesis in Civil Engr., Univ. of Houston, Houston, Texas, August.

Pickett, A. G. and Grigory, S. C., 1967, "Prediction of Low Cycle Fatigue Life of Pressure Vessels", Paper 67-Met-3, Am. Soc. of Mech. Engrs. Meeting, April 3-5, Houston, Texas.

Scordelis, A. C. and Bouwkamp, J. G., 1968, "Analytical Study of Tubular Tee-Joints", SEL Report 68-14, Dept. of Civil Engr., Univ. of California, Berkeley, California, October.

Solakian, A. G., 1935, "A New Photoelastic Material", Mechanical Engineering, Vol. 57, pp. 767-771.

Stewart, G. B., 1959, "Large Tubular Structures", Acier-Stahl-Steel, Vol. 24, No. 11, pp. 463-468, November.

Stewarts and Lloyds, Ptg. Ltd., 1961, "Report on Behavior of Welded Joints in Tubular Structures", Technical Office, Newcastle, Australia, January.

Takahashi, S. K. and Dong, S. B., 1968, "Finite Element Analysis of Solids of Revolution", Tech. Report R-400, Naval Civil Engr. Laboratory, Port Hueneme, California, March.

_______ and Mark, R., 1968, "Photoelastic Investigation of Stress Concentrations in Sphere-Cylinder Transition Regions - Including a Comparison of Results from Photoelastic and Finite Element Analyses", Tech. Report R-572, Naval Civil Engr. Laboratory, Port Hueneme, California, April.

Taylor, C. E., Stitz, E. O., and Balsheim, R. O., 1950, "A Casting Material for Three-Dimensional Photoelasticity", Proceedings of Soc. of Experimental Stress Analysis, Vol. 7, No. 2, pp. 155-172.

______ and Lind, N. C., 1966, "Photoelastic Study of the Stresses Near Openings in Pressure Vessels, Welding Research Council Bulletin 113, pp. 1-24, April.

Tardy, M. H. L., 1929, Méthode pratique d'examen de mesure de la birefringence des verres d'optique, Rev d'Optique, vol. 8, pp. 59-69.

Thielsch, H., 1965, "Defects and Failures in Pressure Vessels and Piping", Reinhold Publishing Corp., New York, pp. 29-43.

Timoshenko, S. P., 1953, "History of Strength of Materials", McGraw-Hill Book Co., Inc., New York, pp. 156-162.

______, and Woinowsky-Krieger, S., 1959, "Theory of Plates and Shells", McGraw-Hill Book Co., Inc., New York.

Toprac, A. A., Johnston, L. P. and Noel, J., 1966, "Welded Tubular Connections: An Investigation of Stresses in T-Joints", Welding Journal Research Supplement, January.

______, and Chen, J., 1966, "Stresses in Steel Tubular Y-Joints", SFRL Tech. Report No. P550-7, Univ. of Texas, Austin, Texas, January.

______, and Brown, R. C., 1966, "An Experimental Investigation of Tubular T-Joints", SFRL Tech. Report P550-8, Univ. of Texas, Austin, Texas, January.

Toprac, A. A., 1968, "Studies of Tubular Joints in Japan; Part I, Review of Research Reports", Report No. R682, Technology Laboratories, Austin, Texas, Prepared for Welding Research Council, New York, September.

______, 1969, "Review of Research; Tubular Connection Investigations in USA: Static, Fatigue, Analysis", Prepared for Welding Research Council, New York, May.

Welter, G. and Dubuc, J., 1962, "Fatigue Resistance of Simulated Nozzles in Model Pressure Vessels of T-1 Steels, Welding Journal, Vol. 41, No. 8, Research Supplement, pp. 368-s to 374-s.

Woodward, C. M., 1881, "A History of the Saint Louis Bridge", G. I. Jones & Co.

Yuan, S. W., 1946, "Thin Cylindrical Shells Subjected to Concentrated Loads", Quarterly of Applied Mathematics, Vol. 4, No. 1, pp. 13-26.

APPENDIX A

EQUIPMENT AND MATERIALS

APPENDIX A

EQUIPMENT AND MATERIALS

Photoelastic Resins

EPON 815® and EPON 828®

Vendor: The Ring Chemical Company
Houston, Texas

Resin Curing Agent

Diethylaminopropylamine (DEP)

Vendor: The Ring Chemical Company
Houston, Texas

Mold Release

RAM Mold Release 225

Manufacturer: RAM Chemicals
Gardena, California

Epoxy Adhesive

Ring Epoxy Adhesive

Vendor: The Ring Chemical Company
Houston, Texas

Machine Tools

Monarch Geared-head Lathe, 13-inch size

Manufacturer: The Monarch Machine Tool Company
Sidney, Ohio

Van Norman Vertical Spindle Milling Machine, Model 36

Manufacturer: Van Norman Machine Tool Company
Springfield, Massachusetts

Cincinnati Numerically Controlled Acramatic No. 3 Cintimatic-200 Series Control Vertical Spindle Milling Machine

Manufacturer: The Cincinnati Milling Machine Company
Cincinnati, Ohio

Polariscope

12-inch diameter, diffused light polariscope

Manufacturer: Polarizing Instrument Company
Irvington, New York

Light Box

18-inch x 18-inch x 6-inch deep opal glass front light cabinet with 9 white and 8 green 15-watt fluorescent lamps

Vendor: Shop made

Camera

Polarizing Instrument Company view camera, 8-inch x 10-inch with 72-inch bellows

Manufacturer: Polarizing Instrument Company
Irvington, New York

Lens and Shutter

Wollensak 13-inch focal length, f 6.8, series IA RAPTAR lens with ALPHAX Synchromatic shutter

Vendor: Polarizing Instrument Company
Irvington, New York

Filter

Wratten 77 filter, 3-inch square

Manufacturer: Eastman Kodak

Rochester, New York

Photographic Film

Tri-X Ortho Sheet Film, 8-inch x 10-inch

Manufacturer: Eastman Kodak

Rochester, New York

Photographic Paper

F-5 AZO paper, 8-inch x 10-inch

Manufacturer: Eastman Kodak

Rochester, New York

Hallowax Oil

Hallowax oil No. 1007

Vendor: E. H. Sargent Company

Dallas, Texas

Paraffin Oil

Paraffin oil, 125-135 cp viscosity

Vendor: Fisher Scientific

Houston, Texas

Oven

Shop made oven

Inside dimensions: 43 inches wide x 48 inches deep x 54-3/4 inches high

Outside dimensions: 59 inches wide x 51-1/2 inches deep x 83 inches high

Temperature range: 75-300°F

Controller: Whellco with adjustable set point

Grinder

Series 6 Dumore Super Flex Grinder

Vendor: Wessendorf and Nelms
Houston, Texas

Drill Press

Series 16 Dumore Hi-Speed Drill Press

Vendor: Wessendorf and Nelms
Houston, Texas

Marking Ink

Dyken Steel Blue DX-100 Marking Ink

Vendor: Briggs-Weaver Machine Company
Houston, Texas

Surface Plate

Black Granite Surface plate, 36 inches x 72 inches

Manufacturer: DoALL Company
Des Plaines, Illinois

Height Gage

Vernier Height Gage, 24 inches

Manufacturer: DoALL Company
Des Plaines, Illinois

APPENDIX B

DIMENSIONS OF T-CONNECTION PHOTOELASTIC MODELS

APPENDIX B

DIMENSIONS OF T-CONNECTION PHOTOELASTIC MODELS

Each model was carefully measured before and after stress freezing. Chord diameters were measured every 1/2 to 1 inch with a micrometer caliper, Figure B-1. Brace diameters were measured every 1/4 to 1 inch. The measurements and the changes resulting from stress freezing are given in Tables B-1 to B-3 for photoelastic Models 1 to 3, respectively.

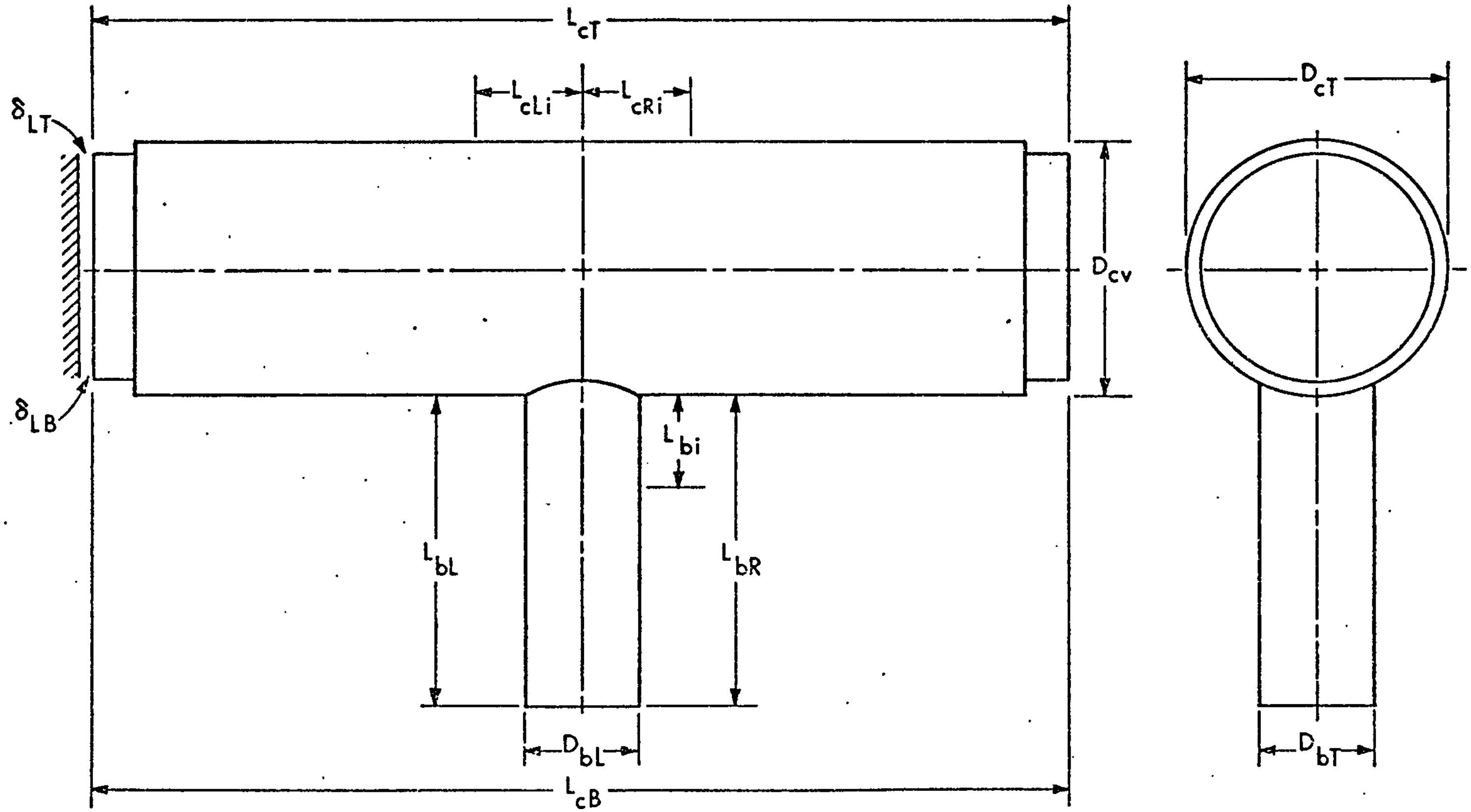

Fig. B-1 - Dimension location map of T-connection models

Table B-1

Dimensions of T-Connection Model 1

A. Chord Diameter

Designation	Distance in	Before Stress Freezing D_{cV} in	Before Stress Freezing D_{cT} in	After Stress Freezing D_{cV} in	After Stress Freezing D_{cT} in	Change ΔD_{cV} in	Change ΔD_{cT} in
L_{cL0}	0	-	4.0050	-	3.9539	-	-0.0511
L_{cL1}	½	-	4.0040	-	3.9572	-	-0.0468
L_{cL2}	1	4.0040	4.0038	4.0639	3.9580	0.0599	-0.0458
L_{cL3}	1½	4.0031	4.0038	4.0612	3.9619	0.0581	-0.0419
L_{cL4}	2	4.0031	4.0039	4.0576	3.9648	0.0545	-0.0391
L_{cL5}	2½	4.0031	4.0035	4.0525	3.9701	0.0494	-0.0334
L_{cL6}	3	4.0037	4.0034	4.0485	3.9739	0.0448	-0.0295
L_{cL7}	4	4.0037	4.0040	4.0390	3.9822	0.0353	-0.0218
L_{cL8}	5	4.0036	4.0041	4.0316	3.9905	0.0280	-0.0136
L_{cL9}	6	4.0036	4.0043	4.0237	3.9972	0.0201	-0.0071
L_{cL10}	7	4.0036	4.0044	4.0181	4.0036	0.0145	-0.0008
L_{cL11}	8	4.0035	4.0040	4.0126	4.0045	0.0091	-0.0005
L_{cR1}	½	-	4.0040	-	3.9549	-	-0.0491
L_{cR2}	1	4.0036	4.0040	4.0630	3.9571	0.0594	-0.0469
L_{cR3}	1½	4.0030	4.0040	4.0605	3.9590	0.0575	-0.0450
L_{cR4}	2	4.0026	4.0040	4.0570	3.9622	0.0544	-0.0418
L_{cR5}	2½	4.0030	4.0040	4.0527	3.9676	0.0497	-0.0364
L_{cR6}	3	4.0030	4.0030	4.0472	3.9710	0.0442	-0.0320
L_{cR7}	4	4.0030	4.0032	4.0403	3.9808	0.0373	-0.0224
L_{cR8}	5	4.0028	4.0030	4.0307	3.9871	0.0279	-0.0159
L_{cR9}	6	4.0028	4.0026	4.0236	3.9948	0.0208	-0.0078
L_{cR10}	7	4.0027	4.0026	4.0186	4.0008	0.0159	-0.0018
L_{cR11}	8	4.0030	4.0032	4.0130	4.0033	0.0100	0.0001

Table B-1 (Cont'd.)

Dimension of T-Connection Model 1 (Cont'd.)

B. Chord Length

Before Stress Freezing		After Stress Freezing		Change	
L_{cT} in	L_{cB} in	L_{cT} in	L_{cB} in	ΔL_{cT} in	ΔL_{cB} in
19.654	19.655	19.6330	19.6808	-0.0210	0.0258

C. Chord End Angular Displacement[a]

Before Stress Freezing				After Stress Freezing				Change			
δ_{RT} in	δ_{RB} in	δ_{LT} in	δ_{LB} in	δ_{RT} in	δ_{RB} in	δ_{LT} in	δ_{LB} in	$\Delta\delta_{RT}$ in	$\Delta\delta_{RB}$ in	$\Delta\delta_{LT}$ in	$\Delta\delta_{LB}$ in
0.003	0.000	0.000	0.004	0.029	0.00	0.024	0.00	0.026	0.0	0.024	-0.004

[a] Positive values measured from the vertical toward the center of the connection

D. Brace Diameter

Designation	Distance in	Before Stress Freezing D_{bL} in	Before Stress Freezing D_{bT} in	After Stress Freezing D_{bL} in	After Stress Freezing D_{bT} in	Change ΔD_{bL} in	Change Δ_{bT} in
L_{b-1}	$-\frac{1}{4}$	-	2.0098	-	2.0097	-	-0.0001
L_{b0}	0	-	2.0099	-	2.0090		-0.0009
L_{b1}	$\frac{1}{4}$	2.0075	2.0091	2.0062	2.0090	-0.0013	0.0
L_{b2}	$\frac{1}{2}$	2.0078	2.0090	2.0071	2.0121	-0.0007	0.0030
L_{b3}	1	2.0085	2.0090	2.0019	2.0142	-0.0066	0.0052
L_{b4}	$1\frac{1}{2}$	2.0086	2.0081	1.9997	2.0172	-0.0089	0.0091
L_{b5}	2	2.0084	2.0084	1.9986	2.0172	-0.0098	0.0088
L_{b6}	$2\frac{1}{2}$	2.0089	2.0080	1.9981	2.0188	-0.0108	0.0108
L_{b7}	3	2.0085	2.0085	1.9976	2.0173	-0.0109	0.0088
L_{b8}	4	2.0083	2.0083	1.9990	2.0148	-0.0093	0.0065
L_{b9}	5	2.0090	2.0090	2.0025	2.0108	-0.0065	0.0018
L_{b10}	6	2.0088	2.0070	2.0058	2.0088	-0.0030	0.0018

Table B-1 (Cont'd.)

Dimension of T-Connection Model 1 (Cont'd.)

E. Brace Length

Before Stress Freezing L_{bR} in	Before Stress Freezing L_{bL} in	After Stress Freezing L_{bR} in	After Stress Freezing L_{bL} in	Change ΔL_{bR} in	Change ΔL_{bL} in
8.011	8.004	8.026	8.017	0.015	0.013

F. Brace End Angular Displacement[a]

Before Stress Freezing δ_N in	Before Stress Freezing δ_F in	After Stress Freezing δ_N in	After Stress Freezing δ_F in	Change $\Delta\delta_N$ in	Change $\Delta\delta_F$ in
0	0.010	0.0	0.010	0.0	0.0

[a] Positive values measured from the vertical toward the center of the connection.

Table B-2

Dimension of T-Connection Model 2

A. Chord Diameter

Designation	Distance in	Before Stress Freezing D_{cV} in	Before Stress Freezing D_{cT} in	After Stress Freezing D_{cV} in	After Stress Freezing D_{cT} in	Change ΔD_{cV} in	Change ΔD_{cT} in
L_{cL0}	0	-	4.0093	-	3.9162	-	-.0931
L_{cL1}	½	-	4.0090	-	3.9165	-	-.0925
L_{cL2}	1	4.0099	4.0091	4.1017	3.9216	.0918	-.0875
L_{cL3}	1½	4.0101	4.0090	4.0980	3.9270	.0879	-.0820
L_{cL4}	2	4.0098	4.0091	4.0932	3.9332	.0834	-.0759
L_{cL5}	2½	4.0099	4.0089	4.0895	3.9395	.0796	-.0694
L_{cL6}	3	4.0098	4.0087	4.0811	3.9455	.0713	-.0632
L_{cL7}	4	4.0095	4.0088	4.0668	3.9598	.0573	-.0490
L_{cL8}	5	4.0080	4.0087	4.0550	3.9735	.0470	-.0352
L_{cL9}	6	4.0080	4.0079	4.0400	3.9869	.0320	-.0210
L_{cL10}	7	4.0070	4.0079	4.0310	3.9963	.0240	-.0116
L_{cL11}	8	4.0070	4.0079	4.0171	4.0038	.0101	-.0041
L_{cR1}	½	-	4.0099	-	3.9168	-	-.0931
L_{cR2}	1	4.0105	4.0099	4.1010	3.9205	.0905	-.0894
L_{cR3}	1½	4.0105	4.0103	4.0990	3.9245	.0885	-.0858
L_{cR4}	2	4.0105	4.0110	4.0922	3.9340	.0817	-.0770
L_{cR5}	2½	4.0106	4.0113	4.0868	3.9380	.0762	-.0733
L_{cR6}	3	4.0107	4.0110	4.0852	3.9490	.0745	-.0620
L_{cR7}	4	4.0107	4.0110	4.0681	3.9598	.0574	-.0512
L_{cR8}	5	4.0107	4.0008	4.0540	3.9727	.0433	-.0281
L_{cR9}	6	4.0103	4.0095	4.0397	3.9850	.0294	-.0245
L_{cR10}	7	4.0103	4.0090	4.0290	3.9992	.0187	-.0098
L_{cR11}	8	4.0100	4.0085	4.0184	4.0032	.0084	-.0053

Table B-2 (Cont'd.)

Dimension of T-Connection Model 2 (Cont'd.)

B. Chord Length

Before Stress Freezing		After Stress Freezing		Change	
L_{cT} in	L_{cB} in	L_{cT} in	L_{cB} in	ΔL_{cT} in	ΔL_{cB} in
19.685	19.680	19.6747	19.7138	-0.0103	0.0338

C. Chord End Angular Displacement[a]

Before Stress Freezing				After Stress Freezing				Change			
δ_{RT} in	δ_{RB} in	δ_{LT} in	δ_{LB} in	δ_{RT} in	δ_{RB} in	δ_{LT} in	δ_{LB} in	$\Delta\delta_{RT}$ in	$\Delta\delta_{RB}$ in	$\Delta\delta_{LT}$ in	$\Delta\delta_{LB}$ in
0	0.004	0	0.002	0.021	0.0	0.021	0.0	0.021	-0.004	0.021	-0.002

[a] Positive values measured from the vertical toward the center of the connection

D. Brace Diameter

Designation	Distance in	Before Stress Freezing		After Stress Freezing		Change	
		D_{bL} in	D_{bT} in	D_{bL} in	D_{bT} in	ΔD_{bL} in	Δ_{bT} in
L_{b-1}	-¼	-	2.0070	-	2.0060	-	-.0010
L_{b0}	0	-	2.0070	-	2.0054	-	-.0016
L_{b1}	¼	2.0009	2.0053	2.0005	2.0030	0.0004	-.0023
L_{b2}	½	2.0023	2.0051	2.0017	2.0060	-.0006	.0009
L_{b3}	1	2.0015	2.0060	1.9943	2.0130	-.0072	.0070
L_{b4}	1½	2.0019	2.0059	1.9897	2.0174	-.0122	.0115
L_{b5}	2	2.0019	2.0050	1.9865	2.0202	-.0154	.0152
L_{b6}	2½	2.0022	2.0048	1.9862	2.0195	-.0160	.0147
L_{b7}	3	2.0022	2.0048	1.9862	2.0200	-.0160	.0152
L_{b8}	4	2.0029	2.0052	1.9920	2.0188	-.0109	.0136
L_{b9}	5	2.0042	2.0052	1.9968	2.0140	-.0074	.0088
L_{b10}	6	2.0056	2.0050	2.0010	2.0113	-.0046	.0063

Table B-2 (Cont'd.)

Dimension of T-Connection Model 2 (Cont'd.)

E. Brace Length

Before Stress Freezing L_{bR} in	Before Stress Freezing L_{bL} in	After Stress Freezing L_{bR} in	After Stress Freezing L_{bL} in	Change ΔL_{bR} in	Change ΔL_{bL} in
8.196	8.195	8.210	8.208	0.0140	0.0130

F. Brace End Angular Displacement[a]

Before Stress Freezing δ_N in	Before Stress Freezing δ_F in	After Stress Freezing δ_N in	After Stress Freezing δ_F in	Change $\Delta\delta_N$ in	Change $\Delta\delta_F$ in
0.005	0.0	0.004	0.0	0.001	0.000

[a] Positive values measured from the vertical toward the center of the connection.

Table B-3

Dimension of T-Connection Model 3

A. Chord Diameter

Designation	Distance in	Before Stress Freezing D_{cV} in	Before Stress Freezing D_{cT} in	After Stress Freezing D_{cV} in	After Stress Freezing D_{cT} in	Change ΔD_{cV} in	Change ΔD_{cT} in
L_{cL0}	0	-	4.0020	-	3.8110	-	-0.1910
L_{cL1}	½	-	4.0024	-	3.8123	-	-0.1901
L_{cL2}	1	4.0130	4.0031	4.1772	3.8174	0.1642	-0.1857
L_{cL3}	1½	4.0130	4.0041	4.1703	3.8297	0.1573	-0.1744
L_{cL4}	2	4.0137	4.0039	4.1671	3.8430	0.1534	-0.1609
L_{cL5}	2½	4.0129	4.0040	4.1608	3.8451	0.1479	-0.1589
L_{cL6}	3	4.0121	4.0041	4.1517	3.8785	0.1396	-0.1256
L_{cL7}	4	4.0125	4.0041	4.1297	3.8930	0.1172	-0.1111
L_{cL8}	5	4.0121	4.0047	4.1036	3.9233	0.0915	-0.0814
L_{cL9}	6	4.0113	4.0045	4.0757	3.9480	0.0644	-0.0565
L_{cL10}	7	4.0101	4.0041	4.0490	3.9710	0.0389	-0.0331
L_{cL11}	8	4.0075	4.0030	4.0260	3.9859	0.0185	-0.0171
L_{cR1}	½	-	4.0023	-	3.8179	-	-0.1844
L_{cR2}	1	4.0117	4.0021	4.1792	3.8175	0.1675	-0.1846
L_{cR3}	1½	4.0129	4.0015	4.1736	3.8250	0.1607	-0.1765
L_{cR4}	2	4.0110	4.0020	4.1687	3.8409	0.1577	-0.1611
L_{cR5}	2½	4.0116	4.0016	4.1605	3.8521	0.1489	-0.1495
L_{cR6}	3	4.0098	4.0008	4.1501	3.8830	0.1403	-0.1178
L_{cR7}	4	4.0090	4.0007	4.1281	3.8931	0.1191	-0.1076
L_{cR8}	5	4.0083	4.0000	4.1051	3.9180	0.0968	-0.0820
L_{cR9}	6	4.0070	3.9990	4.0792	3.9410	0.0722	-0.0580
L_{cR10}	7	4.0050	3.9990	4.0510	3.9671	0.0460	-0.0319
L_{cR11}	8	4.0038	3.9986	4.0261	3.9842	0.0223	-0.0144

Table B-3 (Cont'd.)

Dimension of T-Connection Model 3 (Cont'd.)

B. Chord Length

Before Stress Freezing L_{cT} in	Before Stress Freezing L_{cB} in	After Stress Freezing L_{cT} in	After Stress Freezing L_{cB} in	Change ΔL_{cT} in	Change ΔL_{cB} in
19.6895	19.6860	19.6627	19.7187	-0.0268	0.0327

C. Chord End Angular Displacement[a]

Before Stress Freezing				After Stress Freezing				Change			
δ_{RT} in	δ_{RB} in	δ_{LT} in	δ_{LB} in	δ_{RT} in	δ_{RB} in	δ_{LT} in	δ_{LB} in	$\Delta\delta_{RT}$ in	$\Delta\delta_{RB}$ in	$\Delta\delta_{LT}$ in	$\Delta\delta_{LB}$ in
0.006	0.0	0.0	0.003	0.028	0	0.024	0	0.022	0.0	0.024	-0.03

[a] Positive values measured from the vertical toward the center of the connection

D. Brace Diameter

Designation	Distance in	Before Stress Freezing D_{bL} in	Before Stress Freezing D_{bT} in	After Stress Freezing D_{bL} in	After Stress Freezing D_{bT} in	Change ΔD_{bL} in	Change Δ_{bT} in
L_{b-1}	-¼	-	2.0160	-	2.0141	-	-0.0019
L_{b0}	0	-	2.0160	-	2.0139	-	-0.0021
L_{b1}	¼	2.0108	2.0160	2.0129	2.0117	0.0021	-0.0043
L_{b2}	½	2.0106	2.0150	2.0081	2.0166	-0.0025	0.0016
L_{b3}	1	2.0084	2.0150	1.9981	2.0241	-0.0103	0.0091
L_{b4}	1½	2.0090	2.0147	1.9913	2.0290	-0.0177	0.0143
L_{b5}	2	2.0095	2.0159	1.9886	2.0312	-0.0209	0.0153
L_{b6}	2½	2.0100	2.0140	1.9864	2.0318	-0.0236	0.0178
L_{b7}	3	2.0096	2.0140	1.9864	2.0326	-0.0232	0.0186
L_{b8}	4	2.0098	2.0132	1.9878	2.0306	-0.0220	0.0174
L_{b9}	5	2.0106	2.0133	1.9920	2.0285	-0.0186	0.0152
L_{b10}	6	2.0108	2.0133	2.0031	2.0290	-0.0077	0.0157

Table B-3 (Cont'd.)

Dimension of T-Connection Model 3 (Cont'd.)

E. Brace Length

Before Stress Freezing L_{bR} in	Before Stress Freezing L_{bL} in	After Stress Freezing L_{bR} in	After Stress Freezing L_{bL} in	Change ΔL_{bR} in	Change ΔL_{bL} in
8.206	8.205	8.220	8.218	0.014	0.013

F. Brace End Angular Displacement[a]

Before Stress Freezing δ_N in	Before Stress Freezing δ_F in	After Stress Freezing δ_N in	After Stress Freezing δ_F in	Change $\Delta\delta_N$ in	Change $\Delta\delta_F$ in
0.0	0.003	0.0	0.0	0.0	-0.003

[a] Positive values measured from the vertical toward the center of the connection

APPENDIX C

DEVELOPMENT OF PLASTIC FOR PHOTOELASTIC MODELS

APPENDIX C

DEVELOPMENT OF PLASTIC FOR PHOTOELASTIC MODELS

The successful application of photoelasticity is highly dependent on availability of model material. Even though the fundamental laws of photoelasticity were known 130 years ago, no engineering application of photoelasticity was attempted until the introduction of celluloid in about 1900. Solakian (1935) applied twisting torque to a round Marblette bar after heating to 180°C and permitting it to cool under load. A transverse slice of the bar showed a stress fringe pattern. This was the beginning of the fixation or stress freezing method currently so popular in three-dimensional photoelasticity.

EARLY PHOTOELASTIC PLASTICS

Bakelite (Hetényi 1939), glycerin phthalic anhydride resin, was used in the United States for initial fixation method tests. It was quickly followed by Fosterite (Leven 1948), styrene polyester resin; Kreston (Taylor 1950), allyl ester resin; and Castolite (Frocht 1954), modified polyester resin. However, introduction of epoxy resin (D'Agostino 1955) in the 1950's as a model casting material provided three-dimensional photoelasticity with considerable momentum because of its outstanding advantages.

STANDARD EPOXY RESIN

A major contribution to three-dimensional photoelasticity was made when Leven (1963) reported development of the "standard epoxy" resin. Leven carefully compared 10 resins cured with acid anhydrides and amines. The investigation resulted in developing resin having the composition and characteristics shown in Tables C-1 and C-2, respectively.

Table C-1

Composition of Standard Epoxy Resin

100 parts resin by weight	- Bakelite ERL 2774[a]
42 phr[b]	- Phthalic anhydride
20 phr	- Hexahydrophthalic-anhydride

[a] Bakelite ERL 2774, Bakelite Company (a Division of Union Carbide and Carbon Corporation, 30 East 42 Street, New York, New York.
[b] Parts per hundred resin.

Table C-2

Characteristics of Standard Epoxy Resin

Critical Temperature, °C; T_{cr}	162- 175
Effective Elastic Modulus, psi; E_{eff}	5300-6500
Effective Material Fringe Value, psi/fringe/inch, f_σ	2.48-2.84
Figure of Merit; Q	2100-2400

However, mixing and curing the standard epoxy is difficult and time consuming because

1) HEX-anhydride precipitates if gelation temperature is allowed

to decrease even slightly,

2) exothermic reaction occurs if gelation temperature is allowed to increase even slightly, and

3) residual stresses form if a large casting is permitted to cool rapidly.

Leven avoids these problems by casting with considerable care large solid cylinders of resin from which a variety of models can be fabircated. This procedure is very desirable if models of unknown configuration are to be fabricated. However, in the case of tubular connections where the configuration is known, that is, hollow circular cylinders, components can be cast in specially prepared molds. A mold with a center cylindrical core is desirable to decrease the weight of resin. This special condition, plus the above mentioned difficulties inherent with the standard plastic, prompted an investigation into amine cured epoxy. It was expected that considerable casting time could be saved if an amine cured resin could be used. The investigation reported below was made in association with F. W. Nordstrom.

TESTING AMINE CURED EPOXY RESIN FOR T-CONNECTION MODELS

The investigation of amine cured resins was limited to two low viscosity EPON® resins manufactured by Shell Chemical Company. These resins were selected because (1) they are typical of low viscosity resins available from major chemical supply houses, and (2) Leven (1963) reported EPON to have good sensitivity. Refer to Appendix A for suppliers of resins and other materials. Table C-3 summarizes the properties of the two resins.

Table C-3

EPON® Resin Typical Properties

EPON No.	815	828
Color, 25°C, Gardner[a]	5 max	4 max
Viscosity, 25°C, Poises[b]	5-7	100-160
Epoxide Equivalent[c]	175-195	185-192
Weight per gal, lbs, 20°C	9.5	9.7
Density, g/ml, 20°C	1.133	1.168
Refractive Index, 25°C	1.545-1.560	1.570-1.575
Flash Point, Tag Open Cut, °F	> 175	> 175
Hydroxyl Content, equiv., OH/100 g resin	0.05	0.06
Average Molecular Weight (approx.)	330	380
Equiv. Weight (g resin to esterify one mole of acid)	85	85

[a] Color of Transparent Liquids, ASTM D1544-58T.
[b] Kinematic Viscosity, ASTM D445-53T.
[c] Grams of Resin Containing Gram-Equivalent of Epoxide, ASTM D1652-59T.

The following amine curing agents were investigated, Table C-4. Diethylaminopropylamine (DEP) was determined most suitable for photoelastic needs as discussed below.

Table C-4

Amine Curing Agents

Curing Agent Designation	Chemical Name	Chemical Type
Shell "A"	Diethylaminopropylamine (DEP)	Polyamine
Shell "D"	-	Polyamine Salt
DTA	Diethylenetriamine (DTA)	Polyamine
Jefferson 400	Polyoxpropylenediamine 400	Polyamine
Genamid 250 (G-250)	-	Polyamine

CHARACTERISTICS OF AMINE CURED RESINS

Table C-5 summarizes the various combinations of resins and curing agents studied.

Table C-5

Amine Cured Resin Combinations

Resin Number	Parts by Weight	Curing Agent Designation (Table C-4)	Curing Agent Parts by Weight[a]	Curing Cycle	Remarks: Small Samples	Remarks: Large Samples
815	100	A	5	Room temp. + 180°F for 1 hour	Slight Color	Slight Color
815	100	A	7	Room temp. + 180°F for 1 hour	Slight Color	Slight Color Substantial Heat
815	100	D	10.5	Room temp. for 12 hours	Very Dark Color	-
815	100	Jefferson 400	4	Room temp.	Soft & Pliable	-
828	100	A	6	Room temp. + 212°F for 1 hour	Dark Color	High Heat
828	100	A	8	Room temp.	Slightly Dark Color	Very high Heat
828	100	DTA	8	Room temp.	Dark Color	-
828	50	G-250	50	212°F for 1 hour	Dark Color Soft Pliable	-
828	70	G-250	30	212°F for 1 hour	Dark Color	

[a] Amount of curing agent normally specified by weight as parts per hundred resin, phr.

Initial screening tests were made by casting activated resins in small shallow metal dishes, two inches in diameter and 1/2 inch in depth. The observations made from these small samples are summarized in the remarks column of Table C-5. Results indicated curing agent A was best because of reasonably light color and apparent strength of the cured plastic. EPON® 815 and 828 were mixed in large batches and cast in 500 ml plastic cups. It was observed that resins activated with seven parts per hundred resin (by weight), phr, or higher of agent A or cured at high temperatures caused exothermic heating and gassing as predicted by Leven. However, EPON 815 cured with five phr of agent A at room temperature until firm (B-stage) and heated to 180°F for one hour produced what appeared to be an encouraging plastic; however, the color was darker than desired. Inquiry indicated that curing agent A contained a dye which was added as an indicator of complete mixing. The tests were repeated using undyed curing agent A (DEP) and a light colored resin resulted.

TEMPERATURE CONTROL OF DEP CURED RESIN

The study of DEP cured resin, Table C-5, and reports by Leven (1963) indicate reaction temperature control was required during curing to prevent (1) gassing of the resin, Figure C-1, or (2) thermal stressing of the casting. Accordingly, a study was made of methods of casting large batches of resins.

Large solid castings, 4-1/4 inches OD x 18 inches tall, of EPON 815 and 828 resin cured with five phr DEP were made in aluminum molds. Castings placed in an air-conditioned room, 75°F, during gelation showed marked gassing because of overheating. The use of

Fig. C-1 - Solid casting (left) made in water cooled aluminum mold using EPON 815® and 5 phr DEP. Curing cycle; gelation at room temperature (24 hours) followed by 185°F for 1 hour. Right, 500 ml pour of EPON 815® cured with 10 phr DEP showing internal gassing from exothermic heat

EPON® 828 was discontinued in favor of lower viscosity EPON 815, since the viscosity of EPON 828 was too high to allow air bubbles to rise to the surface of the casting.

Further investigation with five phr DEP cured EPON 815 resulted in casting a 4-1/4 inch OD x 18 inch solid cylinder in a jacketed aluminum mold equipped with circulating water. A section of a piece cut from the original successful casting is shown in Figure C-1. This casting technique has been advanced by the author to the point that an 8-3/8 inch OD x 6-3/16 inch ID x 48-inch tall cylinder can be cast. The aluminum mold consists of three concentric cylinders. The inner cylinder (core) is filled with tap water. The inside annulus contains the activated resin and the outer annulus provides space for circulating tap water.

Castings made for the tubular connections reported in this thesis do not require special temperature control since they are small, that is, 4 1/4 inch OD x 1/2 inch wall. The technique of casting these components is discussed in detail in Chapter 4 and Appendix D.

CHARACTERISTICS OF DEP CURED EPON 815 RESIN

So far only feasibility of casting EPON 815 has been established. It was necessary to establish that the proposed plastic had desirable photoelastic characteristics. Leven (1963) showed that DEP cured epoxy plastic has good photoelastic characteristics. However, it generally is numerically lower than the standard epoxy.

Critical Temperature

Critical temperature is defined as the temperature at which primary bonds of plastic relax. Critical temperature was determined for DEP cured EPON® 815 by testing a series of calibration bars, Figure C-2, at constant load but variable time and temperature. Based on Leven's (1963) study, the critical temperature was expected to be about 95°C. Thus, the majority of the bars were tested near this temperature, Table C-6.

Table C-6
Five phr DEP Cured EPON 815 Critical Temperature Data
(Calibration Bar Load 1003 g)

Calibration Bar No.	Oven Temperature °C	Test Duration min.	Fringe Order N
1	79	270	4.84
2	92	75	4.80
3	92	135	4.80
4	92	55	4.80
5	86	28	4.71
6	92	15	4.85
7	79	15	4.70
8	79	30	4.61
9	79	8	4.55
10	79	12	4.78
11	64	12.5	2.25

The critical temperature is close to 92°C as indicated by development of consistent fringe orders as a function of time, Figure C-3. An exact value of critical temperature was not determined since it will change slightly with each batch of resin prepared. However, the value of 92°C agrees well with 95°C reported by Leven (1963) for a similarly cured high viscosity plastic.

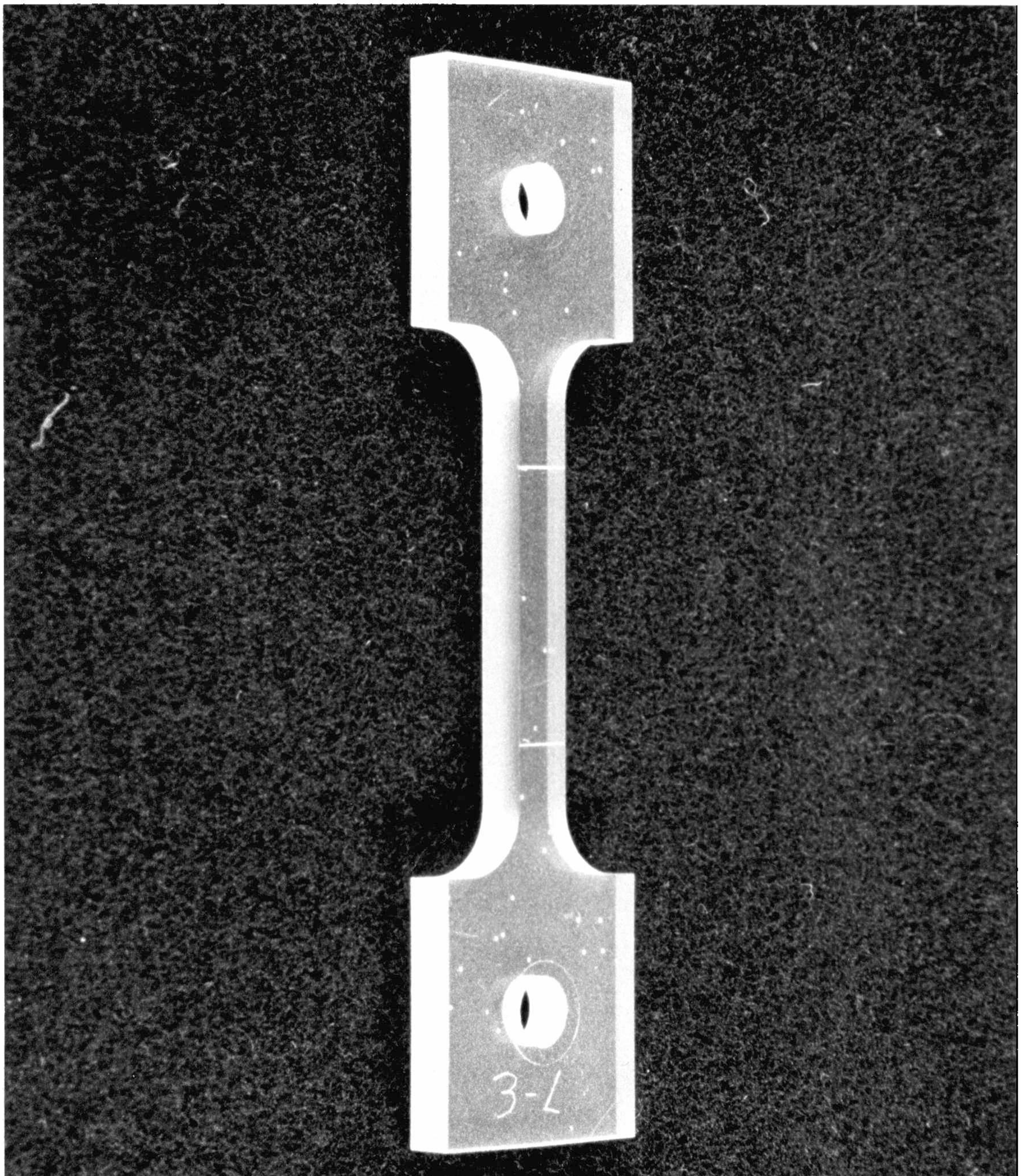

Fig. C-2 - Calibration bar used for determining physical and photo-elastic characteristics of EPON 815® cured with 5 phr DEP

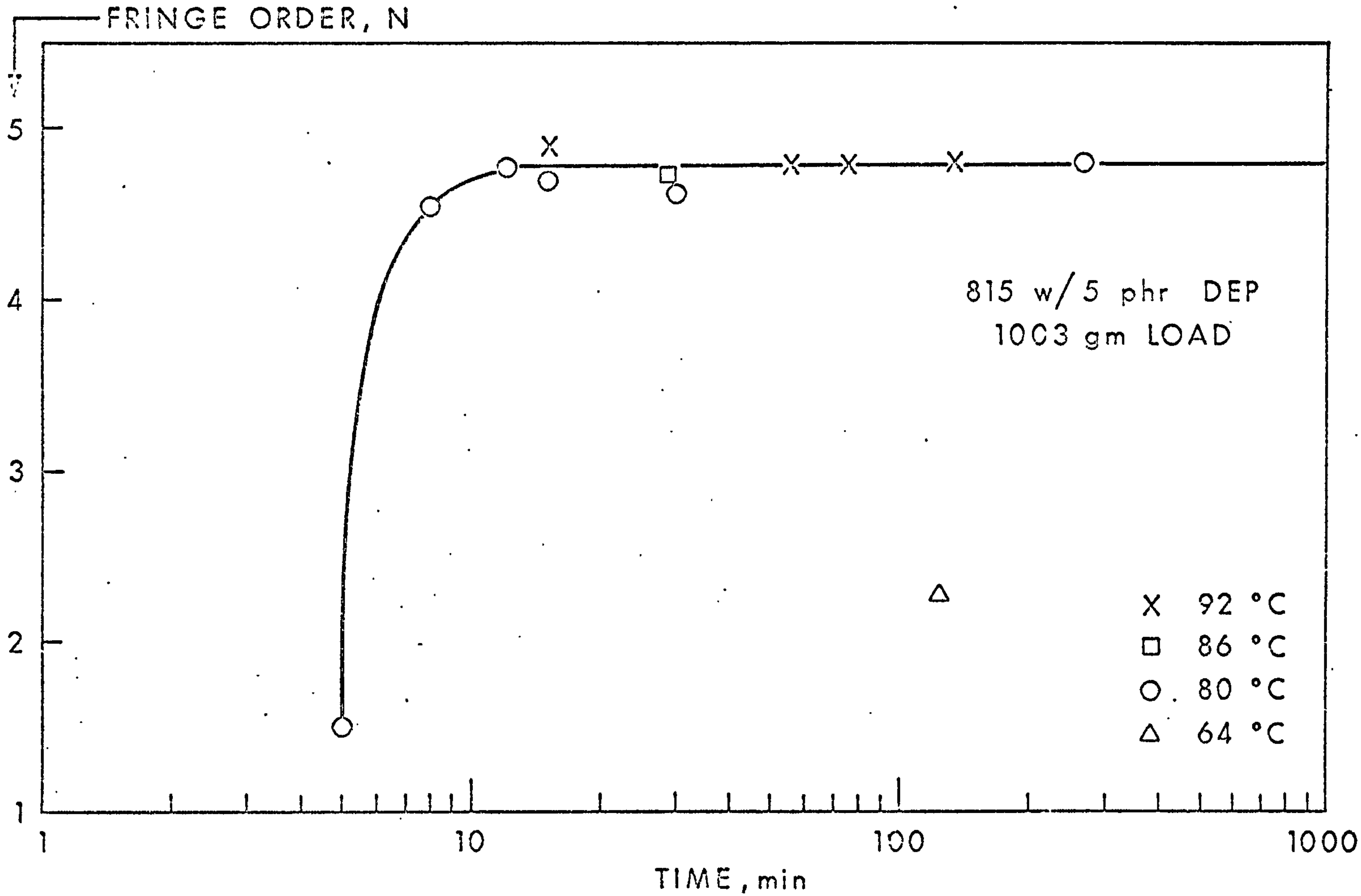

Fig. C-3 - Fringe order variation with time of load application for temperatures near the critical temperature for EPON 815® cured with 5 phr DEP

Elastic Modulus

The effective elastic modulus was determined from equation

$$E_{eff} = \frac{PL}{whe} \quad . \tag{C-1}$$

Data for equation (C-1) was obtained from calibration bars, Figure C-2,on which were scribed two transverse marks to form a gage length, L, about one inch long. Distance between marks was measured accurately with an optical comparator. The calibration bars were heated to 90°C, loaded, and cooled to room temperature while under load. The final length, L_f, was measured and the elongation, e, determined. The width, w, and thickness, h, of the shank of the bars were measured with a micrometer. Measurements for representative calibration bars are summarized in Table C-7. The effective elastic modulus ranges between 3350-4060 psi. This compares well with the value, 3500 psi, reported by Leven (1963). The modulus for the standard epoxy is 5300-6500 psi. This indicates that less deformation will occur at the same load for models fabricated from standard epoxy than from DEP amine cured epoxy. However, as indicated previously, excessive deformation was not a problem with the models reported in this thesis.

Material Stress Fringe Value

The material stress fringe value (Dalley 1965) was calculated from equation

$$f_\sigma = \frac{P}{wN} \quad . \tag{C-2}$$

Table C-7

Physical Properties of EPON® 815 Cured with Five phr DEP

No.	Calibration Bar: Orig. L in.	Final L_f in.	Elong. e in.	Initial Thickness h in.	Initial Width w in.	Load P g.	Stress Freezing: Temp. °C	Time min.	Fringe Order N	Effective Elastic Modulus E_{eff} psi	Effective Material Stress Fringe Value f_σ psi/fringe/inch	Figure of Merit Q
K	0.99442	1.00982	0.01542	0.1923	0.2532	1392.2	90	60	5.24	4060	2.32	1750
L	1.00857	1.02762	0.01905	0.1942	0.2536	1423.3	90	60	5.49	3350	2.26	1482
M	1.02615	1.04640	0.02025	0.1902	0.2470	1454.8	90	60	5.72	3470	2.27	1528
N	0.99892	1.01700	0.01808	0.1942	0.2520	1393.2	89	63	5.25	3460	2.33	1530
O	0.99863	1.01640	0.01777	0.1895	0.2494	1423.3	89	63	5.26	3800	2.39	1590
P	1.0013	1.01810	0.01679	0.1933	0.2528	1454.8	89	63	5.44	3980	2.33	1710

Using the data from Table C-7 in equation (C-2) indicates that fringe values of DEP cured EPON® 815 vary between 2.26 and 2.39 psi/fringe/inch of thickness. Thus, the DEP cured EPON 815 is slightly more sensitive than the standard epoxy. However, it is interesting to note that the fringe values listed in Table C-7 are high compared with those ($f_\sigma = 1.27$) reported by Leven (1963) for a heavier epoxy* cured with 10 phr DEP. No reason has thus far been found for the marked difference in values.

Figure of Merit

The ratio of effective modulus, E_{eff}, to material stress fringe value, f_σ, is known as the Figure of Merit, equation (C-3).

$$Q = \frac{E_{eff}}{f_\sigma} \tag{C-3}$$

Based on the values from Table C-7, the Figure of Merit ranges from 1482 to 1750. This compares with 2100 to 2450 for the standard epoxy. Therefore, DEP cured resin would not be considered as suitable for photoelastic modeling as standard epoxy.

Time Edge Effect

Leven (1963) studied the effect of moisture on the stress fringe pattern along the edge of the model. No specific investigation of the phenomenon was made during the determination of the DEP cured EPON 815 plastic. Experience shows that if the model or slices are stored in an oven at 100°F for 1-2 weeks before analysis, little or no time edge effect is noted.

*Bakelite ERL 2774, Bakelite Company (a Division of Union Carbide and Carbon Corp.), 30 East 42nd Street, New York, New York.

SUMMARY

Table C-8 shows a comparison of DEP cured EPON® 815 and standard epoxy.

Table C-8

Comparison of Epoxy Resins

	Standard Epoxy	DEP Cured EPON 815
Critical Temperature, T_{cr}, °C	162- 175	92- 95
Effective Elastic Modulus, E_{eff}	5300-6500	3350- 4060
Effective Material Stress Fringe Value, f_σ	2.48-2.84	2.26-2.37
Figure of Merit, Q	2100-2450	1482-1750

Casting of DEP cured EPON 815 is easier than casting standard epoxy because temperature during gelation is not so critical. Room temperature cooling water is sufficient to limit the exothermic reaction to provide large, solid, bubble free castings.

The properties of DEP cured EPON 815 are good, particularly the sensitivity to stress. The elastic modulus of DEP cured resin is lower than the standard epoxy, but the difference is not sufficient to cause large deformation during loading.

It should be noted that the critical temperature of the standard epoxy is almost twice that of the DEP cured EPON 815. This provides an advantage since low temperature ovens can be used for stress freezing models. However, since the critical temperature is low, care must be taken to avoid exposing models slices to elevated temperature. It is recommended that slices be maintained in an oven at a temperature of 100°F when not being analyzed.

DEP cured EPON® 815 was used for all castings from which T-connection models and calibration bars were machined for this investigation. The stress sensitivity and ease of casting of DEP cured EPON 815 were the dominant factors which lead to the preference of this material over standard epoxy.

APPENDIX D

CASTING PROCEDURE FOR PHOTOELASTIC T-CONNECTION MODEL COMPONENTS

APPENDIX D

CASTING PROCEDURES FOR T-CONNECTION COMPONENTS

Two separate molds were used in preparing castings for T-connection models:

1) chord mold consisting of a 4-1/4 inch OD aluminum tube 24 inches long into which is centrally fitted a pasteboard mailing tube (core), Figure 4, and

2) brace mold consisting of a 2-3/8 inch ID aluminum tube 14 inches long, Figure 4.

The chord mold was assembled by securing with Ring epoxy adhesive the mailing tube core to an aluminum base plate. The plate was coated previously with RAM 225 mold release to prevent permanent adhesion of the epoxy. The aluminum tube interior was also coated with mold release after which it was attached to the plate with Ring adhesive, Figure 4. The mold was permitted to cure overnight.

The brace mold was prepared by plugging the end of a 2-3/8 inch ID aluminum tube with a rubber stopper which was secured with masking tape. The inside surface of the tube was coated with mold release. No core was provided in the brace mold, Figure 4.

Sufficient EPON® 815, 9.5 lb/gal, to fill the molds was placed in a discardable container, a plastic or tin plated gallon paint can. The weight of the liquid epoxy was determined accurately. Curing agent was added at the rate of five parts DEP per hundred parts resin by weight. Refer to Appendix A for a source of materials.

The DEP was stirred into the resin until the mixture was homogeneous. Care was taken to scrape the sides and bottom of the container to remove uncatalyzed epoxy and care was taken to avoid stirring air into the epoxy during mixing. When the mixture showed a consistent color, that is, no striations, the catalyzed epoxy was poured into the molds. The epoxy was poured down the inside of the tilted mold to decrease the likelihood of entry of air into the resin.

The molds were permitted to gel at room temperature, 75°F, for two days. The gelled epoxy was heated to 180°F for one hour to "tighten" the cure.

The cured plastic was removed from the molds by tapping them to break the seal between the plastic and the mold release. The resulting castings are shown in Figure 5.

APPENDIX E

MACHINING COMPONENTS FOR PHOTOELASTIC T-CONNECTION MODELS

APPENDIX E

MACHINING COMPONENTS FOR PHOTOELASTIC T-CONNECTION MODELS

Machining epoxy plastic is difficult because of its brittleness, low strength, and abrasiveness. Tungsten carbide cutting tools must be used and maintained sharp. Two styles of cutting tools (Bergeman 1947) were used--(1) right-hand corner tool, and (2) finishing tool, Figure E-1. The side cutting-edge angle of the right-hand corner tool was maintained at about 45-50°. The end cutting-edge angle was ground to about 40-45°. The end and side clearance angles were maintained at about 15°. Finishing tool side cutting- and end cutting-edge angles were ground to 15° and 40°, respectively. The nose angle points of the tools were ground slightly rounded to improve longevity. The right-hand corner tool was used in the lathe and milling machine.

CHORD TURNING AND BORING

The chord was machined to finished dimensions in a 13-inch geared-head lathe, Figure E-2. Refer to Appendix A for full description of equipment.

A one-inch thick plug of EPON® 828 activated with seven phr DEP was poured at one end of the chord casting. This provided a solid base on which to tighten the lathe chuck. The casting was centered in the four-jawed chuck by means of a dial indicator. A snug fitting plug was inserted into the tail-stock end of the chord casting so that a live tail-stock center could be used. The exterior surface of the

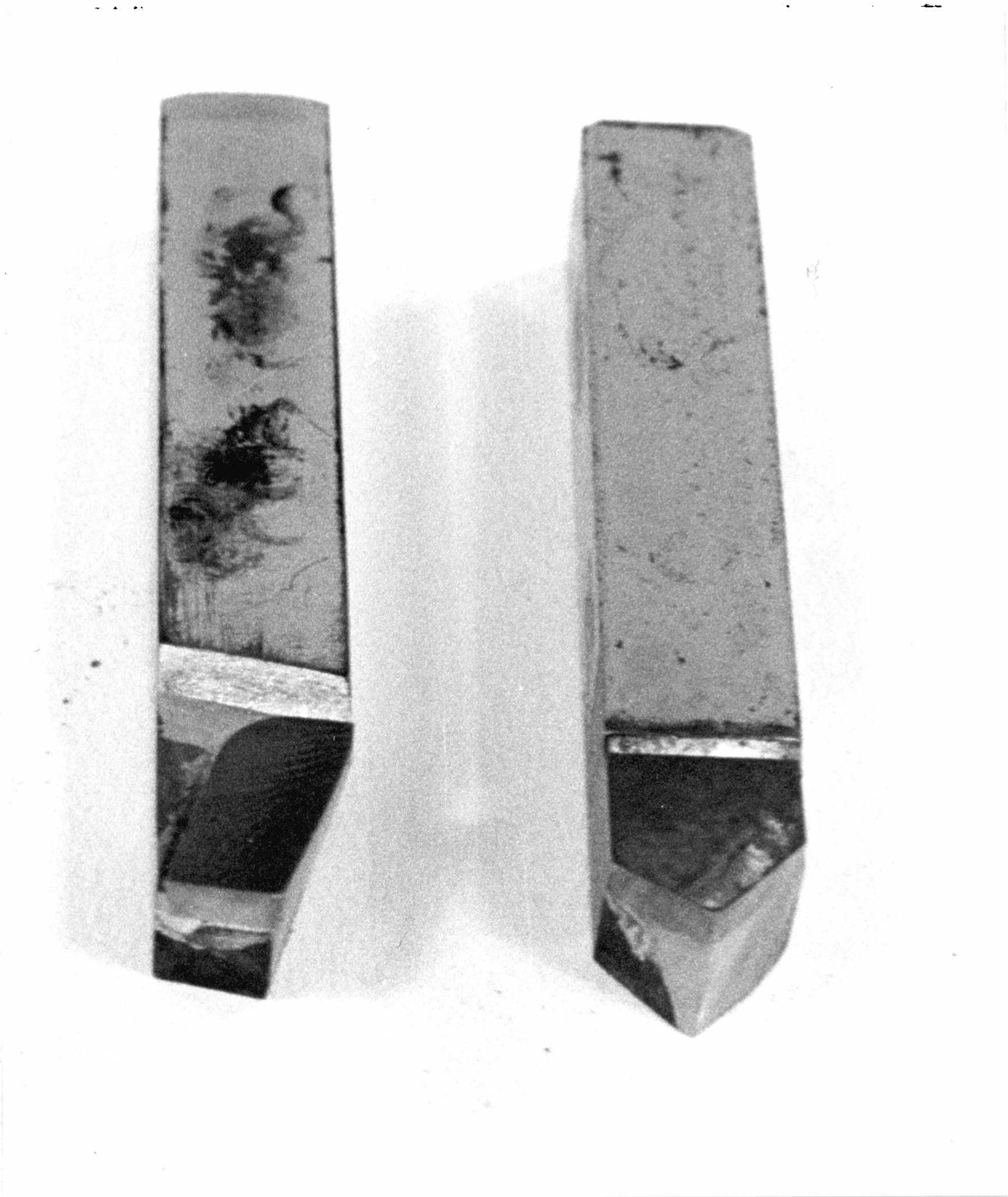

Fig. E-1 - Tungsten-carbide lathe tools - left, finishing tool and, right, right-hand corner tool

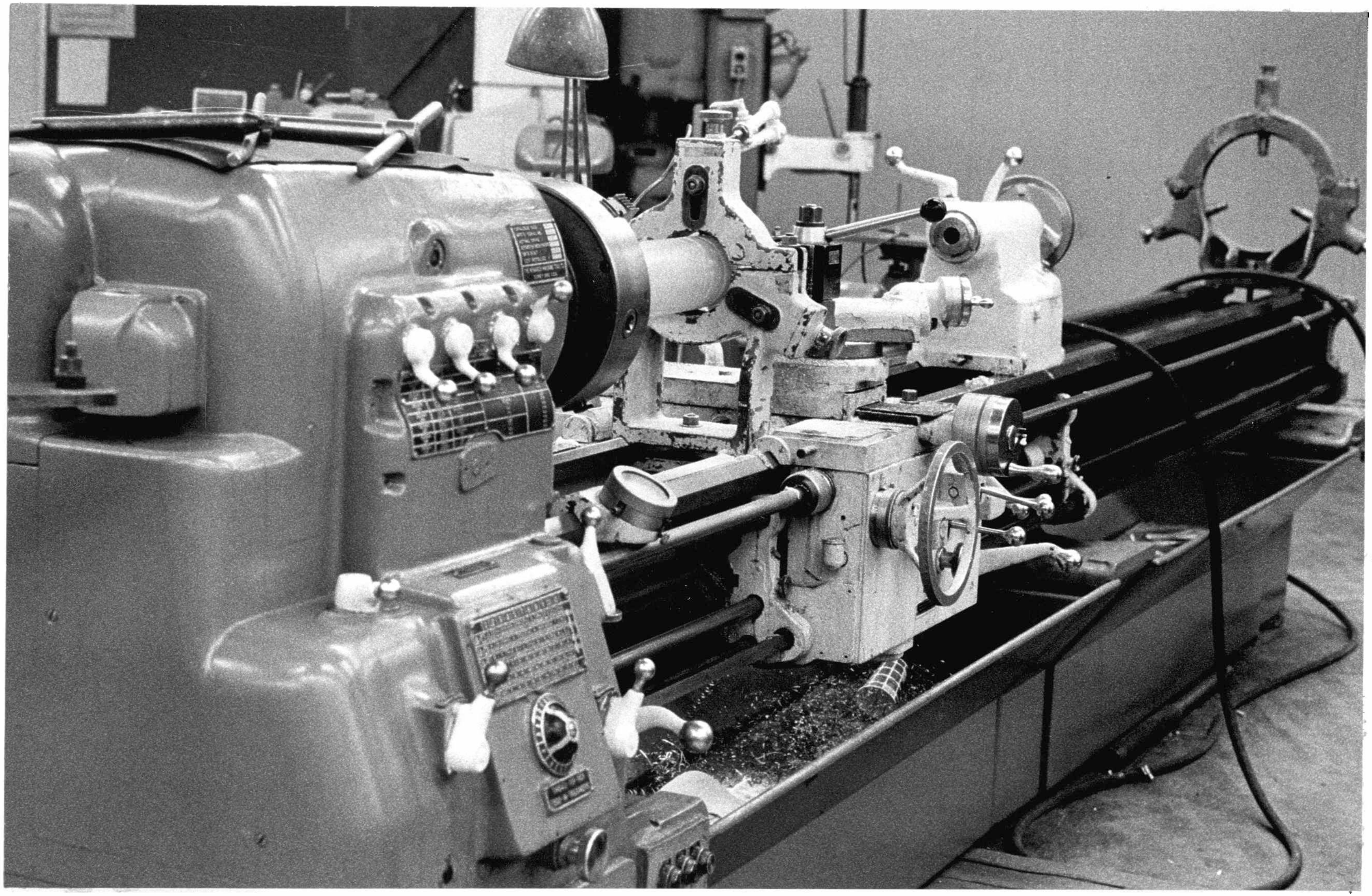

Fig. E-2 - Geared-head lathe used for turning model T-connection components casting was turned circular for about four inches at the tail-stock end. A roller bearing steady-rest was placed under this circular portion of the casting and the tail-stock and plug removed, Figures E-3 and E-4.

A two-inch OD boring bar fitted with a 3/8-inch right-hand corner tool at 45° to the bar axis was attached to the lathe compound rest, Figure E-3. The tool was placed upside-down in the bar so cutting was done on the back side of the chord while the piece was traveling upward. This permitted chips to escape the cutting edge more easily.

The chord was bored at 140 rpm, 0.0051 inches per revolution feed rate and about 0.0050 inch depth cut initially. As the inside diameter approached finished size the feed rate was progressively decreased to 0.0026 inch per revolution. When the ID was within 0.060 inch of finished dimensions, a three-inch boring bar was installed on the cross slide in place of the compound rest, Figure E-4.

The finish cuts, about 0.015 inch each, were made with the large bar to prevent tool chatter which roughens the finish. The lathe speed was reduced to 107 rpm and the feed to 0.0026 inch per revolution. The final cut was 0.005 inch to provide a smooth finish.

After the chord was bored to finished dimension, a close fitting plug was inserted in the hole and the plug center-bored for a tail-stock center. The steady rest was removed and the plugged chord supported by the tailstock.

The outside surface was turned to finished dimension by using a finishing tool, Figure E-5. The feeds and rotary speed were the same as used during boring. The completed chord was cut from the solid base with a tapered parting tool.

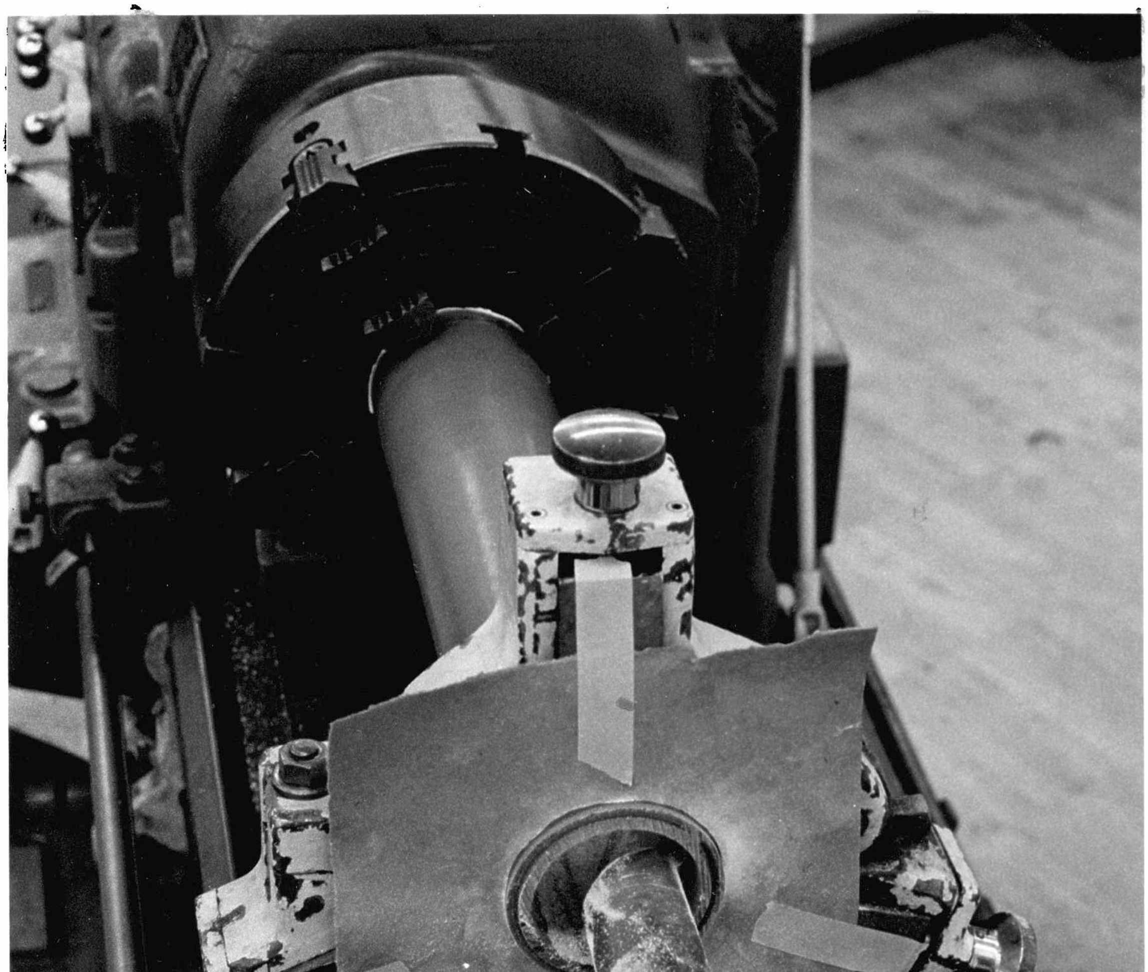

Fig. E-3 - Chord held in chuck and supported by steady rest. Two-inch boring bar fitted on compound rest

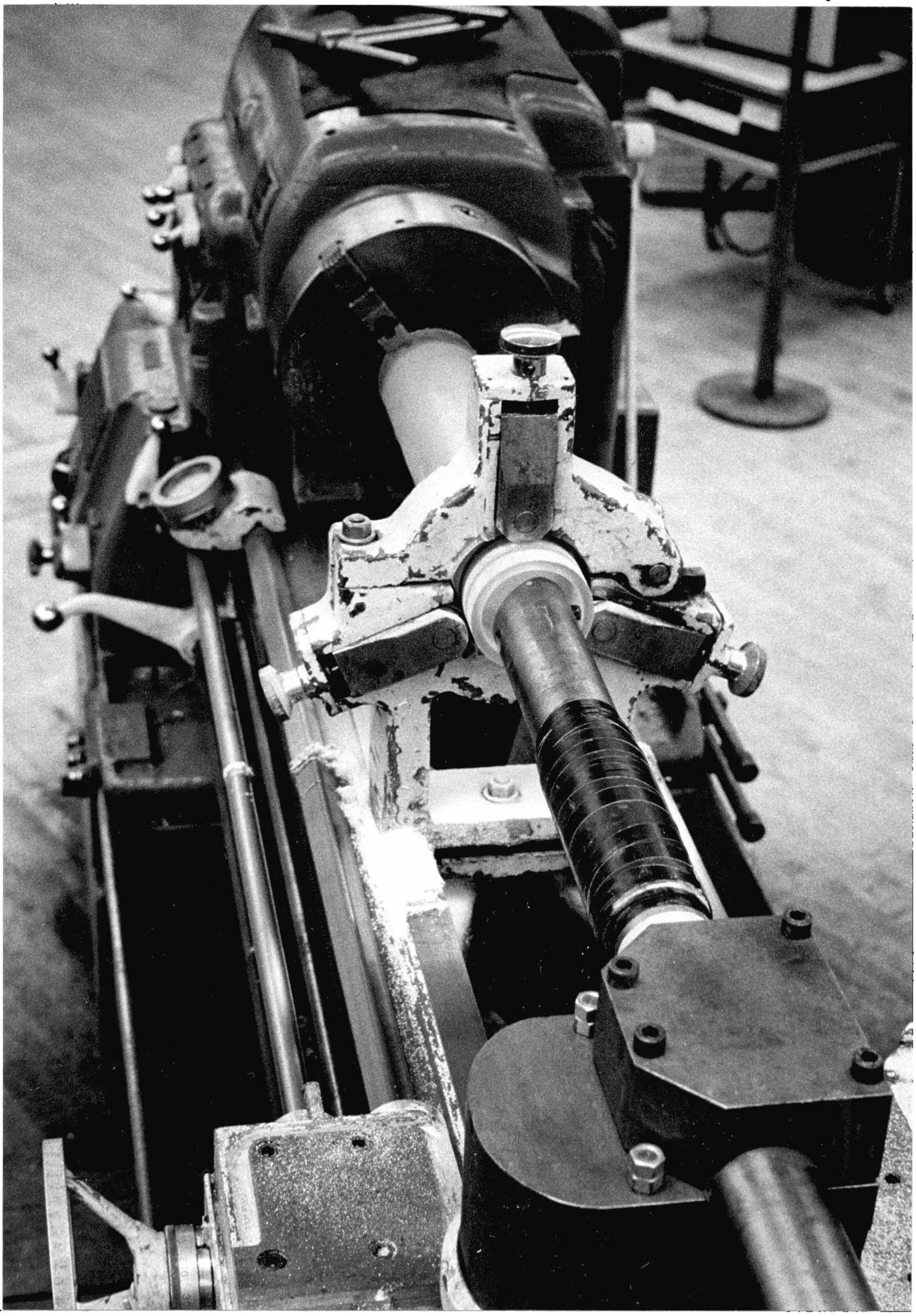

Fig. E-4 - Three-inch boring bar used to make finish cuts in chords

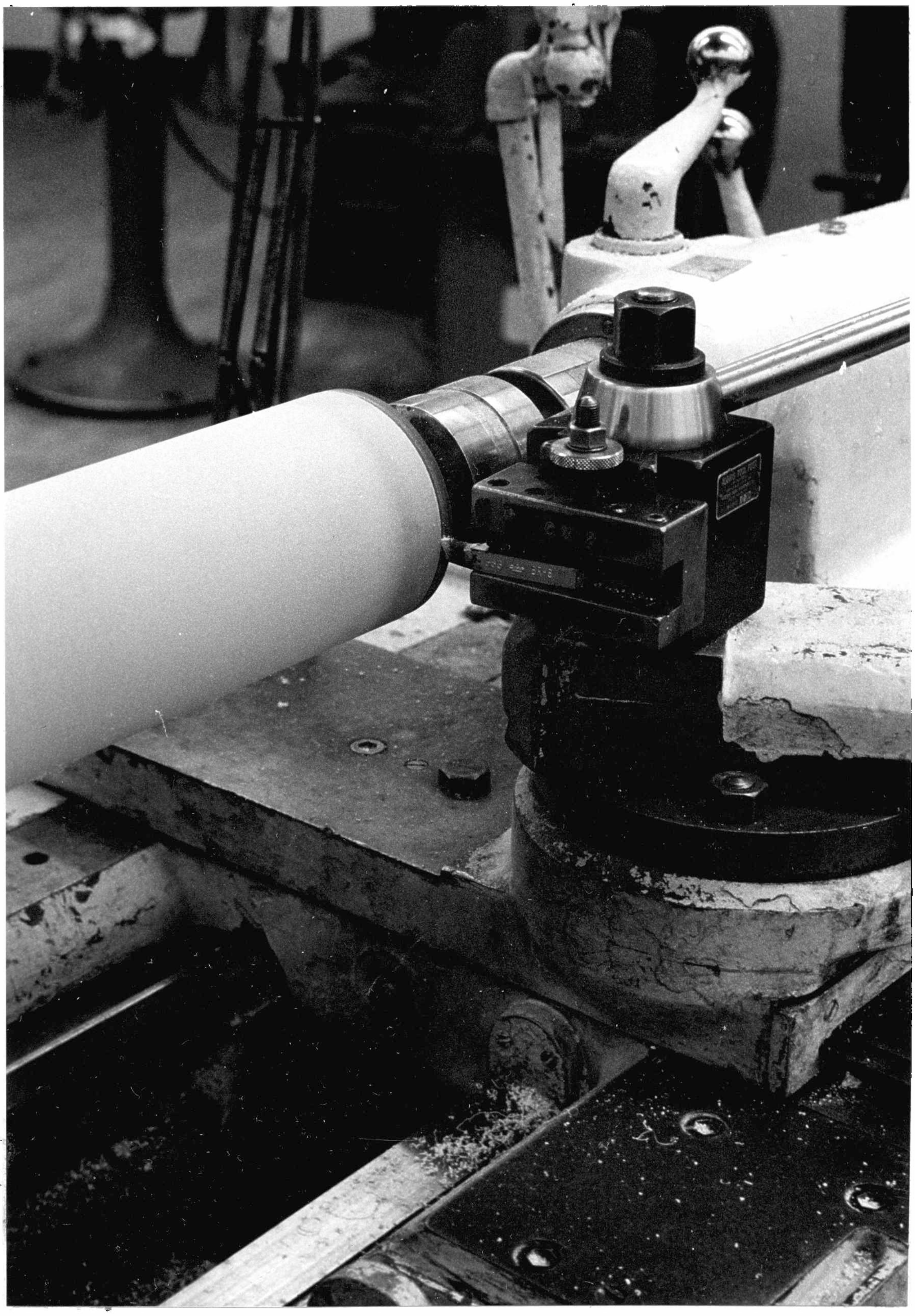

Fig. E-5 - Turning outside of chord in lathe using finishing tool

BRACE TURNING AND BORING

The brace casting, Figure 5, was made solid, then drilled to permit entry of a boring bar. This was performed in a manner similar to that used for preparing the chord for boring. The brace was chucked and adjusted for trueness. The solid end of the brace was center drilled and supported on the tail-stock center while the outboard end of the brace was turned cylindrical. Then the brace was supported on the steady rest.

A 3/4 inch two-fluted twist drill was used for drilling a pilot hole in the solid casting. The drill was provided with a chip breaker (Cleveland 1964) to decrease the tendency to hang-up in the plastic. The pilot hole was opened to 1-1/2 inches with a four fluted drill, Figure E-6. The brace was bored and turned as described for the chord except that a small boring bar was employed. The rotary speeds were 170 rpm and 140 rpm for rough and finish cuts, respectively.

BRACE INTERSECTION CURVE MILLING

The intersection curve was milled on one end of each brace by means of a vertical spindle milling machine. An epoxy plug and sleeve were machined to fit tightly inside and outside of the brace, respectively. When the plug and sleeve encased the brace, it became a composite cylinder of plastic about 2.5 inches in diameter, Figure E-7. Two of these cylinders were mounted face-to-face in Vee-blocks on the milling machine table. Sufficient space was left between the

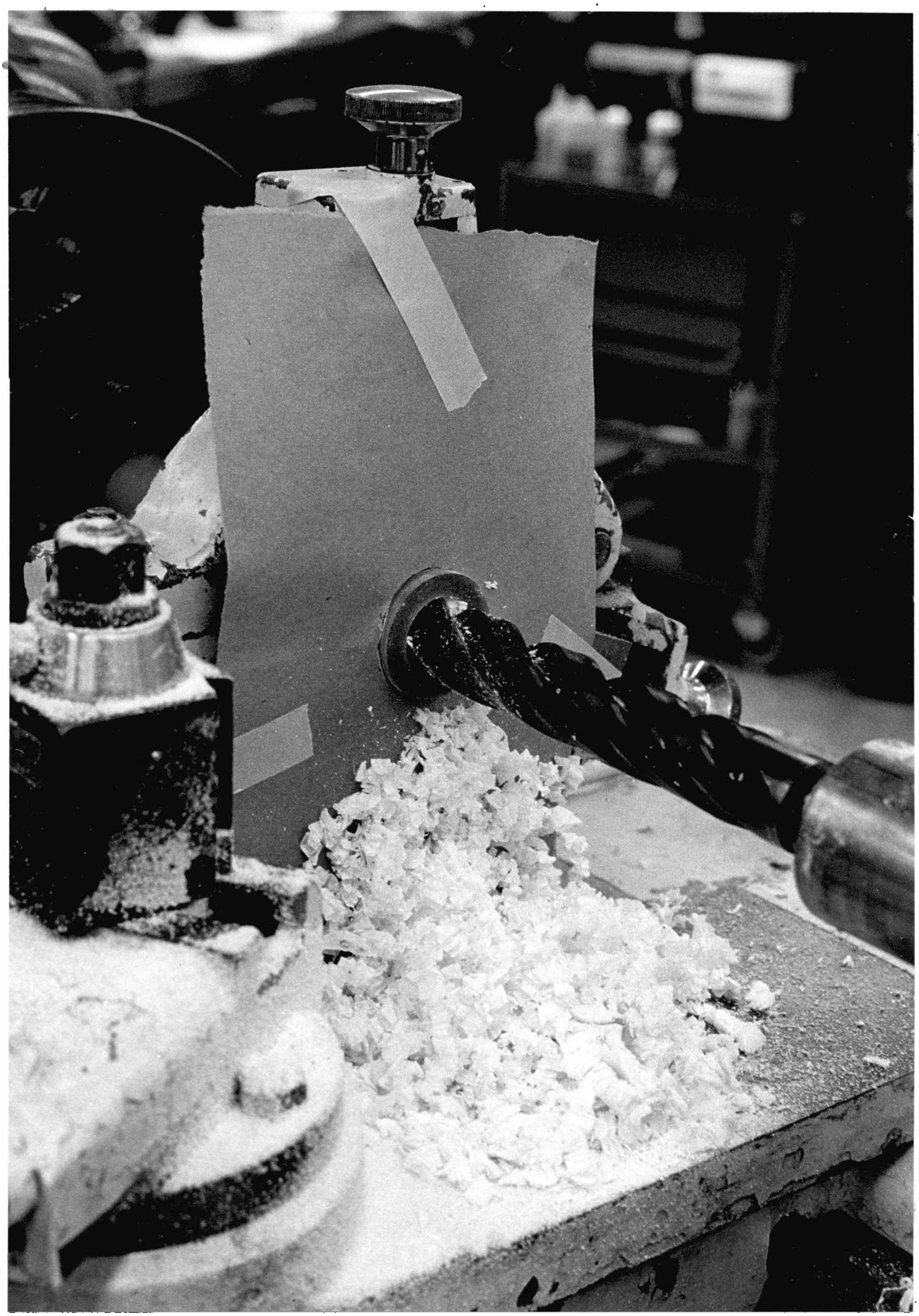

Fig. E-6 - Drilling the brace with a four-fluted twist drill

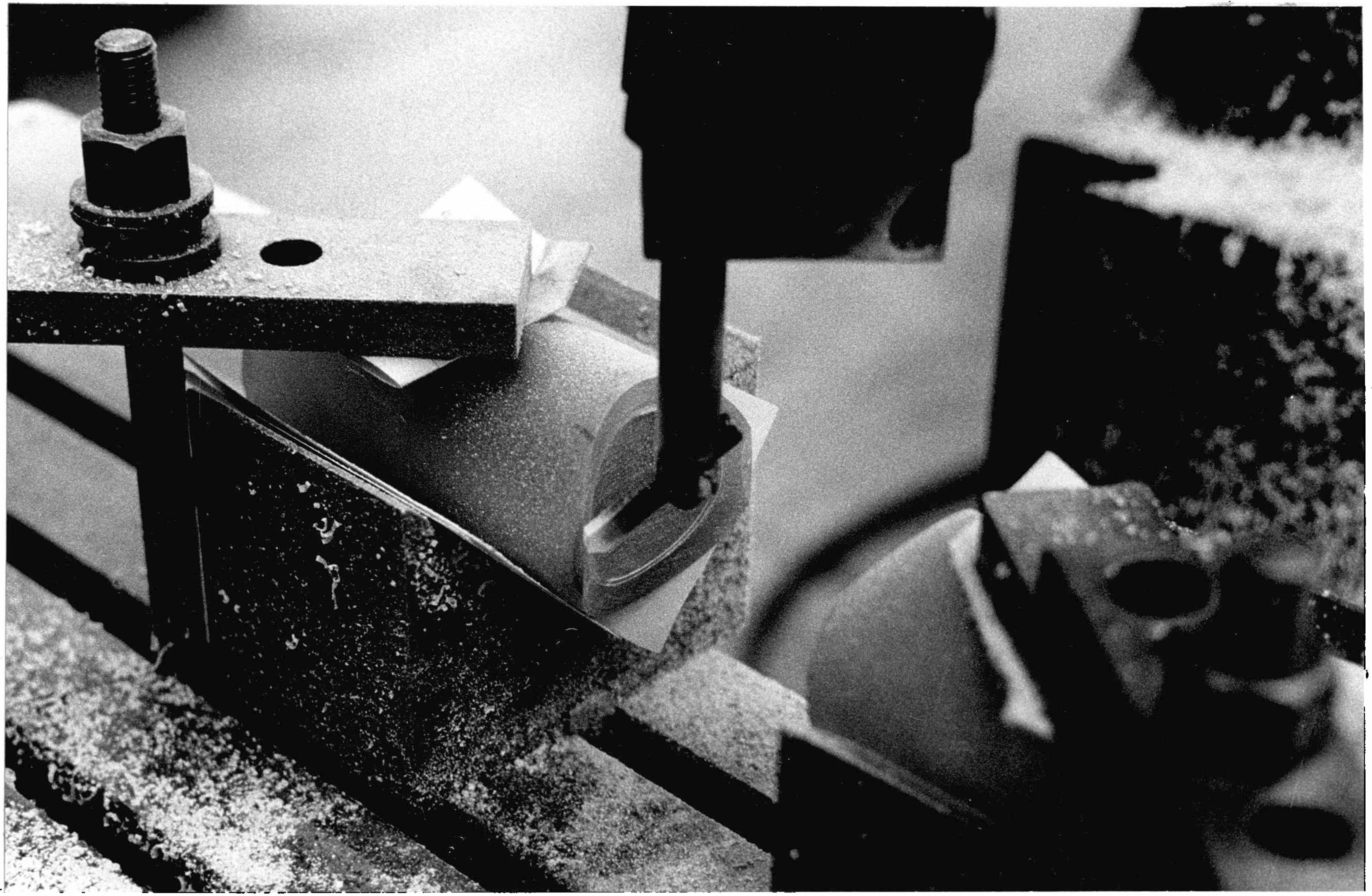

Fig. E-7 - Milling intersection curve in braces "sandwiched" between plug and sleeve faces to accept the boring head tool holder. A 1/4 inch right-hand corner tool was fitted into the holder at 45° to the vertical axis, Figure E-7. Intersection curves were formed by boring a four-inch vertical cylinder through the brace ends, Figure E-7. The tool was advanced horizontally 0.050 inch per cut. Finishing passes were made with 0.005 inch per cut. Spindle speed and feed were 660 rpm and 0.0015 in/rev., respectively. Finish dimensions were checked with an inside micrometer measuring between the milled faces.

The braces were cut to final length by refitting the plug and sleeve at the brace end away from the intersection curve, gripping the composite cylinder in a lathe chuck and cutting to length with a parting tool.

CALIBRATION BAR MACHINING

The sheet casting, Figure 5, was fly-cut to finished thickness, that is, about 0.20 inch, on a vertical spindle milling machine. Figure E-8 shows the sheet casting mounted on the jig plate attached to the milling machine table. The casting was held in place by double faced masking tape and modeling clay. The jig plate was secured to the milling machine table by double faced tape.

The fly cutter was equipped with a 3/8 inch right-hand corner tool, Figure E-1, and rotated at 250 rpm. The table feed was 5/8 inch per minute. The cut was varied from 0.025 inch to 0.005 inch per cut.

The sheet casting was finished on one side and then turned over. The finished surface was placed on the tape, the clay replaced, and the milling process repeated.

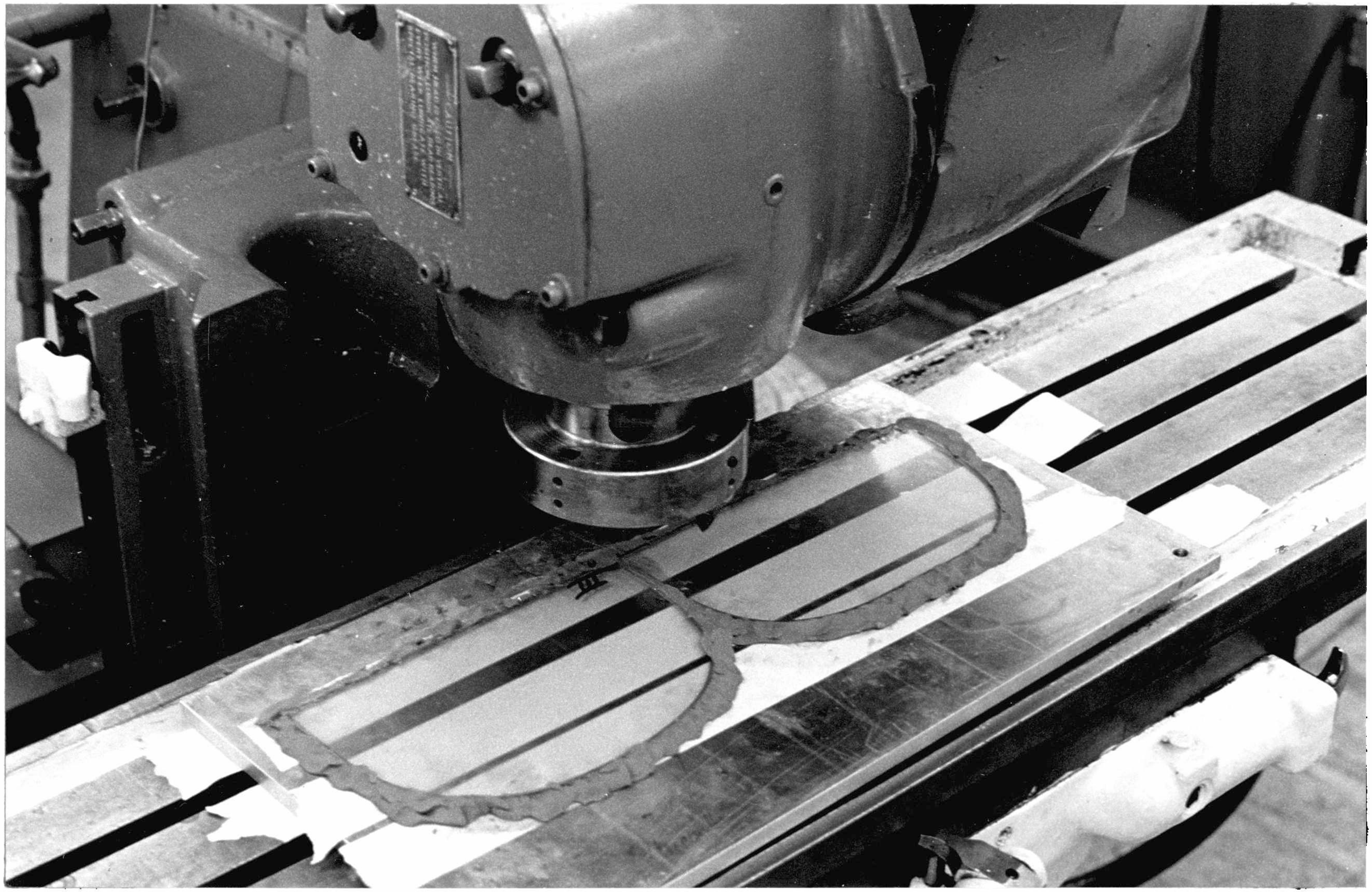

Fig. E-8 - Milling sheet casting surfaces

Machining to shape was performed on a numerically controlled vertical spindle milling machine, Figure E-9. This operation was programmed to drill the loading holes and rough-form the bars without interruption. The rough traverse was made around the bars using 7/16 inch three-fluted end mill. Two finish passes were made with a 1/2-inch end mill. Spindle speed was 1200 rpm. Water mist coolant was sprayed on the bars during machining.

Fig. E-9 - Cutting calibration bars held by jig mounted on table of numerically controlled milling machine

APPENDIX F

PHOTOELASTIC T-CONNECTION MODEL ASSEMBLY

APPENDIX F

PHOTOELASTIC T-CONNECTION MODEL ASSEMBLY

Loading of the T-connection models was performed by applying an axial load to the braces. Particular care was taken during cementing of the brace to the chord to assure a strong intersection weld.

Cement Preparation

Experimentation showed that a good epoxy cement could be made from 25 grams of EPON® 828 cured with 10 phr DEP. The addition of cab-o-sil was unnecessary if the catalyzed epoxy was permitted to thicken 5 1/2 hours before using. During development of the cementing procedure, air bubbles were beaten into the cement while stirring. These bubbles were not released from the curing epoxy because of the viscosity of EPON 828, Table C-3. Thus, the trial welds contained imperfections which could produce extraneous stresses at the intersection curve, Figure F-1. Further testing proved that thickening the catalized epoxy under a vacuum eliminated bubbles and produced a near imperfection-free weld, Figure F-2.

Assembly

The brace was centered on the chord to provide a symmetric structure. A circumferential line was drawn around the chord using a piece of straight heavy paper as a wrap-guide, Figure F-1. In addition, marks were provided one inch on each side of the centerline as guides.

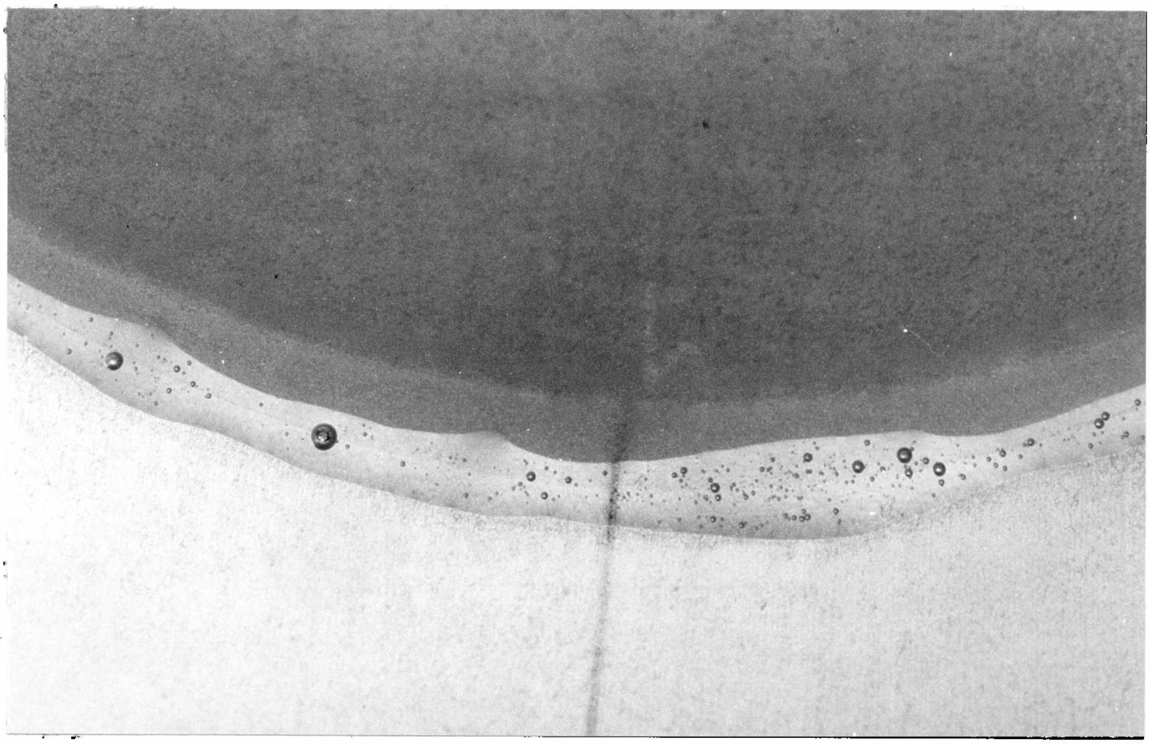

Fig. F-1 - Intersection weld containing air bubbles in the cement

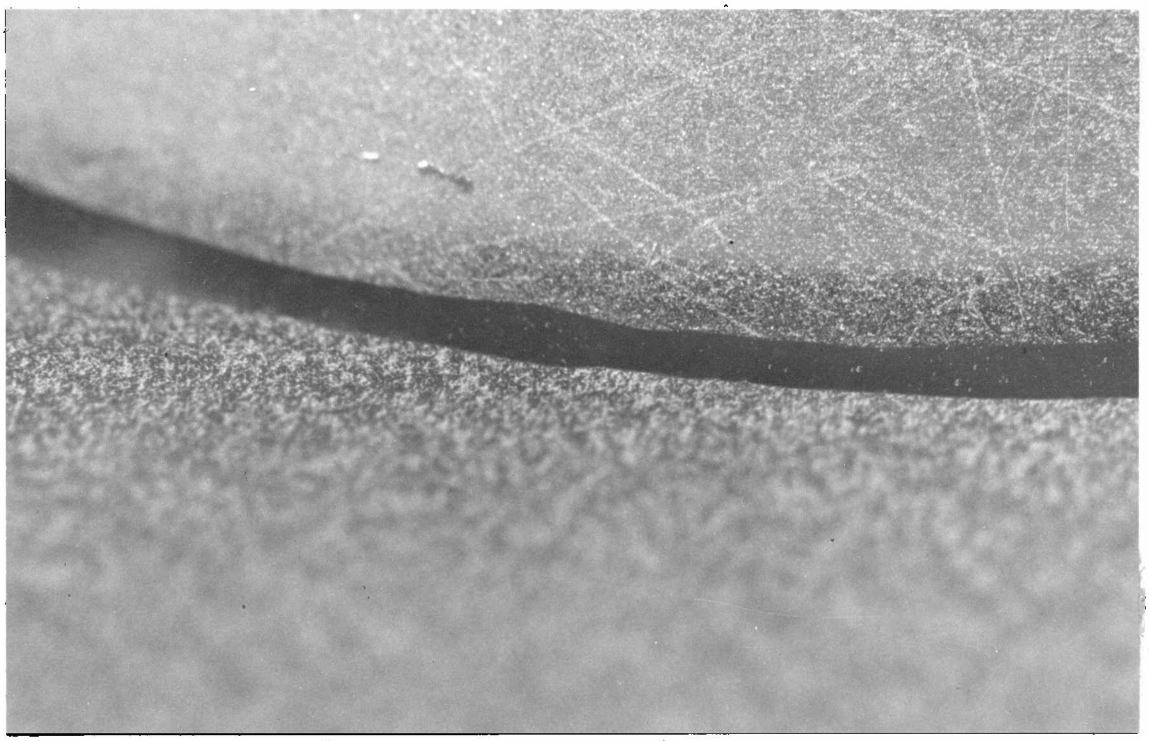

Fig. F-2 - Intersection weld made with epoxy cement thickened under a vacuum

Brace and chord surfaces to be cemented were cleaned with acetone. The intersection curve of the brace was lightly "buttered" with vacuum-thickened cement. The chord was held horizontal in V-blocks and the brace carefully placed on the chord. The brace was tapered to a jig and weighted with 400 grams (equivalent to about two psi), Figure 8. The assembled components were cured for 24 hours at room temperature. Tightening of the cure was accomplished by placing the assembly in 100°F oven overnight.

Prior to loading, chord and brace loading fixture diaphragms, Figure 10, were cemented in place with Ring epoxy adhesive.

APPENDIX G

PHOTOELASTIC MODEL SLICING

APPENDIX G

PHOTOELASTIC MODEL SLICING

Slicing of a three-dimensional photoelastic model is the process of transforming the model into a set of two-dimensional sections (slices), Figure 20, which can be analyzed by conventional photoelastic methods. Three operations are required in slice preparation: (1) scribing, (2) cutting, and (3) finishing.

The model was prepared for scribing by removing the diaphragms from each end of the chord, Figure 10. This was done by sawing through the chord wall with a jeweler's saw adjacent to the diaphragm. The brace end plate was retained to provide firm support when the connection was gripped in a chuck for indexing.

SCRIBING

The area to be scribed was painted with marking ink, Figure G-1. The brace end of the connection was gripped in an indexing-head chuck mounted on a granite surface plate, Figure G-1. Alignment was obtained by measuring the height of both ends of the brace and chord. With the indexing head at zero and the chord horizontal, a centerline was scribed around the entire connection using the height gage. Edge lines were scribed 0.125 inches above and below the centerline. The head was indexed 30° and next center and edge lines were scribed around the connection, Figure G-1. This operation was repeated every 30°. The completely scribed T-connection model is shown in Figure G-2.

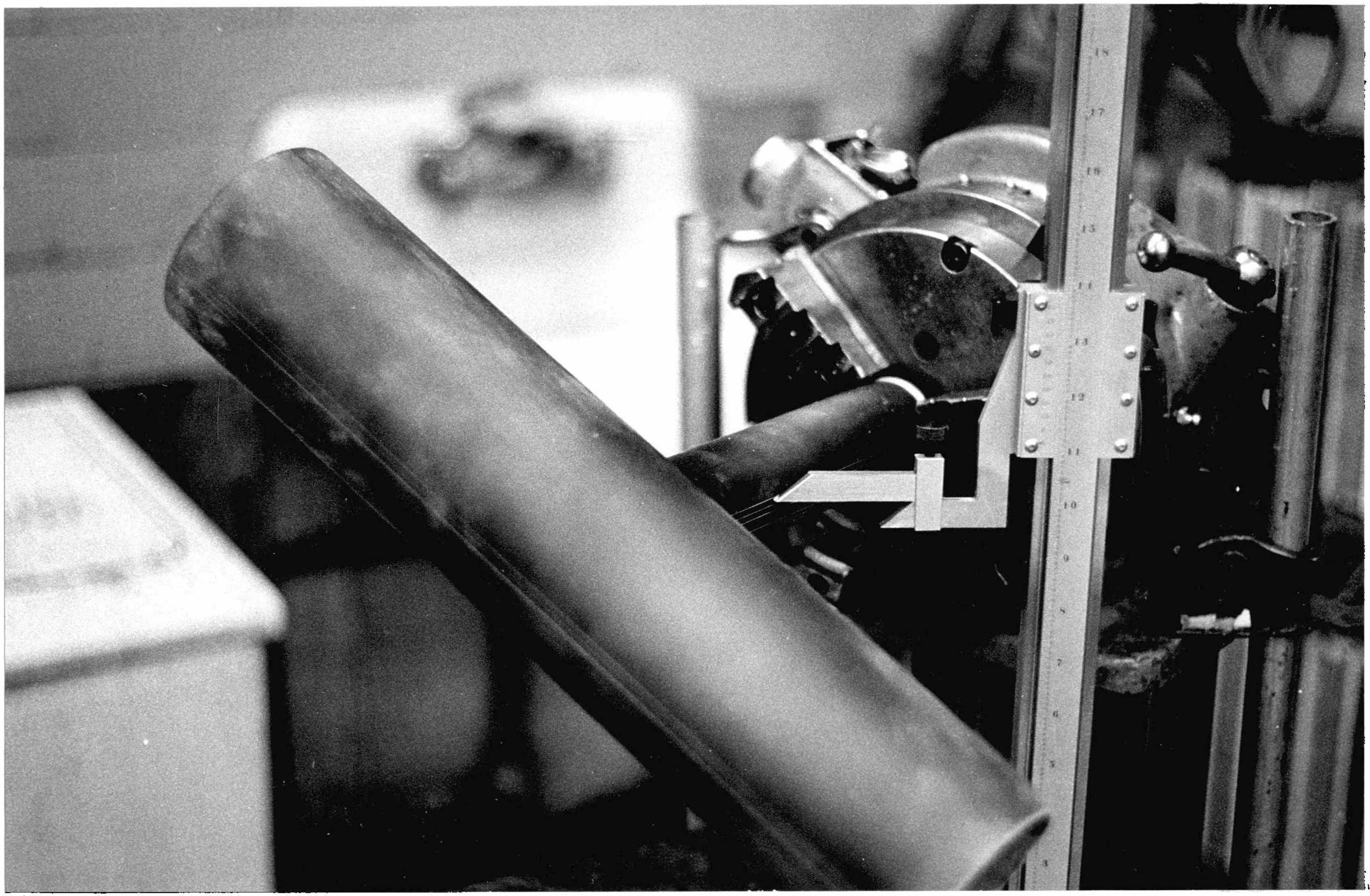

Fig. G-1 - T-connection coated with marking ink, held in indexing head chuck and scribed by height gage

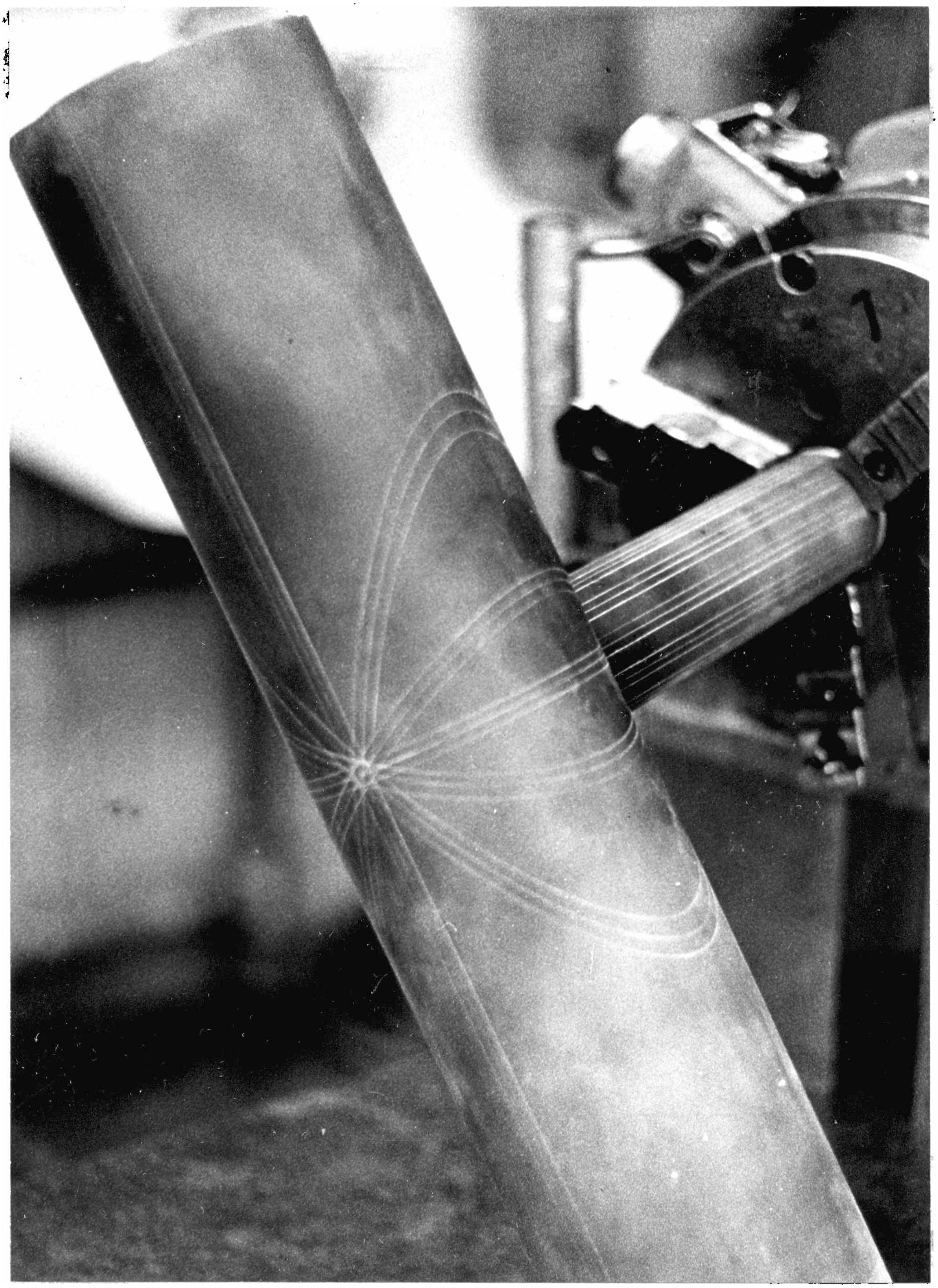

Fig. G-2 - T-connection model after scribing every 30° around brace

SLICE CUTTING

Cutting was performed with a dentist's burr held in a high speed grinder. The burr was held at an angle to the work piece and directed freehand, Figure 17. The brace was always cut first because it is so delicate. Several passes were made outside of the edge scribe lines with the burr. When a groove was cut in the tube wall, the burr was held normal to the surface and the cut made through the entire connection wall. The edge of the cut was made about 1/16 inch outside of the edge scribe line. This decreased the likelihood of subjecting the slice to excessive heat which would change stress patterns. Even with extreme care, some pattern distortion was observed near rough cuts which were not finish machined.

FINISHING

Slice edges were made parallel and smooth by fly-cutting on a vertical spindle milling machine, Figure 19. A piece of jig plate was attached to the milling machine table with double faced tape. The slices were positioned on the plate so the slice centerline was maintained at a constant elevation above the plate, Figure G-3. Centerline elevation was measured with a surface gage.

The slices were embedded in clay and the surfaces finished by fly-cutting with a right-hand corner tool, Table G-1.

Fig. G-3 - Maintaining constant slice center line elevation with surface gage

Table G-1

T-Connection Model Slice Finishing Data

	Depth of Cut (Inch)	Feed Rate (In/Min)	Spindle Speed (RPM)
Rough Cut	0.010	1.1	750
Final Cut	0.005	0.5	750

The finished slice surfaces were smooth and parallel, Figure 20.

SUBSLICING

Subslices are thin sections removed from a photoelastic model slice. Two types of subslicing are possible: (1) surface subslicing and (2) transverse subslicing, Figure G-4.

T-connection model surface subslices were prepared by cutting the model slice parallel to the free surfaces with a jeweler's saw. The resulting rough subslices, Figure G-4, were milled to uniform thickness with a high speed drill press, Figure G-5. The saw-cut surface of the subslice was smoothed at the rate of 0.001 inch per pass between a carbide burr and the milling guide, Figure G-5. Only light cuts were taken in order to assure maintaining the subslice at substantially ambient temperature during the smoothing operation.

Transverse subslices were smoothed by working down the saw-cut surfaces on emery paper placed on a granite surface plate.

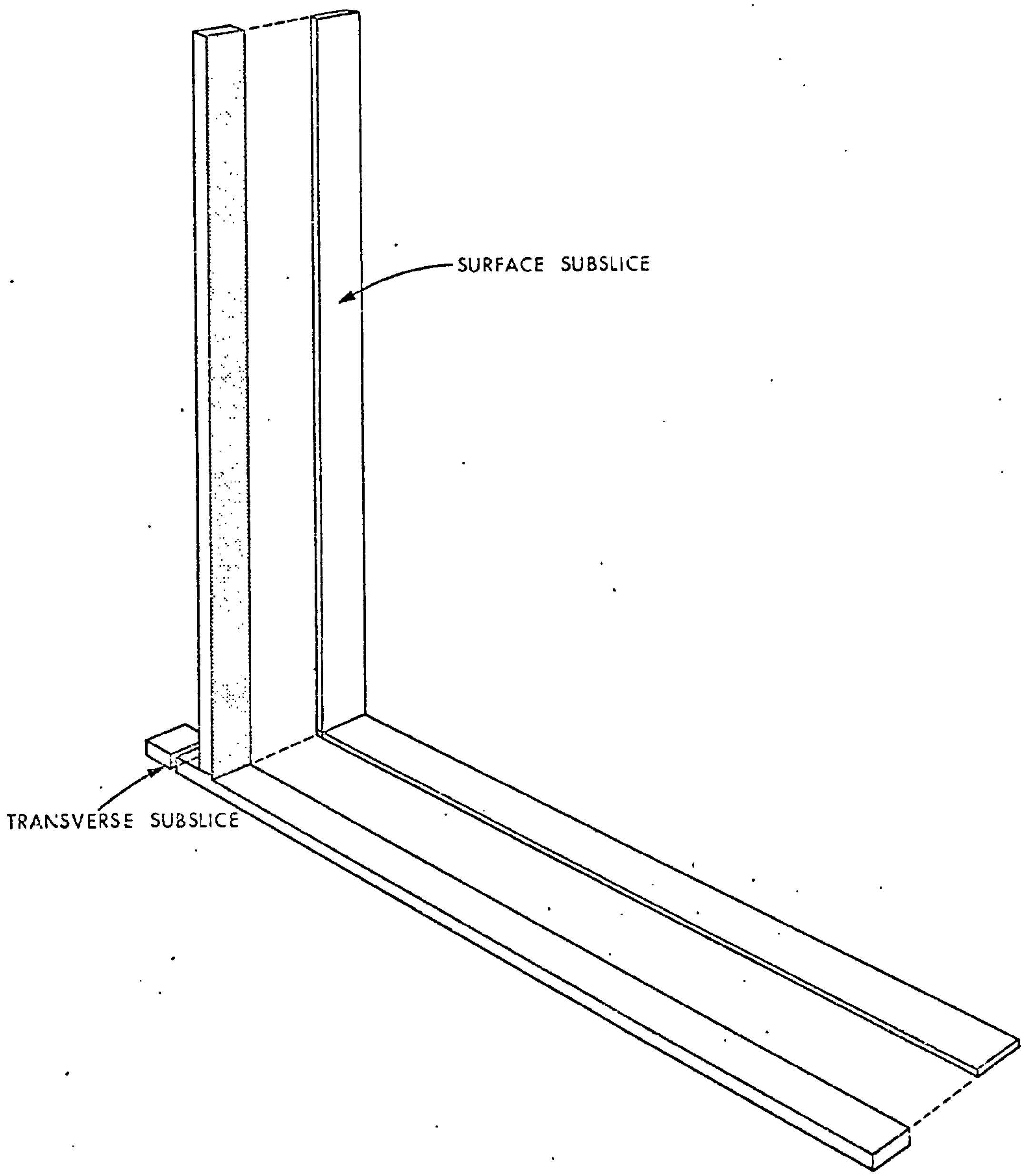

Fig. G-4 - Surface subslice and transverse subslice locations. (Surface subslices were removed from both sides of the slice even though only one subslice is shown.)

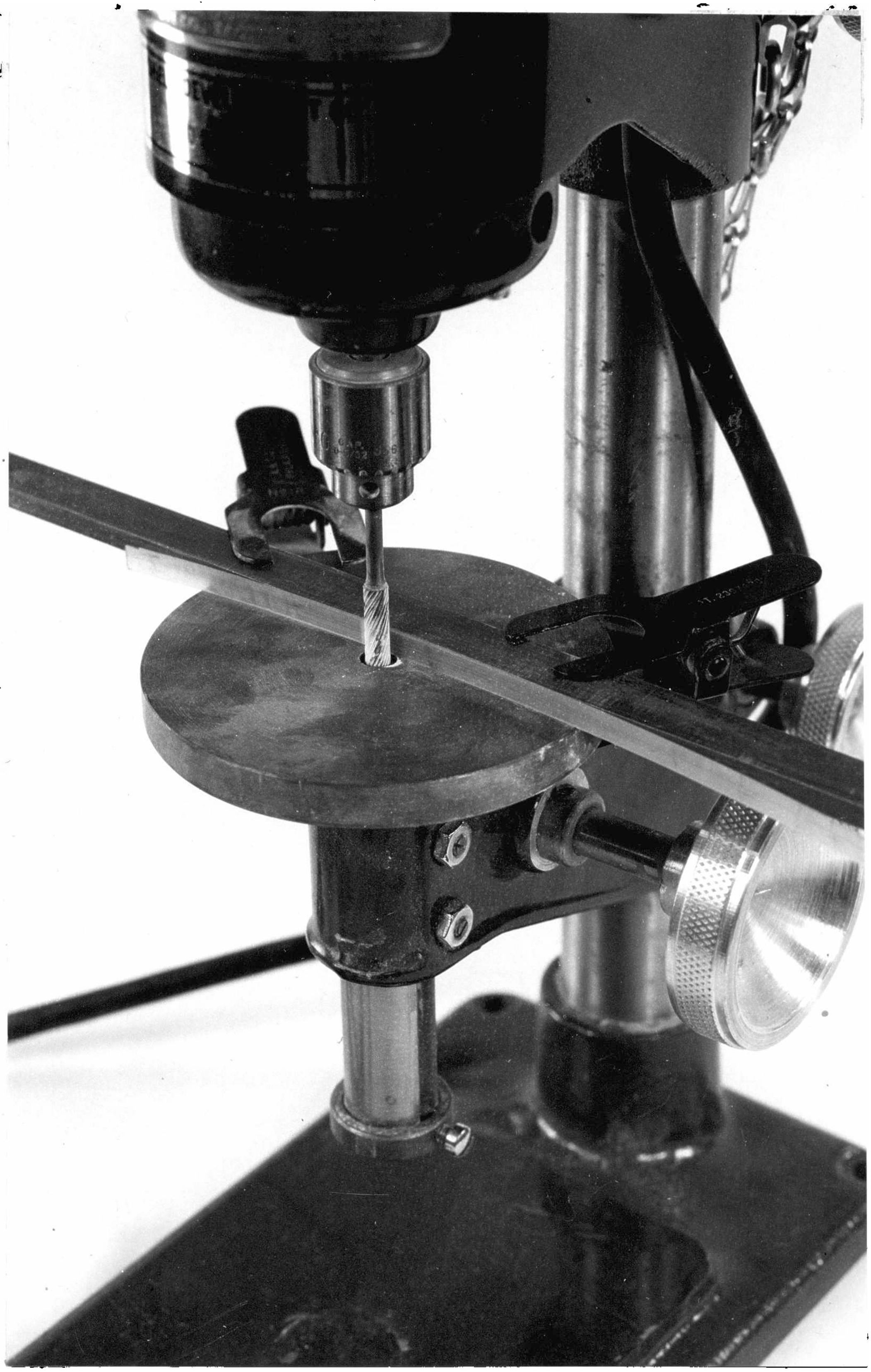

Fig. G-5 - Finishing surface subslice with carbide burr in high speed drill press

APPENDIX H

TARDY COMPENSATION

APPENDIX H

TARDY COMPENSATION

Determination of fractional isochromatic fringe orders permits improved accuracy of stress determination since it eliminates the necessity of working only with interger fringe orders.

Fractional fringe orders can be determined to the hundredth part of a fringe using Tardy Compensation (Dalley 1965, Tardy 1929). The technique entails placing the piece to be analyzed in a polariscope adjusted for dark field plane polarized light. The piece is rotated until an isoclinic passes through the point of interest. Then the polariscope is adjusted for circular polarized light. The analyzer is rotated until an isochromatic fringe produces extinction at the point of interest. The fringe order, N, at the point of interest is determined by

$$N = N_i \pm \frac{\rho}{180} \quad , \qquad \text{(H-1)}$$

where

N_i = fringe moved to produce extinction at the point of interest, and

ρ = analyzer rotation to produce extinction.

The plus sign is used in equation (H-1) if N_i is moved toward N_{i+1} during analyzer rotation. The negative sign is used if N_i is moved toward N_{i-1}. Analyzer rotation is best determined by averaging measurements of the leading and trailing edges of the fringe as it passes the point of interest.

Fractional order fringes were determined from Table H-1 for appropriate values of ρ.

Table H-1

Tardy Compensation Fraction Fringe Order Equivalents

ρ	ρ/180	ρ	ρ/180	ρ	ρ/180	ρ	ρ/180
1	.0056	51	.2833	101	.5611	151	.8389
2	.0111	52	.2889	102	.5667	152	.8444
3	.0167	53	.2944	103	.5722	153	.8500
4	.0222	54	.3000	104	.5778	154	.8556
5	.0278	55	.3056	105	.5833	155	.8611
6	.0333	56	.3111	106	.5889	156	.8667
7	.0389	57	.3167	107	.5944	157	.8722
8	.0444	58	.3222	108	.6000	158	.8778
9	.0500	59	.3278	109	.6056	159	.8833
10	.0556	60	.3333	110	.6111	160	.8889
11	.0611	61	.3389	111	.6167	161	.8944
12	.0667	62	.3444	112	.6222	162	.9000
13	.0722	63	.3500	113	.6278	163	.9056
14	.0778	64	.3556	114	.6333	164	.9111
15	.0833	65	.3611	115	.6389	165	.9167
16	.0889	66	.3667	116	.6444	166	.9222
17	.0944	67	.3722	117	.6500	167	.9278
18	.1000	68	.3778	118	.6556	168	.9333
19	.1056	69	.3833	119	.6611	169	.9389
20	.1111	70	.3889	120	.6667	170	.9444
21	.1167	71	.3944	121	.6722	171	.9500
22	.1222	72	.4000	122	.6778	172	.9556
23	.1278	73	.4056	123	.6833	173	.9611
24	.1333	74	.4111	124	.6889	174	.9667
25	.1389	75	.4167	125	.6944	175	.9722
26	.1444	76	.4222	126	.7000	176	.9778
27	.1500	77	.4278	127	.7056	177	.9833
28	.1556	78	.4333	128	.7111	178	.9889
29	.1611	79	.4389	129	.7167	179	.9944
30	.1667	80	.4444	130	.7222	180	1.0000
31	.1722	81	.4500	131	.7278		
32	.1778	82	.4556	132	.7333		
33	.1833	83	.4611	133	.7389		
34	.1889	84	.4667	134	.7444		
35	.1944	85	.4722	135	.7500		
36	.2000	86	.4778	136	.7556		
37	.2056	87	.4833	137	.7611		
38	.2111	88	.4889	138	.7667		
39	.2167	89	.4944	139	.7722		
40	.2222	90	.5000	140	.7778		
41	.2278	91	.5056	141	.7833		
42	.2333	92	.5111	142	.7889		
43	.2389	93	.5167	143	.7944		
44	.2444	94	.5222	144	.8000		
45	.2500	95	.5278	145	.8056		
46	.2556	96	.5333	146	.8111		
47	.2611	97	.5389	147	.8167		
48	.2667	98	.5444	148	.8222		
49	.2722	99	.5500	149	.8278		
50	.2778	100	.5556	150	.8333		

APPENDIX I

STRESS CONCENTRATION FACTORS

DETERMINED FROM PHOTOELASTIC T-CONNECTION MODELS

APPENDIX I

STRESS CONCENTRATION FACTORS DETERMINED FROM PHOTOELASTIC T-CONNECTION MODELS

Results of analysis of T-connection slices are portrayed graphically in Figures I-1 through I-15 as stress concentration factors, K_t and K_0.

$$K_t = \frac{\sigma_t}{\sigma_n}$$

and (I-1)

$$K_0 = \frac{\sigma_0}{\sigma_n}$$

where

σ_t = stress parallel to the longitudinal axis of slice, Figure 28,

σ_0 = stress orthogonal to σ_t and in the plane of the slice unloaded surface, Figure 28, and

$\sigma_n = \frac{P}{A}$, nominal brace stress, equation (6-5).

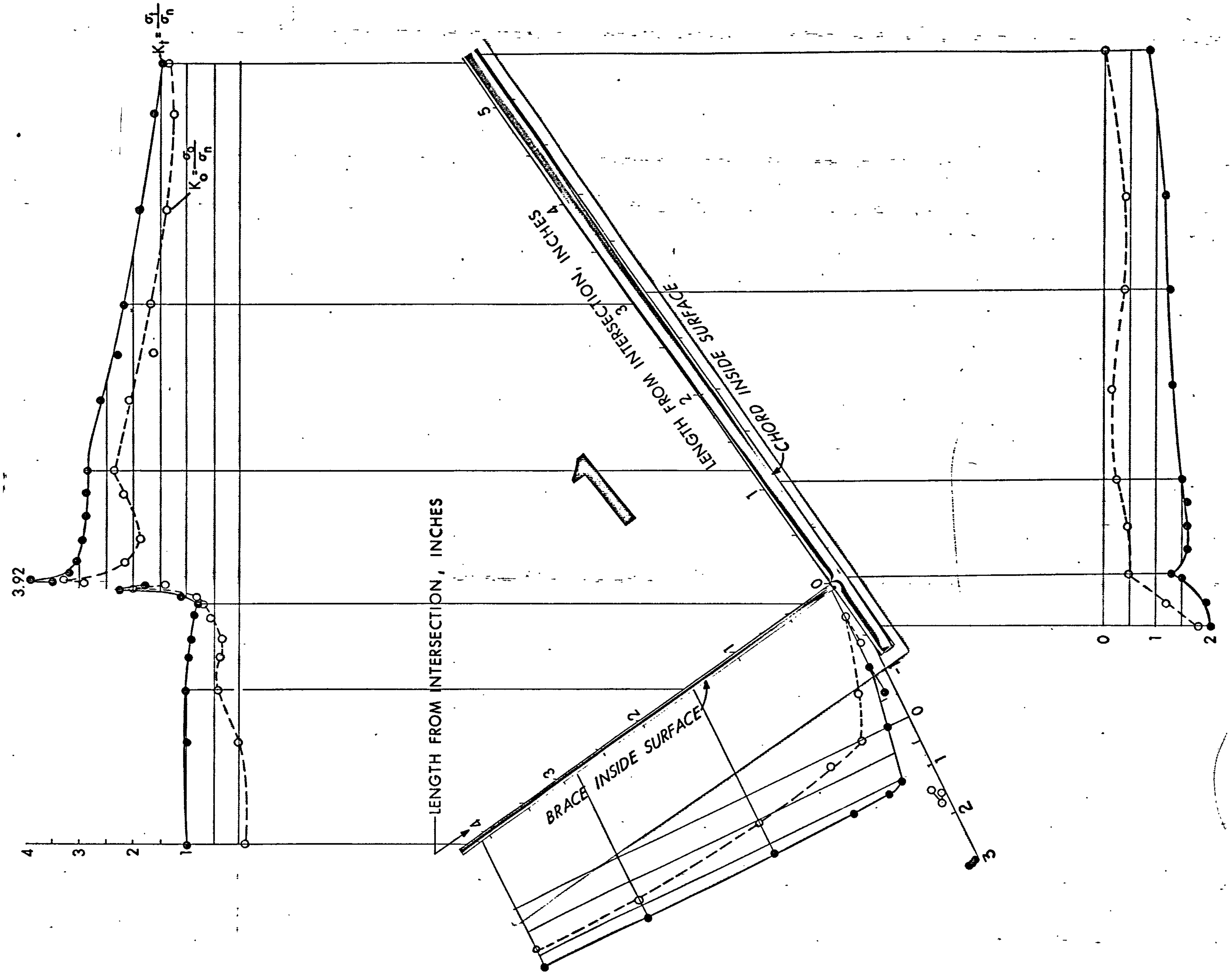

Fig. I-1 - Distribution of stress concentration factors on inner and outer surfaces of 0° and 180° slices (at $\varphi = 0°$) of T-connection Model 1, $\alpha = 4.91$, $\beta = 0.5$, $\gamma = 13.62$, $\tau = 0.354$, and slice thickness 0.224 inch

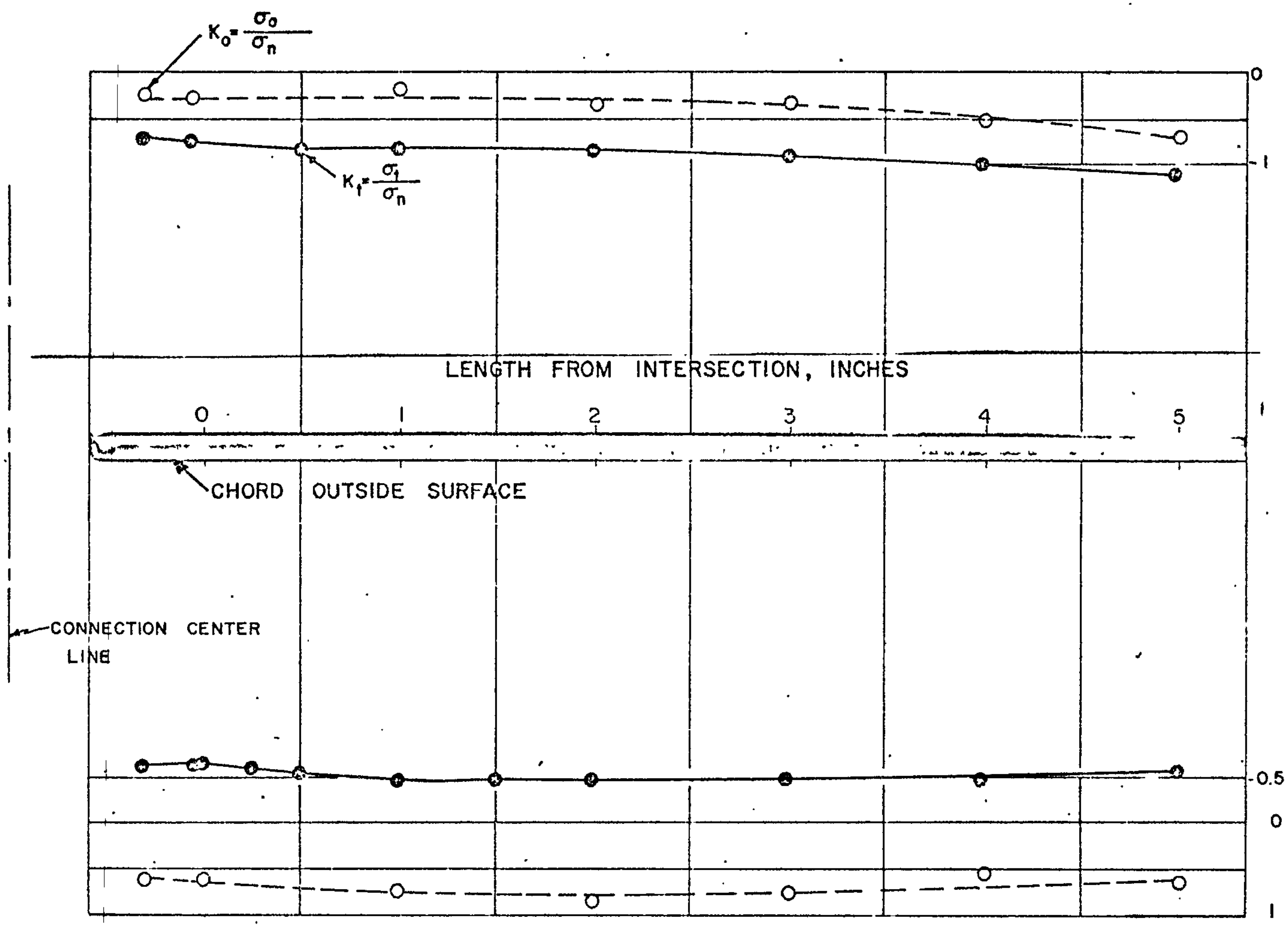

Fig. I-2 - Distribution of stress concentration factors on inner and outer surfaces of 0° and 180° slices (at φ = 180°) of T-connection Model 1, α = 4.91, β = 0.5, γ = 13.62, τ = 0.354, and slice thickness 0.226 inch

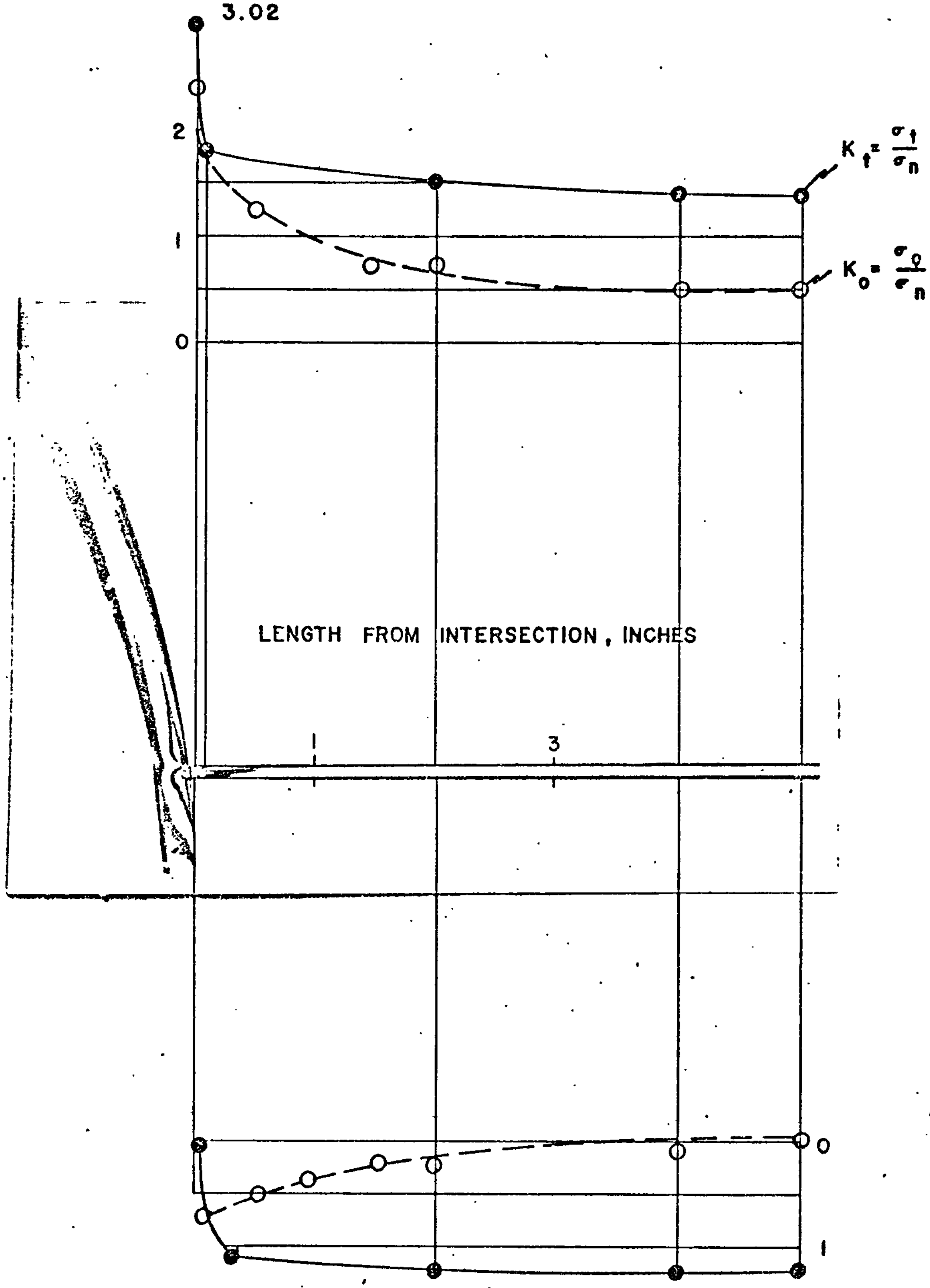

Fig. I-3 - Distribution of stress concentration factors on inner and outer brace surfaces of 30°, 150°, 210° and 330° slices of T-connection Model 1, α = 4.91, β = 0.5, γ = 13.62, τ = 0.354, and slice thickness 0.221 inch

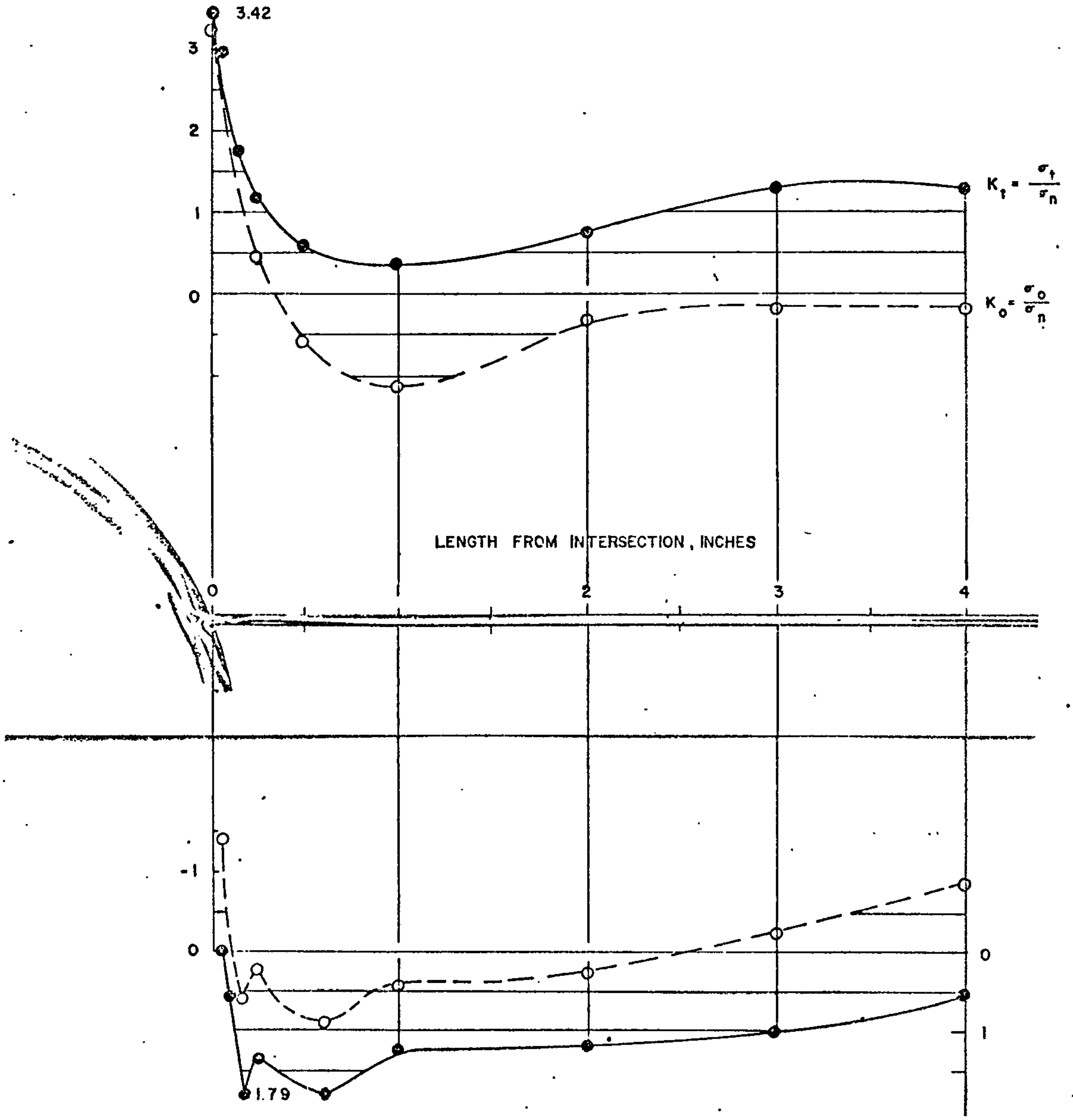

Fig. I-4 - Distribution of stress concentration factors on inner and outer brace surfaces of 60°, 120°, 240°, and 300° slices of T-connection Model 1, $\alpha = 4.91$, $\beta = 0.5$, $\gamma = 13.62$, $\tau = 0.354$, and slice thickness 0.224 inch

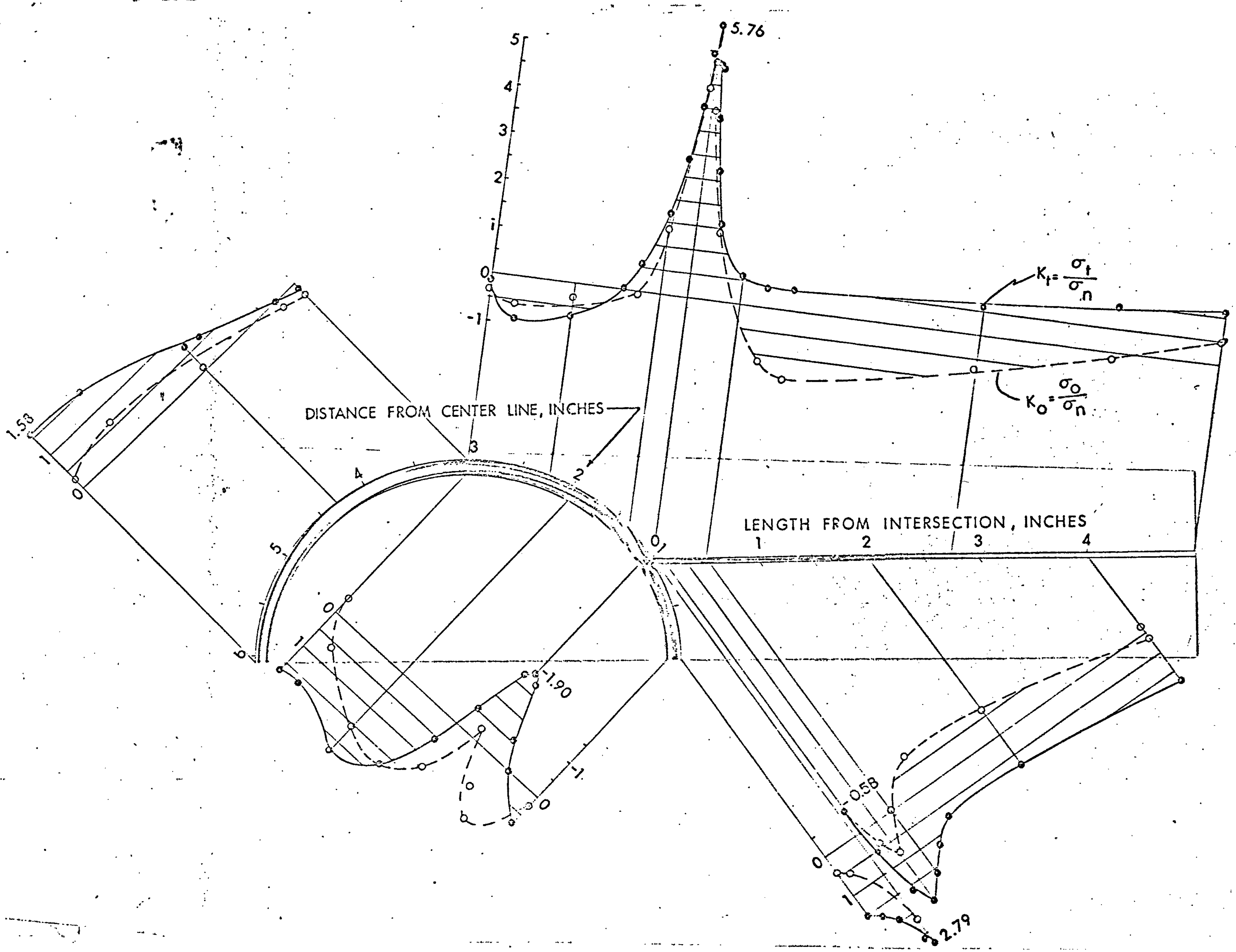

Fig. I-5 - Distribution of stress concentration factors on inner and outer surfaces of 90° and 270° slices of T-connection Model 1, $\alpha = 4.91$, $\beta = 0.5$, $\gamma = 13.62$, $\tau = 0.354$, and slice thickness 0.246 inch

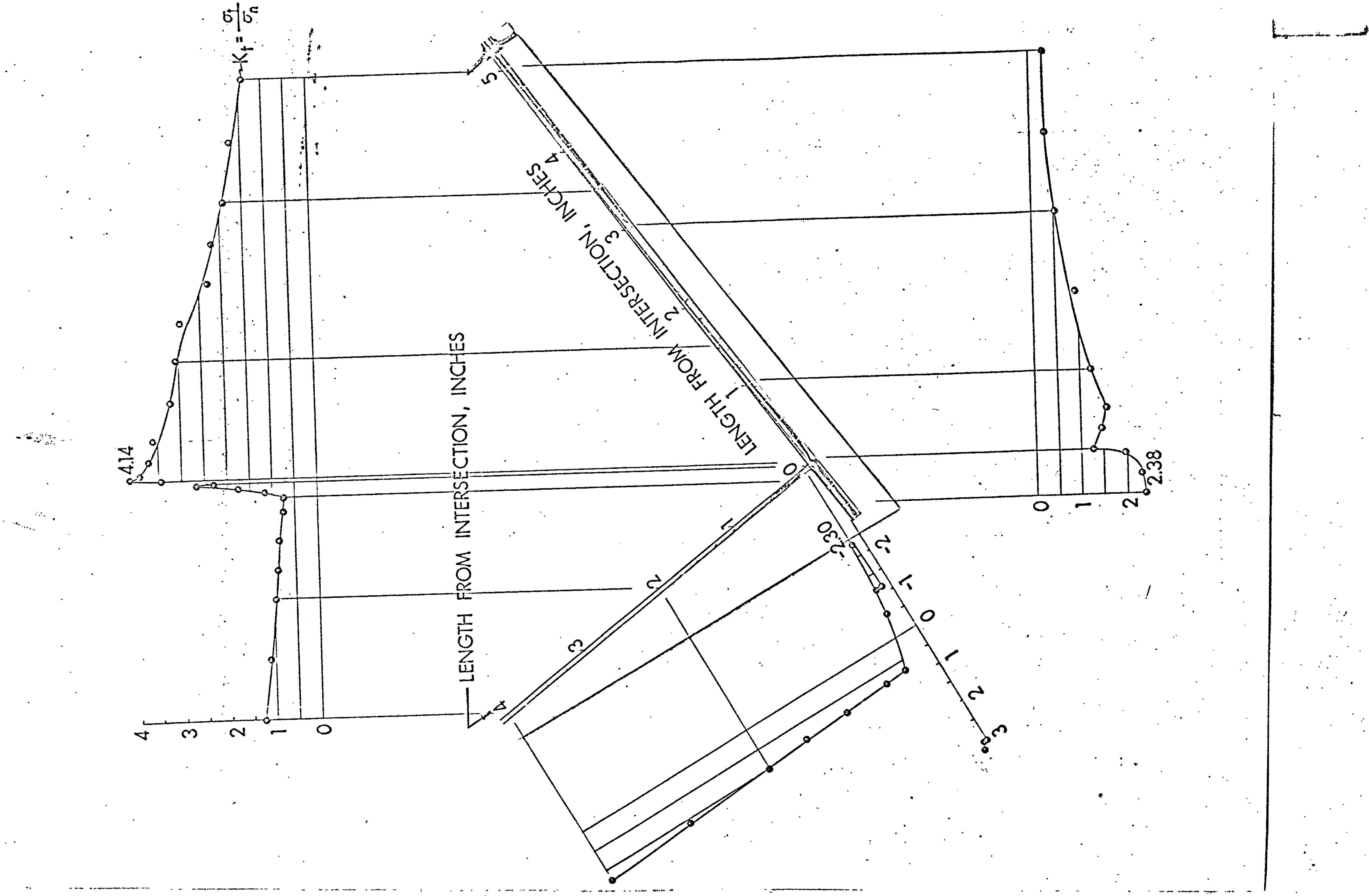

Fig. I-6 - Distribution of stress concentration factors on inner and outer surfaces of 0° and 180° slices (at $\varphi = 0°$) of T-connection Model 2, $\alpha = 4.91$, $\beta = 0.5$, $\gamma = 18.38$, $\tau = 0.486$ and slice thickness 0.234 inch

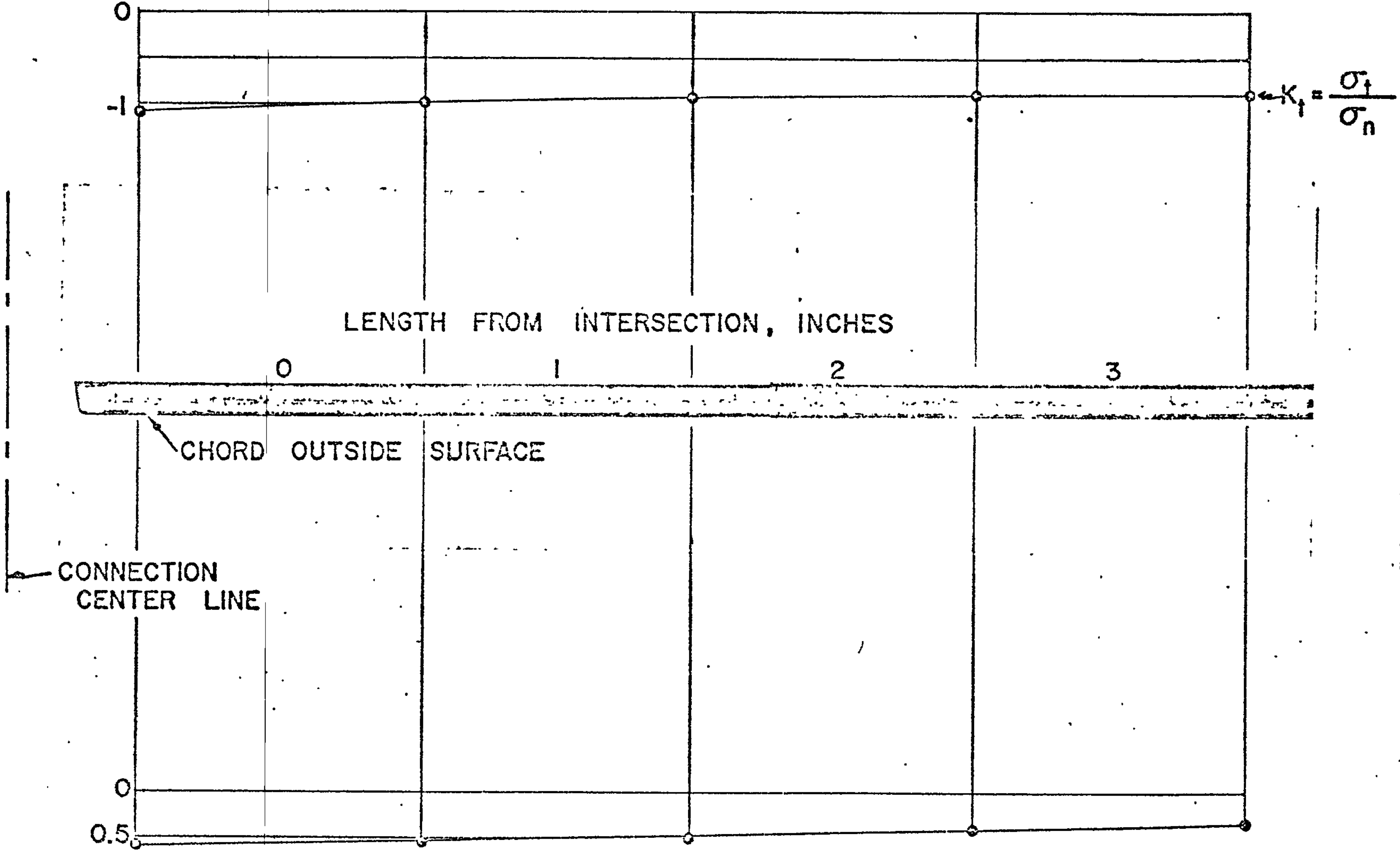

Fig. I-7 - Distribution of stress concentration factors on inner and outer surfaces of 0° and 180° slices (at φ = 180°) of T-connection Model 2, α = 4.91, β = 0.5, γ = 18.38, τ = 0.486, and slice thickness is 0.237 inch

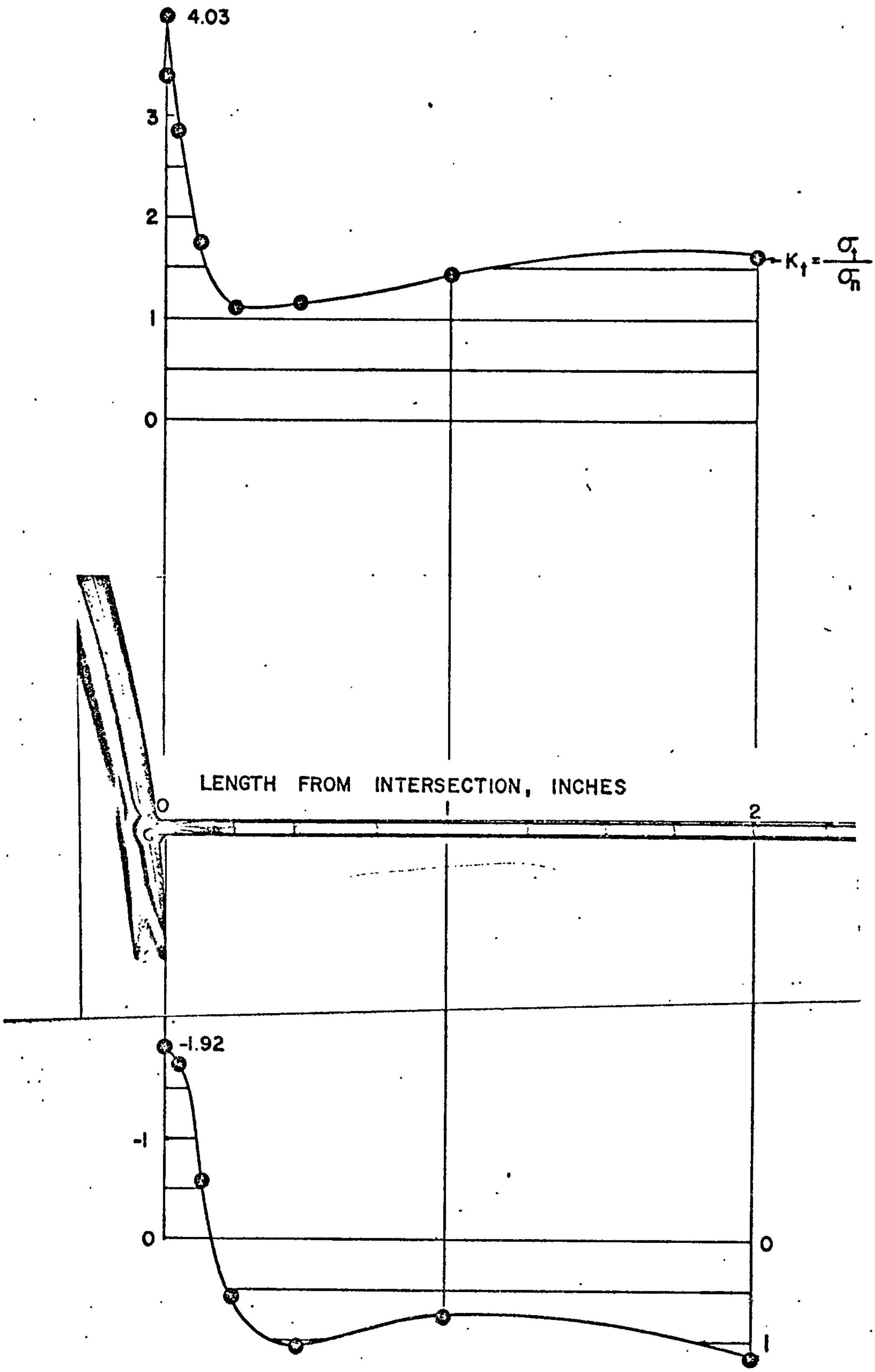

Fig. I-8 - Distribution of stress concentration factors on inner and outer surfaces of 30°, 150°, 210°, and 330° slices of T-connection Model 2, $\alpha = 4.91$, $\beta = 0.5$, $\gamma = 18.38$, $\tau = 0.486$ and slice thickness is 0.237 inch

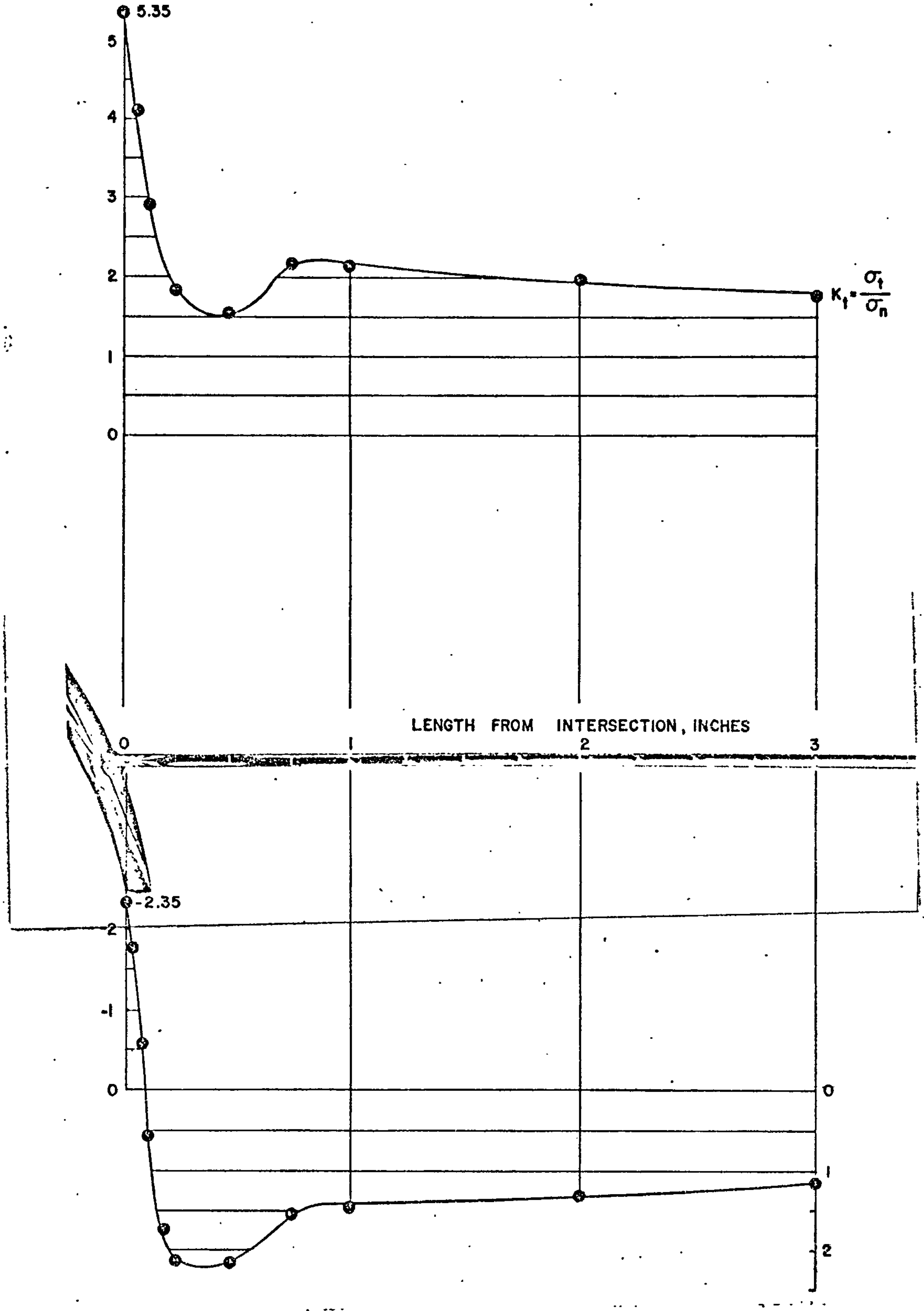

Fig. I-9 - Distribution of stress concentration factors on inner and outer surfaces of 60°, 120°, 240°, and 300° slices of T-connection Model 2, $\alpha = 4.91$, $\beta = 0.5$, $\gamma = 18.38$, $\tau = 0.486$, and slice thickness is 0.233 inch

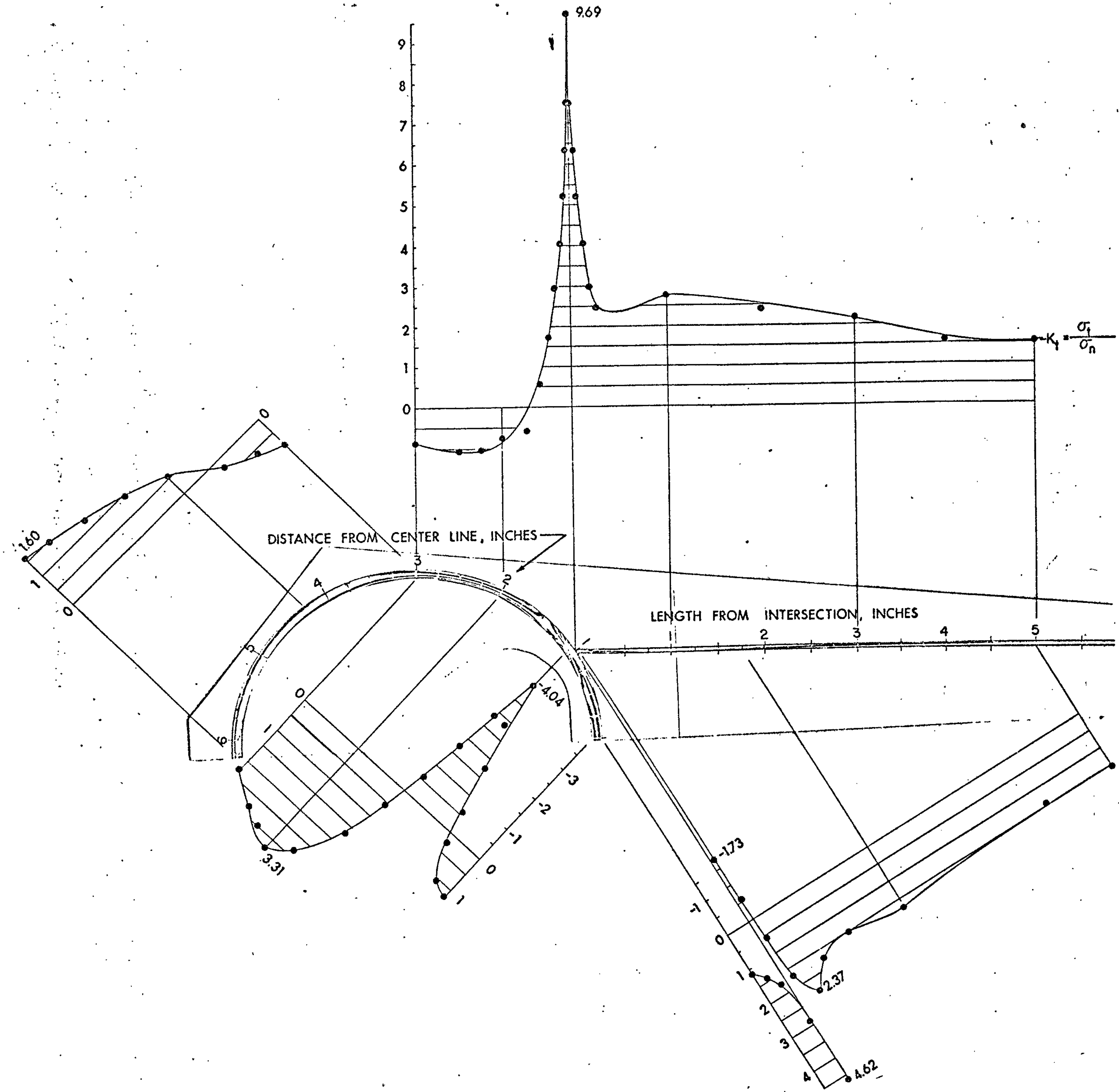

Fig. I-10 - Distribution of stress concentration factors on inner and outer surfaces of 90° and 270° slices of T-connection Model 2, α = 4.91, β = 0.5, γ = 18.38, τ = 0.486, and slice thickness is 0.233

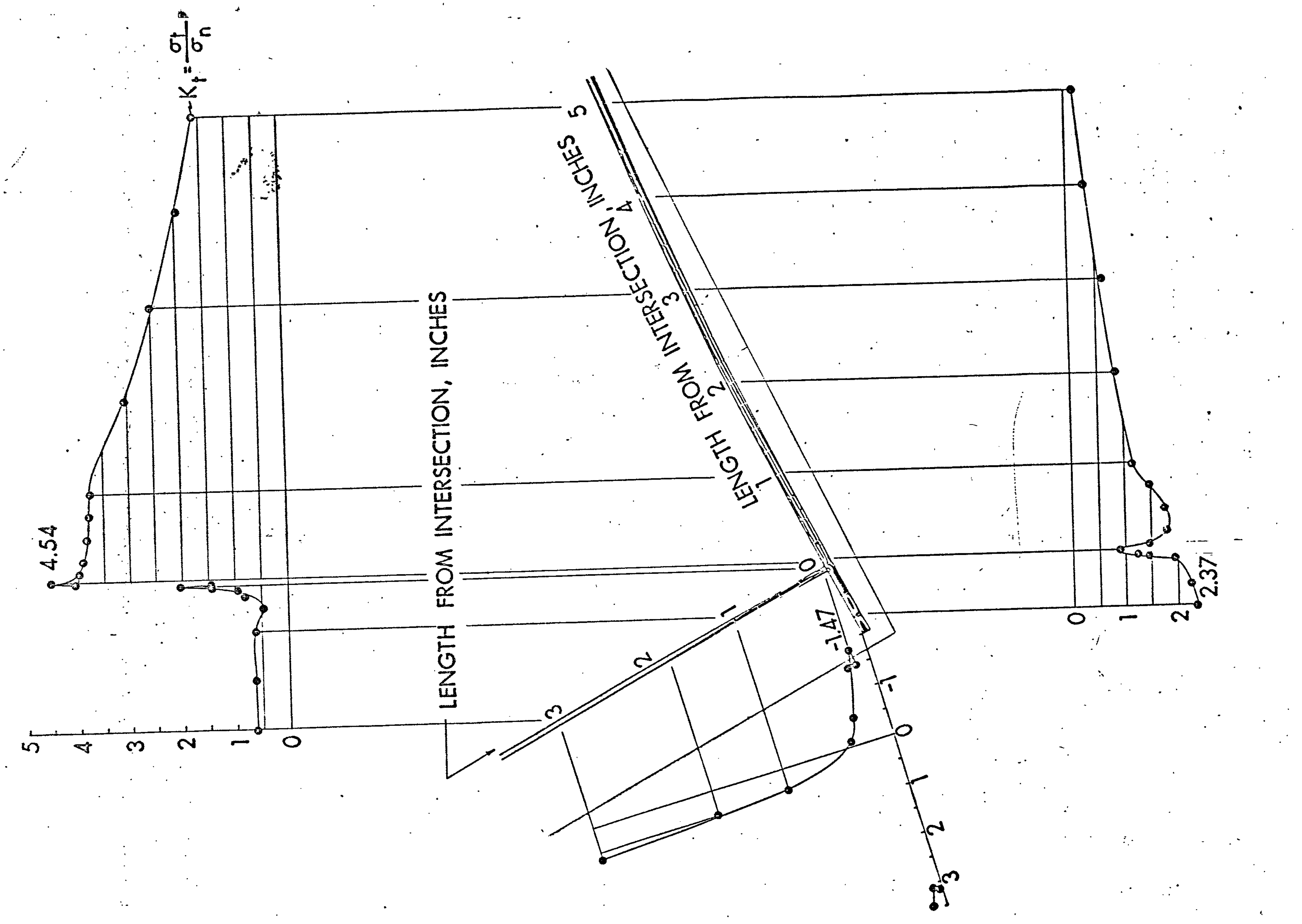

Fig. I-11 - Distribution of stress concentration factors on inner and outer surfaces of 0° and 180° slices (at $\varphi = 0°$) of T-connection Model 3, $\alpha = 4.91$, $\beta = 0.5$, $\gamma = 24.40$, $\tau = 0.610$ and slice thickness 0.256 inch

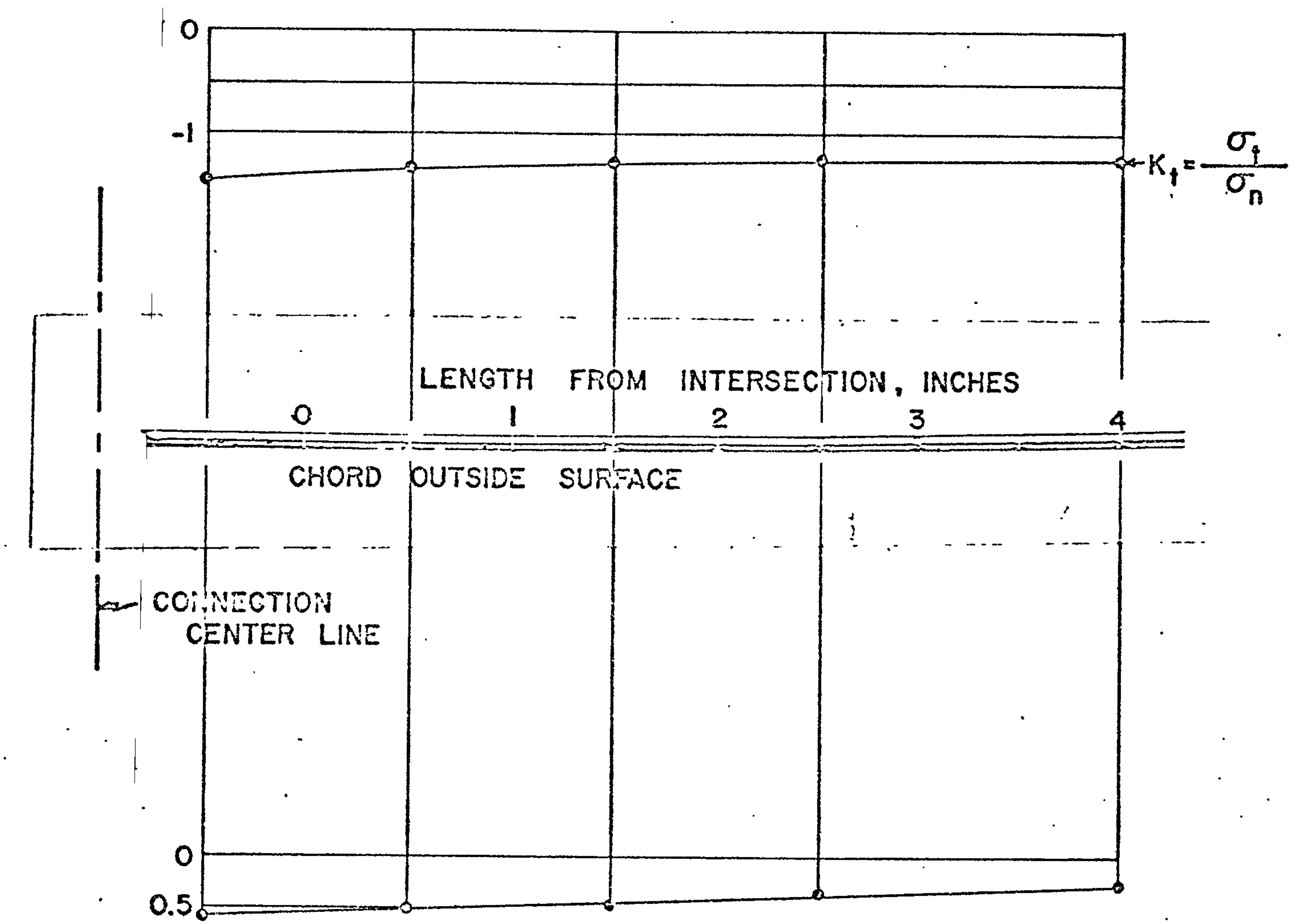

Fig. I-12 - Distribution of stress concentration factors on inner and outer surfaces of 0° and 180° slices (at $\varphi = 180°$) of T-connection Model 1, $\alpha = 4.91$, $\beta = 0.5$, $\gamma = 24.40$, $\tau = 0.610$, and slice thickness is 0.251 inch

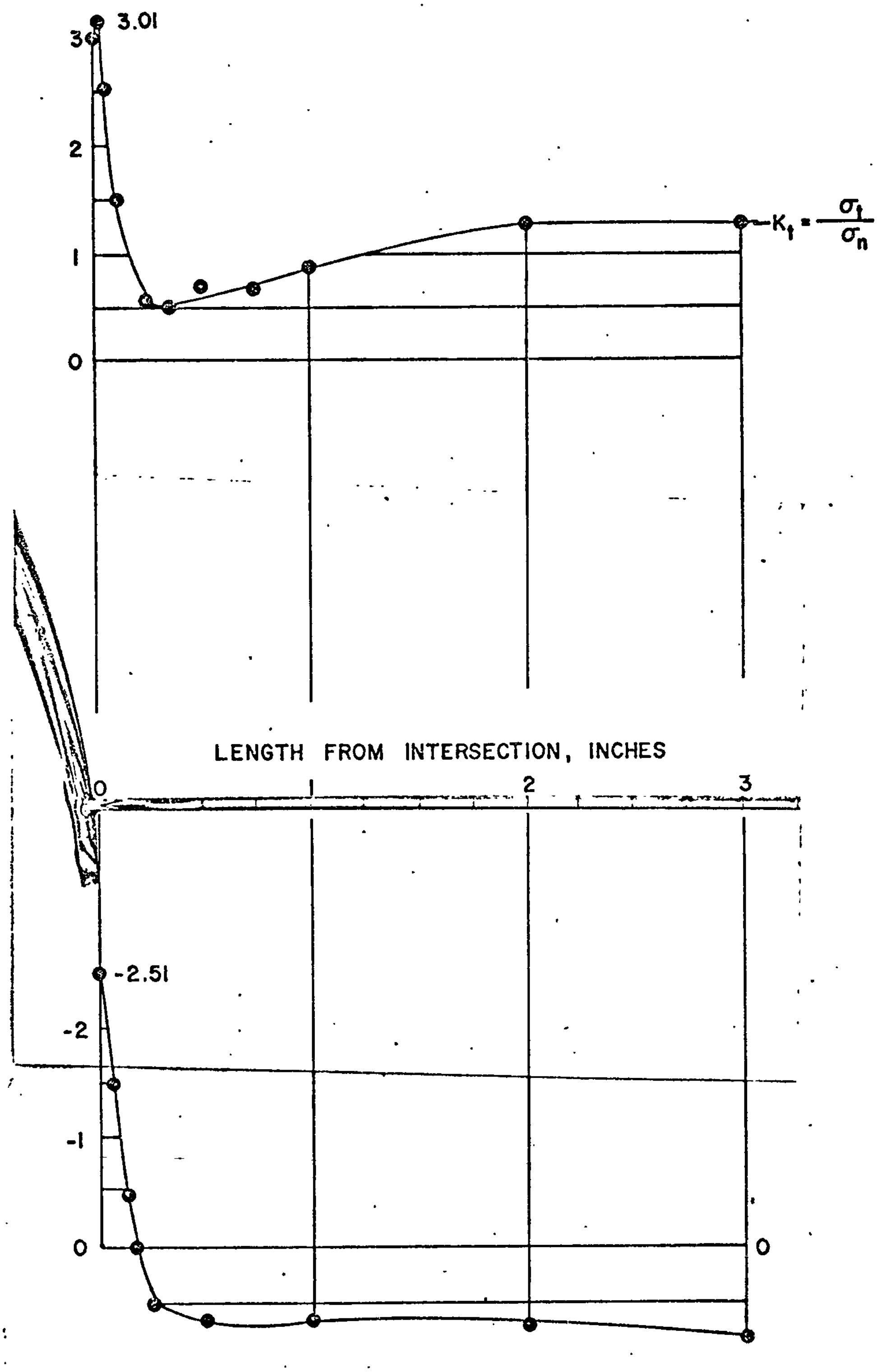

Fig. I-13 - Distribution of stress concentration factors on inner and outer brace surfaces of 30°, 150°, 210°, and 330° slices of T-connection Model 1, α = 4.91, β = 0.5, γ = 24.40, τ = 0.610 and slice thickness is 0.255 inch

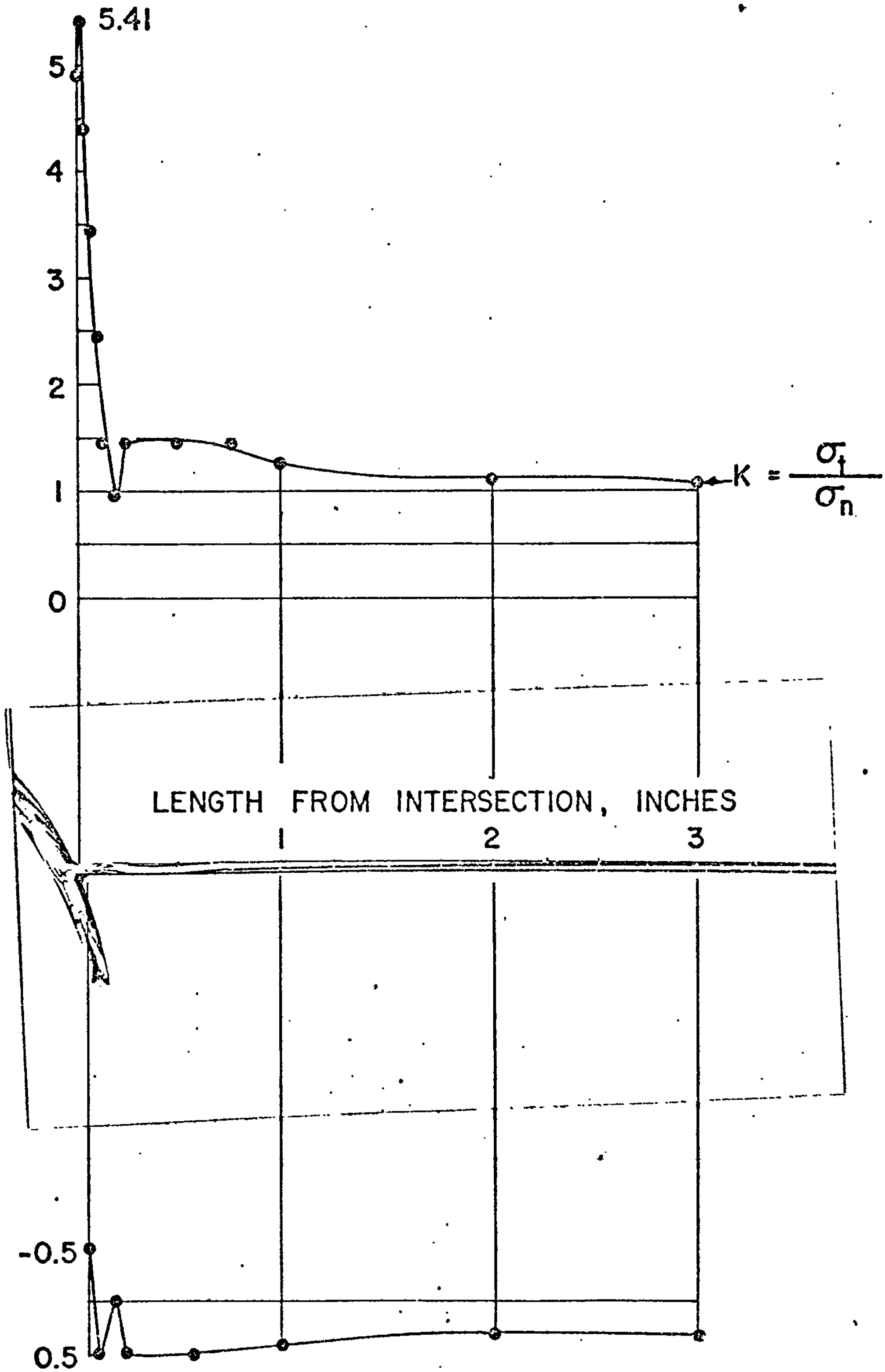

Fig. I-14 - Distribution of stress concentration factors on inner and outer brace surfaces of 60°, 120°, 240°, and 300° slices of T-connection Model 1, α = 4.91, β = 0.5, γ = 24.40, τ = 0.610, and slice thickness is 0.250 inch

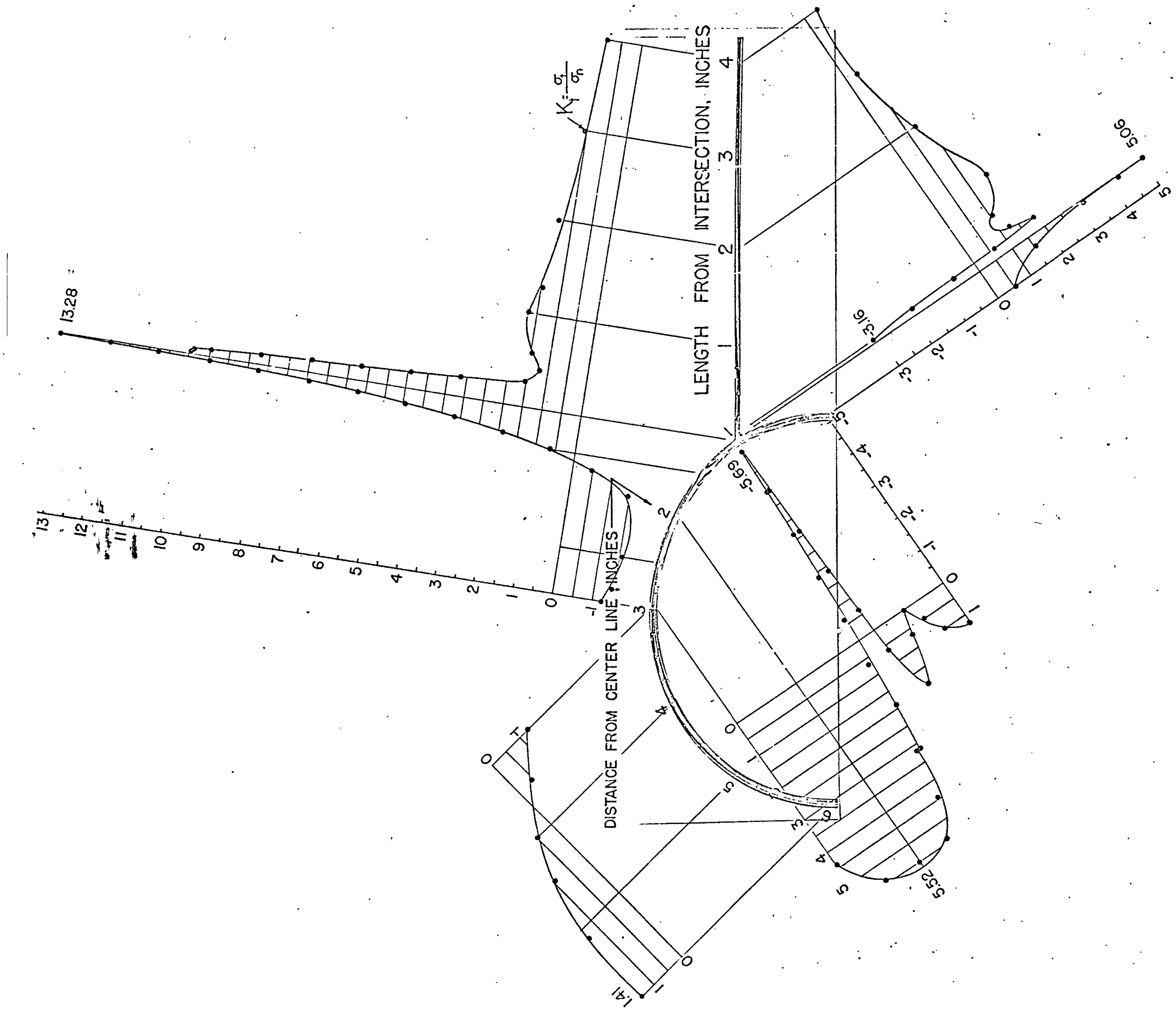

Fig. I-15 - Distribution of stress concentration factors on inner and outer surfaces of 90° and 270° slices of T-connection Model 1, α = 4.91, β = 0.5, γ = 24.40, τ = 0.610, and the slice thickness is 0.255 inch